Dissertation
submitted to the
Combined Faculties for the Natural Sciences and for Mathematics
of the Ruperto-Carola University of Heidelberg, Germany
for the degree of
Doctor of Natural Sciences

Put forward by
M.Sc. Elisabeth Brühl
born in Heidelberg

Oral examination: 25.07.2017

Systematic Study on Coherent Control of Electronic Population and Vibrational Coherence in the One-Photon Regime

Referees:

Prof. Dr. Marcus Motzkus
Prof. Dr. Wolfgang Petrich

Abstract: In the scope of this thesis, a systematic study about coherent control with shaped femtosecond pulses in the one-photon regime was performed. This regime is especially important in nature as photochemical and -physical reactions are driven by sun light, i.e. at very low intensities. Apart from the relevance of these conditions in nature, coherent control experiments at low intensity are well suited to gain understanding of the underlying processes as well as to control them by using shaped laser light fields. For the experimental shaping in the visible spectral range, a liquid-crystal spatial light modulator (LCM) was utilized. Here, it was shown for the first time that such an LCM introduces noise on the tailored spectral phase. The detailed characterization of the noise implied that molecular properties like the mobility of the liquid crystals cause the noise. Reliable pulse shapes on a pulse-to-pulse basis were achieved by externally cooling the LCM. Due to appropriate data averaging, coherent control experiments were successfully performed, where even small differences in the shaped pulses are important. These control experiments aimed at the enhancement of electronic population and vibrational coherence in the ground and excited state in dependence on the temporal shape of the excitation pulses for various excitation spectra. The temporal shape of the excitation pulse was tailored to linearly chirp pulses, multipulses, whose interpulse distance matches the period of the dominant molecular mode, and the sum of both as chirped multipulses. While the ideal choice to enhance the population and the vibrational coherence in the ground state is a resonant negatively chirped multipulse, the excited state is enhanced best with a blue-detuned positively chirped multipulse. These transient absorption experiments were performed on a prototype chromophore. However, the results should be applicable to other systems.

These kinds of control experiments should be transferred to DNA bases and prototype molecules, which can be easily addressed theoretically. As many organic molecules absorb light in the ultraviolet wavelength regime, an experimental setup for the shaping of femtosecond pulses in the spectral range between 250 nm and 350 nm was developed and characterized in detail. This setup provides the basis for future experiments with organic samples.

Zusammenfassung: Im Rahmen dieser Arbeit wurde eine systematische Studie auf dem Gebiet der kohärenten Kontrolle mit modulierten Femtosekundenimpulsen im Ein-Photonen-Regime durchgeführt. Dieses Regime ist besonders in der Natur von Bedeutung, da photochemische und -physikalische Reaktionen durch Sonnenlicht getrieben werden und damit bei sehr geringen Intensitäten stattfinden. Neben der Relevanz dieser Prozesse in der Natur sind kohärenter Kontrollexperimente bei geringen Intensitäten gut geeignet, um ein Verständnis für die zugrundeliegenden Prozesse zu erhalten und sie mittels modulierter Laserlichtfelder zu kontrollieren. Für die experimentelle Modulation im sichtbaren Spektralbereich wurde eine Flüssigkristallmaske verwendet. Zum ersten Mal wurde hier gezeigt, dass eine solche Maske Rauschen auf die modulierte spektrale Phase aufprägt. Die detaillierte Charakterisierung dieses Rauschens deutete an, dass molekulare Eigenschaften wie die Mobilität der Flüssigkristalle das Rauschen verursacht. Zuverlässige Impulsmodulationen auf einer Puls-zu-Puls-Basis wurden durch eine externe Kühlung der Maske erreicht. Mithilfe einer geeigneten Datenmittelung wurden erfolgreich Experimente zur kohärenten Kontrolle durchgeführt, bei denen bereits kleine Unterschiede in der Impulsmodulation wichtig sind. Ziel dieser Kontrollexperimente war die Verstärkung der elektronischen Population und Schwingungskohärenz im Grundzustand und im angeregten Zustand in Abhängigkeit von der zeitlichen Modulation des Anregungsimpulses für verschiedene Anregungsspektren. Die zeitliche Impulsform des Anregungspulses wurde mit linearem Chirp, Multipulsen, deren Subpulsabstand der Periode einer dominanten molekularen Schwingung entsprach, und der Summe aus beiden als gechirpte Multipulse moduliert. Die ideale Wahl um die Population und Schwingungskohärenz im Grundzustand zu verstärken ist ein resonanter negativ gechirpter Multipuls. Der angeregte Zustand wird mit einem blauverschobenen positiv gechirptem Multipuls am besten verstärkt. Diese transienten Absorptionsexperimente wurden an einem Prototyp-Chromophor durchgeführt, aber die Ergebnisse sollten auf andere Systeme übertragbar sein. Diese Art der Kontrollexperimente soll auf DNA-Basen und Prototypmoleküle übertragen werden, welche theoretisch gut beschrieben werden können. Da viele organische Moleküle Licht im ultravioletten Wellenlängenbereich absorbieren, wurde ein experimenteller Aufbau zur Modulatoren von Femtosekundenimpulsen im Spektralbereich von 250 nm bis 350 nm entwickelt und im Detail charakterisiert. Dieser Aufbau kann als Ausgangspunkt für zukünftige Experimente mit organischen Proben genutzt werden.

Contents

1 Introduction

In traditional chemistry, synthesis is controlled by utilizing macroscopic quantities such as temperature, pressure and concentration of components. An alternative, physical approach to control chemical reactions is based on light-matter interactions. Nowadays laser sources are available for this purpose, which provide laser pulses with durations on the order of nuclear processes within molecules, i.e. in the order of tens to hundreds of femtoseconds. In Figure 1.1, the idea of coherent control is depicted in a simplified schematic drawing. A triatomic molecule is irradiated by a femtosecond pulse to break one of the chemical bonds. To be able to select a specific bond to break, while the other one is unaffected, the temporal and spectral shapes of this excitation pulse are modulated. The constructive and destructive interferences between various quantum pathways to the final state are controlled by the light field. Already small variation of the pulse shape can determine which final molecular state is predominantly reached.

Over the last decades, a number of successful control experiments were demonstrated [1–4]. Beside the fragmentation of molecules [5], also energy transfer between intra- and intermolecular channels [6, 7] and photoisomerization processes [8] were controlled. The control in the low-intensity regime is of special interest as many natural photophysical and photochemical processes are initiated by low light intensity. Prominent examples are the light-driven reactions in photosynthetic units and light receptors. The question arises if biological functions can be improved by coherent light. Early theories on coherent control claimed that photochemical reactions cannot be controlled in the low-intensity regime [9]. However, this theory was disproved by successful experiments on the

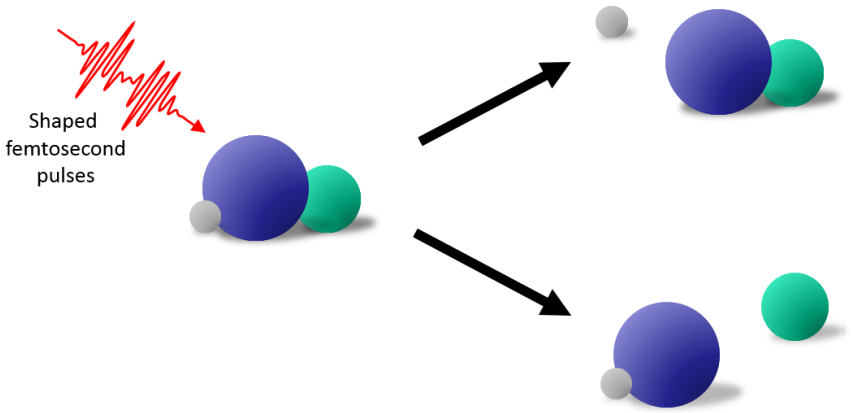

Figure 1.1: Schematic picture of coherent control. The final state of a chemical reaction, here bond breaking, depends on the shape of a femtosecond pulse.

weak-field control of the retinal isomerization efficiency in bacteriorhodopsin, which is responsible for vision in higher organisms [8, 10, 11]. As these examples show, first control experiments aimed an successful control. However, the search for the underlying light-matter interaction got more and more into the focus. Nowadays, an additional goal is to find the crucial parameters for successful coherent control and to develop rules of thumb, which can be applied for various molecular systems [1].
At low intensity, mainly the ground state and first excited state are involved. Subsequently, most higher lying states can be neglected and the complexity of the molecular system is crucially reduced. For example, one focuses on the control of the population and vibrational coherence of the ground state and first excited state. Typical examples of control parameters, which influence population and vibrational coherence, are linear chirp and multipulse excitation (depicted schematically in Figure 1.2(a,b)) as well as the spectral overlap between excitation and absorption spectra [12–14].

Following and combining these various avenues, a systematic study is performed in the scope of the present work to investigate the interplay between the spectral overlap as well as the temporal shape of the excitation pulse. For the first time, the effect of linear chirp and multipulse is directly compared and

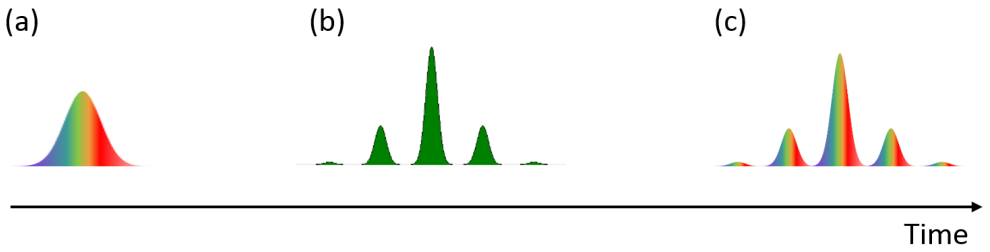

Figure 1.2: Temporal distriubtion of a linear chirped pulse (a), a multipulse (b) and the combination of these two to a chirped multipulse (c).

both phase modulations are combined to a chirped multipulse to analyze their interplay (see Figure 1.2(c)). The goal of this study is to provide a guideline for parameter sets in future control experiments. Furthermore, this study can be used to analyze the failure of many attempts to control molecular processes in the past (e.g. [15]) and can help to find better parameter sets.
For these kinds of experiments, where only small differences in the shaped pulses are important, reliable pulse shaping methods are required. For this purpose, over the last decades a number of different shaping devices have been developed [16–20]. One of the most widely used devices is the so-called liquid-crystal spatial light modulator (LCM) [21]. It shows an efficient and accurate shaping performance [22], which allows shaping of high precision [23]. However, as shown in the present work, it is still challenging to shape sub-15 fs pulses with LCMs reliably on a shot-to-shot basis. For various experimental conditions, phase instabilities were observed and characterized. Nevertheless, the shaping performance is successfully optimized, which makes it possible to perform the systematic study of coherent control described previously.

Over the last decades, mainly large molecules have been investigated in such control experiments as the molecular absorption spectra in the visible are overlapping with the spectra of most common laser sources. However, the investigation of small molecular systems, that can be described theoretically, is more promising to gain knowledge about the most basic control mechanisms. As such molecules predominantly absorb in the ultraviolet (UV) regime, the generation and especially the shaping of femtosecond pulses in the UV are required, which is much more demanding than in the visible. Nevertheless, there is intensive research

going on to overcome these challenges for the generation [24–26] as well as for the shaping of femtosecond pulses in the UV using various techniques [27–30]. In the scope of this thesis, a shaping set-up, based on an acousto-optic modulator (AOM), for the UV is developed, which allows expanding the spectral regime for control experiments to the UV.

Structure of the Thesis

The thesis is structured as follows. In **Chapter 2**, the study on the phase artifacts of the LCM in presented. It includes an experimental part and to reproduce these observations a simulation. After the introduction, the background provides an overview of the shaping of femtosecond pulses and the working principle of the LCM. Furthermore, details about the experiment and simulation are given. Next, the results from experiment and simulation are presented and discussed. Finally, a summary is given. **Chapter 3** starts with a motivation for the systematic study on coherent control with tailored pulses. In the next sections, the experimental method for this part, which is transient absorption spectroscopy, the data acquisition and the data analysis are introduced. After the description of the experimental details, the results are presented. It includes general results from the transient absorption data, various effects on the vibrational coherence as well as the enhancement due to tailored excitation pulses. These results are discussed and finally a conclusion is drawn. In **Chapter 4**, the third project within this thesis, the development of an AOM-based shaping system in the UV, is reported. First, the need for shaped pulses in the UV is motivated. Second, a brief overview of currently available UV shaping systems is given and the choice of the AOM is explained. Next, the working principle of the latter is described. The implementation of the AOM comprises the optical and electronical configuration as well as its spectral calibration. In the section about the characterization of the AOM, its shaping performance is presented, which allows for a comparison of the newly developed system and the systems stated in the literature. At the end of this chapter, it is summarized and an outlook for UV shaping is given. The thesis ends with a summary and an outlook for coherent control in **Chapter 5**.

Characterization and Minimization of Phase Noise in LCMs

2

For control experiments with shaped pulses, small modulations in the pulse shape can have a significant impact. Therefore, it is crucial to realize reliable pulse shaping. In this chapter[1], a study is presented on spectral phase noise, which is introduced by a liquid crystal modulator (LCM) and which directly influences the shaping performance. The shot-to-shot second-order intensity autocorrelation trace (AC) and the second harmonic (SH) signal are utilized to characterize the phase noise of unshaped and shaped pulses. Furthermore, the second-order intensity auto-correlation is numerically simulated to get a deeper insight into the temperature dependent phase instability on the pulse output. The simulation includes pulses with second-order Taylor and sinusoidal phase parameterizations to demonstrate the action of phase noise on typical shaped pulses in coherent control experiments. In the discussion, ideal experimental parameters are presented and possible reasons for the phase noise and especially the fact that it is now reported for the first time are pointed out.

[1]Parts of this chapter contribute to a paper, which is currently in preparation: E. Brühl, T. Buckup, and M. Motzkus. "Minimization of $1/f^n$ Phase Noise in Liquid Crystal Masks for Reliable Femtosecond Pulse Shaping". In preparation, 2017.

2.1 Introduction

LCMs are often used to tailor properties of femtosecond laser pulses. In spite of its extensive use, the performance of the LCM is not always satisfying. One limiting factor is the speed of how fast the tailoring of the laser electric field can be varied, i.e. the update rate of the modulation applied to the LCM, can be a challenge for the experimental application of LCMs based on nematic liquid crystals (LCs). In particular, applications like holographic tweezers or real-time control of photochemical reactions require response times, which are much faster than the one of commercial LCMs. Typically, commercial LCMs have modulation response times in the region of several tens of milliseconds [21] to hundreds of milliseconds, when a large voltage gradient is applied. This time scale is mainly determined by the nematic molecular re-orientational movement. For applying optimized voltages (e.g. overdrive switching), LCMs have been sped up to 1 ms in the lab though [31]. Higher update rates using usual nematic LCs molecules are constrained to time scale of the molecular orientational dynamics, which precludes its use in real-time control or spectroscopy with higher repetition lasers ($>1\,\mathrm{kHz}$).
Another challenge in the use of LCM is related to the orientation fluctuations of its LC molecules and the effect on the modulation stability in control experiments, which until now has been remained undiscussed. In spite of an applied control voltage (c.f. Section 2.2.2), the orientation of LCs is not fixed in space but is only constrained in a libration-like movement. As a consequence, a hindered orientational movement takes place in each pixel of an LCM and therefore, it can lead to noticeable phase instabilities on the output laser pulse. In the scope of the present work, the phase noise is characterized by shot-to-shot AC traces and the SH signals to analyze the impact of tailored bandwidth, acquisition time, operating temperature of the LCM and the average scheme.

2.2 Background

In the scope of this thesis, femtosecond pulses were shaped to various temporal pulse shapes and with several shaping devices. In the following, the basic idea of pulse shaping and the most prominent types of pulse shapes are introduced. In addition, the working principle of an LCM is explained. Further shaping devices are presented in Chapter 4.

2.2.1 Shaping of Femtosecond Pulses

Heisenberg's uncertainty principle dictates that temporally short pulses require a broad spectrum. For example, to generate a 10-fs pulse, a Gaussian spectrum with a spectral width of more than 10 % of the central wavelength is needed. It is not possible to modulate the temporal shape of femtosecond pulses in the time domain due to the temporal limitations of electronic devices. To circumvent this problem, shaping can be used to manipulate the spectral components of a temporarily dispersed light field. The light pulse in the time domain is linked via the Fourier transform to its correspondence in the spectral domain. In general, an electric field $E(\omega)$ can be described in the spectral domain by the amplitude, $E_0(\omega)$, and the phase, $\phi(\omega)$, which yields

$$E(\omega) = E_0(\omega) \exp[i\phi(\omega)]. \tag{2.1}$$

The modulation of $E_0(\omega)$ and $\phi(\omega)$ can result in a pulse, which is shaped in the temporal domain.

Phase Modulation

One possibiltiy to realize the temporal shaping of femtosecond pulses is to introduce relative phase shifts across the spectrum of the pulse. This phase modulation represents a deviation from the transform-limited pulse, where the

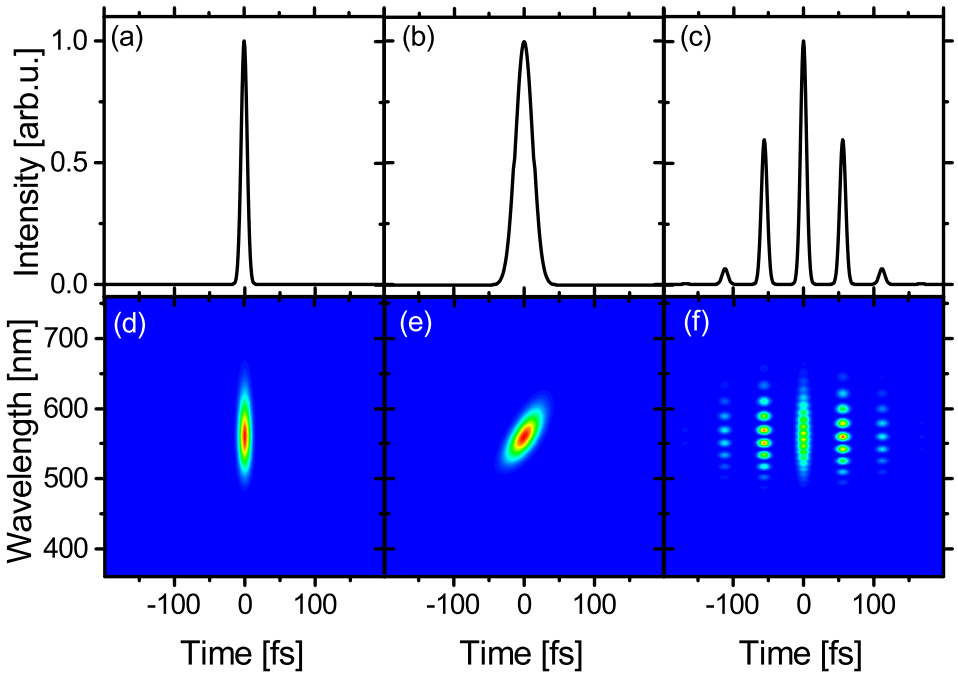

Figure 2.1: Simulated temporal distributions and 2D representations (wavelength versus time) for a transform-limited pulse (a, d), linearly chirped pulse with $\phi'' = 100\text{fs}^2$ (b e), multipulse with the parameters $a = 1.23$, $b = 56\,\text{fs}$, $c = 0$ (c, f).

phase is constant, i.e. $\phi(\omega) = 0$, across the whole spectrum. The most prominent types of phase modulation are chirp and multipulse. Temporal distributions and 2D representations (wavelength versus time) of transform-limited, linearly chirped and multipulses are shown in Figure 2.1.

Chirped Pulses The phase of the electric field can be expanded into a Taylor series around the center frequency ω_{cen}:

$$\begin{aligned}\phi(\omega) &= \sum_{n=0}^{N} \frac{1}{n!} \frac{d^n \phi(\omega)}{d\omega^n}\bigg|_{\omega=\omega_{cen}} \\ &= \sum_{n=0}^{N} \frac{b_n}{n!} (\omega - \omega_{cen})^n,\end{aligned} \tag{2.2}$$

where b_n is the expansion coefficient of the n-th order. In the case of a transform-limited pulse with a temporal duration (FWHM) of τ_{TL}, all prefactors b_n are zero for $n > 0$. For $b_1 \neq 0$, the whole pulse is shifted in time by b_1. The factor b_2 is responsible for temporal broadening. Positive values of b_2 cause a positively linear chirp, i.e. the low frequency components are ahead in time of the high frequencies. The reverse is true for negative values of b_2. As can be seen from Eqn. (2.2), b_2 represents the second derivative of ϕ at $\omega = \omega_{cen}$. Therefore, b_2 is abbreviated as ϕ'' in the following. The temporal duration (FWHM) of a chirped pulse, $\tau_{\phi''}$, can be estimated by:

$$\tau_{\phi''} = \sqrt{\tau_{TL}^2 + \ln(16)^2 \left(\frac{\phi''}{\tau_{TL}}\right)^2} \tag{2.3}$$

[32]. For $b_3 \neq 0$, temporal prepulses (for $b_3 < 0$) or postpulses (for $b_3 > 0$) are introduced. While their height with respect to the main peak is controlled by the magnitude of b_3, the spacing between the subpulses and their intensity cannot be varied independently. Higher order chirps are normally not considered.

Multipulses With a spectral phase of the form

$$\phi(\omega) = a \sin(b(\omega - \omega_{cen}) + c) \tag{2.4}$$

a so-called pulse train or multipulse (MP) is realized. The parameter b determines the spacing between the subpulses and the parameter c sets their relative phase. The amplitude a defines the relative height of the subpulse and it is given by Bessel functions of the first kind, J_n, [34] according to

$$a_n = J_n(a), \tag{2.5}$$

where n is the index of the subpulses. Additionally, when using the Jacobi-Anger identity [35][2],

$$\exp(ia\sin(x)) = \sum_{n=-\infty}^{\infty} J_n(a)\exp(inx), \tag{2.7}$$

an analytic expression for the multipulse in time domain can be written as:

$$E(t) = \exp(i\omega_{cen}t)\sum_{n=-\infty}^{\infty} J_n(a)E_{in}(t+nb)\exp(inc). \tag{2.8}$$

The relative phase $\Delta\phi = \phi_n + \phi_{n-1}$ between adjacent pulses is $\Delta\phi = c$ for prepulses, i.e. $n > 0$. In contrast it is $\Delta\phi = \pi - c$ for postpulses ($n < 0$) as the sign of the Bessel functions alternates according to

$$J_{-n}(x) = (-1)^n J_n(x). \tag{2.9}$$

In the scope of this thesis, c is set to 0. However, its influence on molecular systems, which are addressed with multipulses, is discussed in Ref. [33].

Temporal Characterization of Femtosecond Pulses

Beside the shaping of laser pulses, the direct, temporal measurement of pulsed laser is limited to picoseconds due to the intrinsic response time of electronic devices. To characterize shorter optical pulses, techniques based on optical correlation are required. One classic example is the autocorrelation, where the correlation between two replicas of the pulse itself is determined. An alternative is cross-correlation with another pulse, whose duration is similar or shorter and which has been characterized before. These correlation techniques provide the temporal profile of the pulse while the relative phase information is lost. However, this is sufficient to adjust the laser output, used in the experiments as well

[2] In Ref. [35] the Jacobi-Anger expansion has the form

$$\exp(ia\cos(x)) = \sum_{n=-\infty}^{\infty} i^n J_n(a)\exp(inx), \tag{2.6}$$

which can be rewritten as Eqn. (2.7) for real values of a.

as to verify the multipulse character and the chirp using Eqn. (2.3) of the shaped pulses. Its implementation is comparably easy and it provides direct information about the pulse, which are clear experimental advantages. The second-harmonic autocorrelator used to characterize the pulses in the visible used in this and the following chapter is described in Ref. [36].

For completeness, further techniques, described in the literature, will be briefly mentioned. More advanced methods suitable for temporal characterization are FROG (Frequency-Resolved Optical Gating) and the even more sophisticated SPIDER (Spectral Phase Interferometry for Direct Electric Field Reconstruction) systems [37, 38]. Spectral amplitude and phase of the pulse are reconstructed from the measured 2D trace in the time-frequency domain. However, these techniques require additional effort for implementation and procedure of the retrieval. A further drawback is the limited feedback rate.
Having a shaping device available opens up further possibilities for pulse characterization. A promising technique including a shaping device, which is already commercially available, is MIIPS (Multiphoton Intrapulse Interference, [39]). Furthermore, a method based on d-scan has been developed more recently [40]. In the two latter techniques, the femtosecond pulses are modified by additional spectral phases and the corresponding second-harmonic generation spectra as well as the fundamental spectrum are measured to fully characterize the pulse by reconstruction of the spectrum and phase.

In Chapter 4 femtosecond pulses in the ultraviolet (UV) will be shaped and characterized. For UV pulses no nonlinear crystals with phase matching and optical transmittance are readily available [41]. Therefore, the method of phase-matched, second-harmonic autocorrelation cannot be transferred to the UV. Besides cross correlation of different frequency mixing schemes [42], two-photon absorption offers a potentially easier alternative. Nonlinear crystals as well as a complimentary detector are replaced by a photon multiplier tube. Utilizing the non-linear process of two-photon absorption on the photocathode, photoelectrons are generated. Details about such an autocorrelator used in Chapter 4 can be found in [43, 44].
Although the characterization in the UV is in general more challenging than

in the visible, shapers have also been implemented. A shaper assisted cross-correlation set-up based on a 2D MEMS (micro-electro mechanical systems, c.f. Section 4.2) has been developed delivering spectral as well as temporal information of the UV pulse [45]. Another technique for the characterization of UV pulses makes use of spectral shearing [46].

4f Set-up

Nearly all techniques used for pulse shaping nowadays are based on spatial light modulation (SLM). As this terminology implies, spatial separation is necessary to perform the modulation. A schematic of a common set-up is depicted in Figure 2.2. The femtosecond pulse is diffracted on a grating and collimated by a focusing mirror. The distance between grating and focusing mirror is equal to the focus length of the mirror. Subsequently, the spectral components are spatially separated and can be modulated with any kind of SLM, e.g. an LCM. Afterwards the spectrum is focused again on a second grating. This set-up is usually called 4f set-up as the distance between the two gratings is in total equal to four times the focal length of the focusing mirrors.
The 4f set-ups utilized in the scope of this work are built in the quasi-Littrow configuration. A Littrow configuration of a grating infers that the light is diffracted back towards the direction from which it came. To separate the diffracted from the incoming beam, the gratings are slightly tilted, i.e. quasi-Littrow, and the focusing mirror is placed centered below the path of the incoming beam. In the whole set-up the optical path is horizontal, i.e. parallel to the optical table, except for the path between grating and focusing mirror.
The effect of the first grating can be interpreted as a Fourier transformation of the incoming light field from the time to the spectral domain according to

$$\tilde{E}_{in}(\omega) = FT\{E_{in}(t)\}. \tag{2.10}$$

Next, the laser field is modulated by the mask, $M(\omega)$, in the spectral domain:

$$\tilde{E}_{out}(\omega) = \tilde{E}_{in}(\omega)M(\omega). \tag{2.11}$$

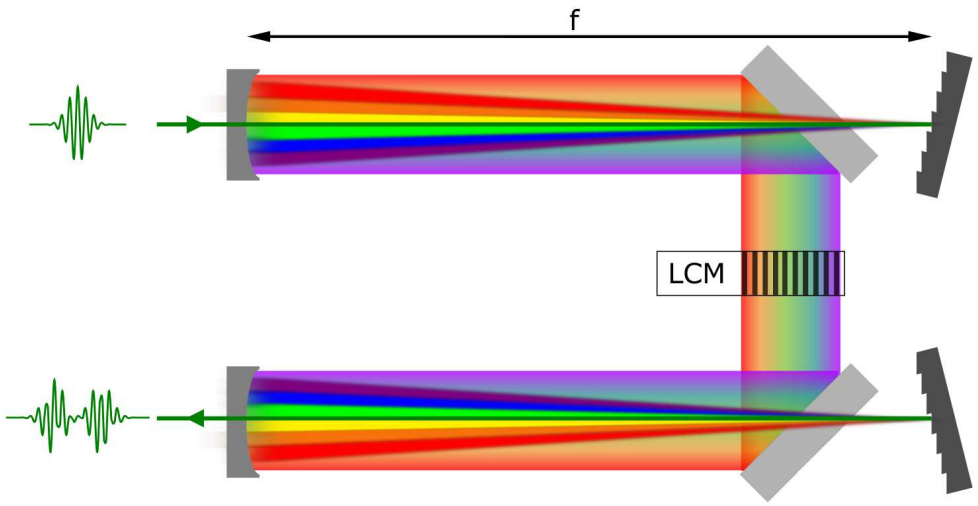

Figure 2.2: Schematic of a 4f set-up with a shaper device (LCM) in the Fourier plane. Here a quasi-Littrow configuration is shown, where the incident and outgoing angle of both gratings with respect to the grooves are identical.

The role of the second grating is the retransformation of the modulated light field to the temporal domain:

$$E_{out}(t) = FT^{-1}\{\tilde{E}_{out}(\omega)\}. \tag{2.12}$$

In principle, the shape of $M(\omega)$ can be arbitrarily chosen. As shown previously in this section, $M(\omega)$ normally consists of phase $\phi(\omega)$ and amplitude $A(\omega)$ modulation, expressed by

$$M(\omega) = A(\omega)exp(i\phi(\omega)), \tag{2.13}$$

which allows the direct modulation electric field.

2.2.2 Working Principle of the Liquid Crystal Modulator

An extensively used type of SLM is the LCM, which consists out of an array of birefringent liquid crystal (LC) cells. In every cell, elongated LC molecules are

placed between two glass substrates with ITO (Indium Tin Oxide) electrodes (Figure 2.3(a)). The alignment layers define the predominant orientation of the

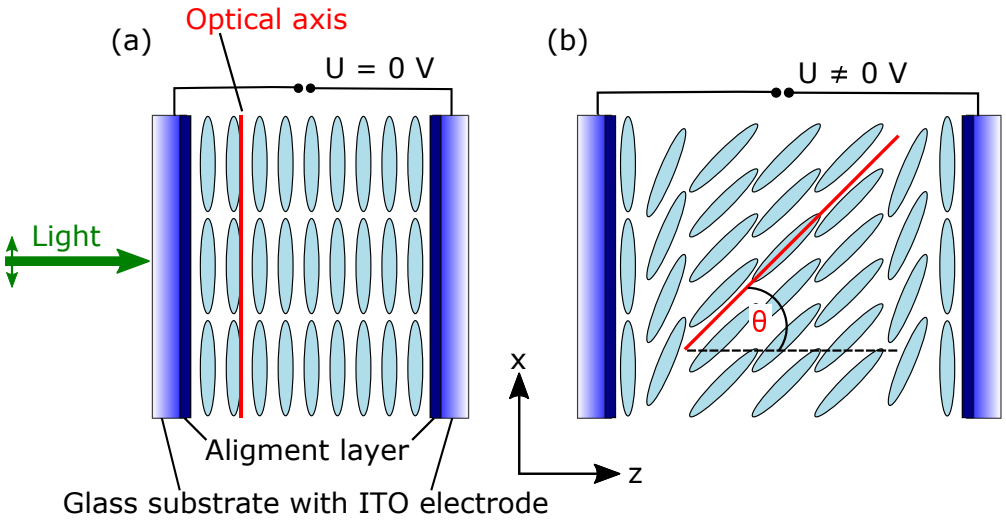

Figure 2.3: Working principle of an LC cell. (a) LCs are placed between two glass substrates with ITO electrodes. Alignment layers ensure the well-defined orientation of the LCs without external electric field. (b) The LCs are tilted by the angle θ due to an external electric field. Therefore, the phase shift introduced by the LCs to light polarized along x can be controlled. Figure adapted from [47].

LC molecules. The optical properties of the LC cell is controlled by an electric field across the cell. The electric field is realized by an AC voltage, U, in form of a bipolar square wave with a frequency of several kHz is necessary (Figure 2.4), which fulfills

$$\langle U(t) \rangle = 0 \tag{2.14}$$

[48, 49]. The reason for the AC voltage is that already small static electric fields destroy the LC phase or cause a electrochemical degradation of the material due to ion contaminants to the surface [50].
The effect of the AC field on the refractive index of the LC molecules can be explained by the optical Kerr effect [51, 52]. The interaction between the AC

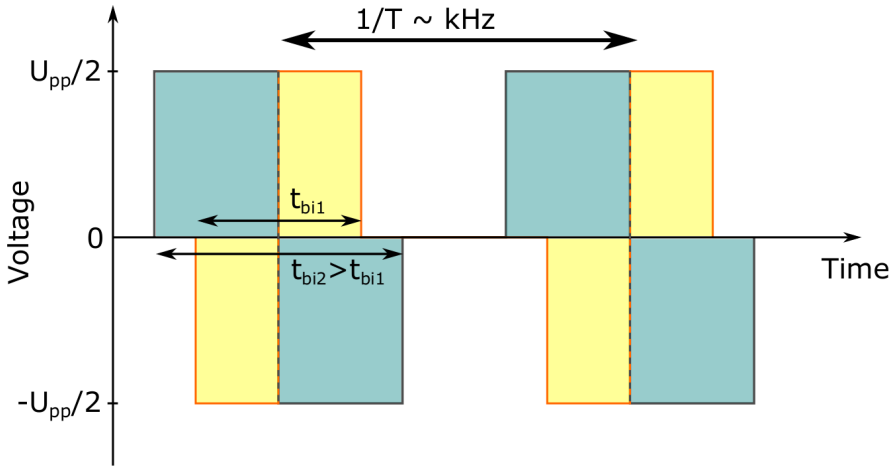

Figure 2.4: Bipolar square waveform to drive the LC cells. The frequency (1/T) is kept constant to several kHu. The intensity of the time-averaged voltage is changed by the pulse width t_{bi} as the colored areas indicate (e.g. $t_{bi2} > t_{bi2}$) to control the refractive index of the LC medium, n and therefore the phase of transmitted light.

field, F[3], and a nonlinear optical medium like the LC molecules can be described by the nonlinear polarization, P,

$$P = \epsilon_0 \left(\chi^{(1)} + \frac{3}{4} \chi^{(3)} |F|^2 \right) F, \tag{2.15}$$

where ϵ_0 stands for the vacuum permittivity and $\chi^{(n)}$ is the n-th order component of the electric susceptibility of the LC medium. The effective susceptibility, χ_{eff}, is the sum of the linear susceptibility, χ_{lin}, and the nonlinear susceptibility, χ_{nl}:

$$\begin{aligned} \chi_{eff} &= \chi_{lin} + \chi_{nl} \\ &= \chi^{(1)} + 3\chi^{(3)} |F|^2. \end{aligned} \tag{2.16}$$

[3]The term F is chosen to distinguish between this electric field and the optical field E. As the frequency of F is constant and F points along the z-axis (in Figure 2.3), the frequency dependence is neglected and the Kerr effect is described in one dimension.

The refractive index, n, is defined as

$$\begin{aligned} n &= \sqrt{1+\chi} \\ &= \sqrt{1+\chi_{lin}+\chi_{nl}} \\ &= n_0\sqrt{1+\frac{1}{2n_0^2}\chi_{nl}}, \end{aligned} \tag{2.17}$$

where $n_0 = \sqrt{1+\chi_{lin}}$ stands for the linear refractive index. A Taylor expansion around χ_{nl} allows to rewrite n as

$$\begin{aligned} n &= n_0 + \frac{3\chi^{(3)}}{4n_0^2 c\epsilon_0} I \\ &= n_0 + n_2 I, \end{aligned} \tag{2.18}$$

where $I = \frac{1}{2}n_0\epsilon_0 c|F|^2$ is the time-averaged intensity of the AC field, F. Furthermore, the nonlinear refractive index, n_2, is defined as

$$n_2 = \frac{3\chi^{(3)}}{4n_0^2 c\epsilon_0}. \tag{2.19}$$

Due to the anisotropy of the LC molecules, the AC field only affects the refractive index along the optical (extraordinary) axis of the molecules, which is therefore also called n_{eo}. The refractive index, n_{ord}, which is perpendicular to the optical axis, i.e. ordinary axis, is unaffected and remains constant. In the case of birefringent LC molecules, the change of n due to the AC field causes an effective tilt of the molecules (Figure 2.3(b)). The angle between the optical axis of the LC molecules and the direction of the electric is called θ and it depends on the intensity, I, of the AC field. The control of I can be realized by changing the peak-to-peak voltage U_{pp}, or in the case of a bipolar square wave the pulse width t_{bi} [53] as shown in Figure 2.4. The period T remains constant.
The controllability of n_{eo} is used to modify the phase of light, which propagates through the LC cell. While the phase of light, which is polarized parallel to the optical axis of the LC molecules, is controlled by θ as visualized in Figure 2.3, which depends on U. The phase shift to light, which is polarized perpendicular to the optical axis, i.e. ordinary-polarized, is constant.

To additionally allow control over the amplitude of the light field, a second layer of LCs and a polarizer[4] in the upcoming optical path are required. Then the optical axes of the two layers are oriented at $\pm 45°$ with respect to the initially linearly polarized light. Therefore, the intensity is equally distributed on two components, one parallel to the ordinary axis and the other one parallel to the extraordinary axis of the LCs. As the assignment of the ordinary and extraordinary components is just inverted in the second layer, the phase of the two polarization components can be changed individually, providing a tool for independent modulation of the phase and amplitude.
The linear optical elements, LC cells and polarizer, can be represented by Jones matrices (see Ref. [54]). The incoming, linearly polarized light wave, E_{in}, is modulated to the outgoing light wave, E_{out},

$$E_{out} = \cos\left(\frac{\Delta\phi_1 - \Delta\phi_2}{2}\right) \exp\left(i\frac{\Delta\phi_1 + \Delta\phi_2}{2}\right) E_{in}, \tag{2.20}$$

with amplitude A and phase ϕ,

$$\begin{aligned} A &= \cos\left(\frac{\Delta\phi_1 - \Delta\phi_2}{2}\right) \\ \phi &= \frac{\Delta\phi_1 + \Delta\phi_2}{2}. \end{aligned} \tag{2.21}$$

The condition $\Delta\phi_1 = \Delta\phi_2$ has to be fulfilled for a pure phase modulation. A and phi are rewritten as the phase shifts, $\Delta\phi_1$ and $\Delta\phi_1$, in two LC layers:

$$\begin{aligned} \Delta\phi_1 &= \phi + \arccos(A) \\ \Delta\phi_2 &= \phi - \arccos(A). \end{aligned} \tag{2.22}$$

The relation between phase shift and applied voltage is determined by a calibration. For this voltage calibration the transmission in the presence of a polarizer after the LCM is recorded in dependence on the voltage for both layers. The procedure is described in detail in the manual of the LCM used [47].

So far the working principle is described for a monochromatic light wave passing

[4] Without polarizer, polarization instead of amplitude and phase shaping is realized

one LC cell. Whenever the LCM is placed at the Fourier plane of a 4f set-up, the spatially dispersed spectral components of a femtosecond pulse pass different LC cells of the array, which are typically called pixels. As each pixel is addressed independently, single spectral components can be modulated individually by applying different AC voltages to different pixels. It allows the shaping of femtosecond pulses by introducing relative phases and relative amplitudes to the spectral components.
For the control of only one property (phase, amplitude or polarization of light) one layer is sufficient. For more complex shaping methods, e.g. control over the whole light field, more complex set-ups were realized [55–57].

2.3 Experimental and Simulation Details

2.3.1 Experimental Details

For the experimental part, femtosecond pulses with a central wavelength of 540 nm and the pulse duration of 14 fs were utilized, which were generated by a one-stage non-collinear optical parametric amplifier (NOPA) [58–61]. Two different LCM models were utilized. Their specifications are summarized in Table 2.1. For all measurements, except for the tailored pulses, maximum voltage was applied to all pixels of the LCM. This way, the spectral and voltage calibration effects on the LCM can be excluded. The small additional chirp due to the dispersive material of the LCM was manually compensated by the optimization of the second grating position within the 4f set-up.
Two aluminum blocks were fixed on the housing of the LCM above and below the LC display. Cooling water, continuously flowing through these aluminum blocks, controlled the temperature of the LC displays. A picture of the LCM with the cooling system surrounded by the 4f set-up is shown in Figure 2.5. For LCM 1 two temperature sensors (according to manufacturer not absolutely calibrated) on both sides of the display monitored the temperature while LCM 2 did not include any temperature sensors. The electronics heated the LCM 1 to 26.0 °C

	LCM 1	LCM 2
Model, manufacturer	SLM-S640d, Jenoptik	SLM-640-D, CRI
Number of pixels	640 double mask	640 single mask
Modulation	Phase and/or amplitude	Phase or amplitude only
Modulation frequency	6 kHz	3.3 kHz
Pixel sizes	96.52 µm x 10.0 mm	100 µm x 5 mm
Response time	N/A	35 ms
Temperature sensors	2 at each side of the mask	no

Table 2.1: Specifications of the two LCMs given by the manufacturer.

without external cooling. Around 30 minutes after starting the circulation of the cooling water, the LCM's temperature decreased to 20.0 °C. The measurements with the cooled LCM 1 and LCM 2 were started after at least 45 minutes in order to ensure stable thermal conditions. The temperature of the lab was kept constant at 21.0 °C ± 0.1 °C.

For the first measurement, the AC traces, the energy per pulse and beam stability (energy passing through pinhole) were recorded simultaneously. The AC was measured with a shot-to-shot commercial autocorrelator NOPA-PAL [36]. In this commercial device, the time delay between the two replicas of the pulse is realized by a continuously moving piezo, i.e. shot-to-shot data acquisition. Therefore, the AC trace over N delays consists of N adjacent laser pulses. To monitor the energy per pulse, the beam was focused on a photodiode (PDA55, Thorlabs). A spatial portion of the beam was detected by another photodiode (PDA155, Thorlabs) for the additional information about the beam directional stability. In a second series of measurements, the collinear second harmonic (SH) signal was detected with a photodiode (PDA155). The difference in measuring the AC trace and the SH signal is visualized in Figure 2.6

Each of these measurements was performed under several experimental conditions. First, the light directly from the NOPA, i.e. without 4f set-up, was measured as a reference. Second, the beam was sent through the non-cooled LCM and the same measurement as before was acquired. Next, the LCM was cooled and the measurement was performed with the cooled LCM. Finally, the first measurement without LCM was repeated to control and exclude any possible drifts of the laser influencing the results.

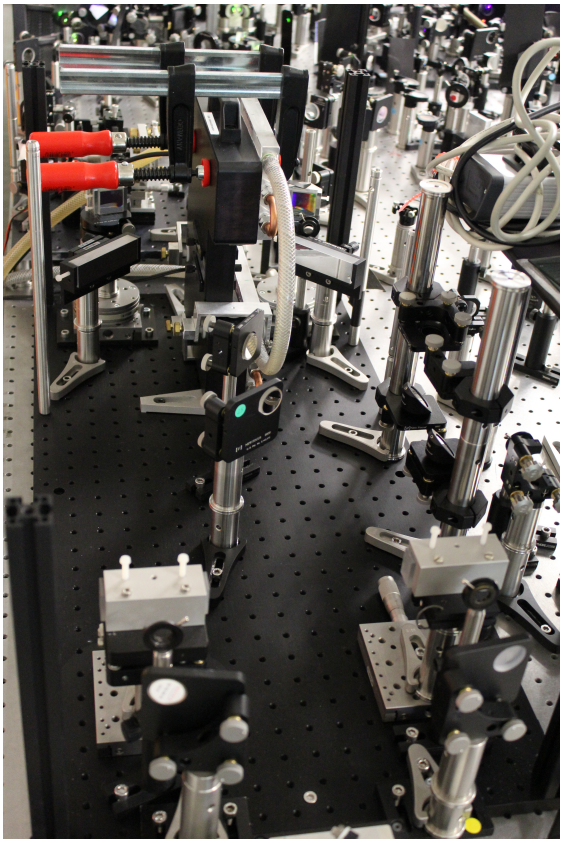

Figure 2.5: Picture of the LCM with the cooling system surrounded by the 4f set-up.

2.3.2 Simulation Details

The second-order intensity autocorrelation was simulated numerically with various types of noise, which were used to modify the spectral phase using Lab2 [62], an add-on to LabVIEW. Input for the simulation was a Gaussian pulse spectrum (512 points) with the same central wavelength and spectral width as in the experiment. Moreover, the geometry of the 4f set-up was a direct input parameter set. To model the second-order process, non-depleted three wave mixing was implemented with optical parameters like thickness and cutting angle of the nonlinear crystal comparable to the experiment. The initial laser pulses (i.e. without LCM) were chosen noise-free since the focus was on the effect of the LCM and the temperature dependence. Noise was set as a direct

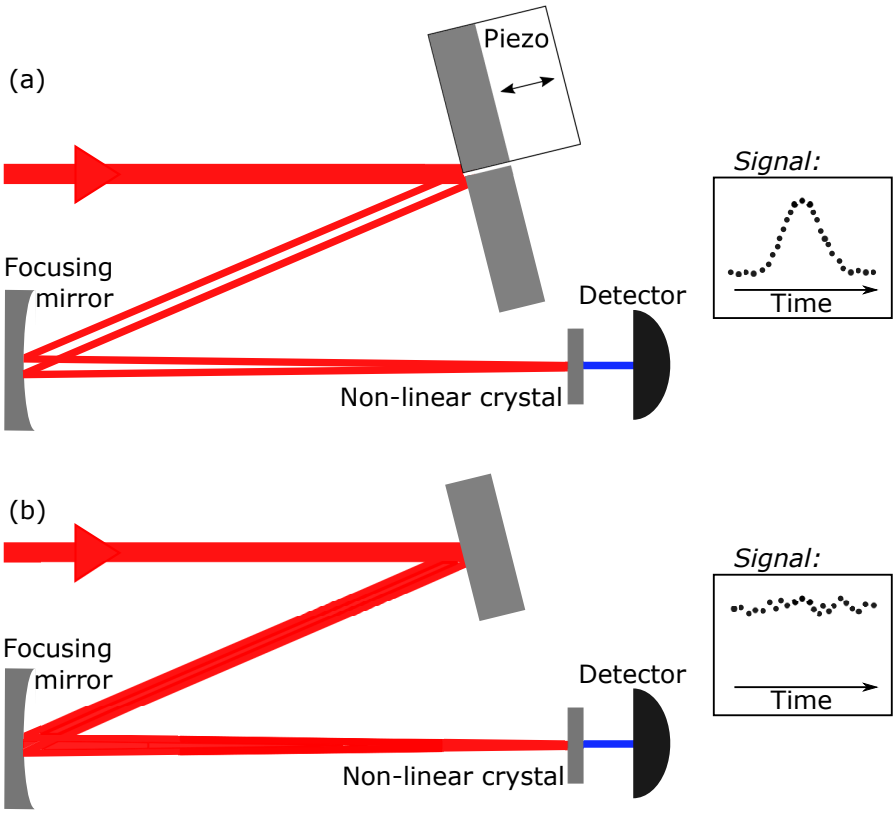

Figure 2.6: Schematic set-up for acquiring the AC trace (a) and the SH signal (b). For the AC trace, the initial pulse is split in two replicas, which are focused into the non-linear crystal. The non-linear signal is generated by the temporally overlapping parts of both replicas. The temporal overlap is varied from shot to shot by a piezo stage. For the SH signal adjacent data points are measured under the same experimental conditions.

input parameter for the spectral phase $\phi(\omega)$ of the laser pulses. Therefore, the spectral electric field $E(\omega)$ was modified according to

$$E(\omega) = E_0(\omega)\exp\{i[\phi(\omega) + \phi_{noise}(\omega)]\}. \tag{2.23}$$

Two different approaches were used to simulate the experimental noise. The first approach uses different kinds of noise (uniform noise with various magnitudes as well as Brownian ($1/f^2$) noise). The noise was generated independently for each spectral component (pixel). In a second approach, a coupling between the pixels was implemented. The coupling between the pixels was generated

by using six supporting spectral components which were distributed evenly among the spectral components of the pulse. An initial phase for each of the six supporting spectral components was generated by Brownian noise, which was then multiplied by a vector containing N samples in time with the same experimental frequency dependence (Section 2.4.1). From these data, the noise for all pixels was calculated via spline interpolation. To distinguish between the cooled and non-cooled case, the magnitude of the noise was varied by a factor of two. Thus, the limits for the phase were set to be $\phi_{\text{noise}}^{\text{max}} - \phi_{\text{noise}}^{\text{min}} = 1.2\,\text{rad}$ for the non-cooled case and 0.6 rad for the cooled case. 150 shot-to-shot AC traces were generated in a time window of ±150 fs with a temporal resolution of 2 fs.

2.4 Results

The following section contains experimental results on the second-order intensity autocorrelation traces to visualize the effect of the phase noise, second harmonic signals to investigate the time-dependence of the phase noise and, finally, effects on transient absorption measurements. The goal of the subsequent numerical simulation of the autocorrelation traces is to reproduce the experimental data and to get a deeper understanding about the characteristics of the phase noise and its origin.

2.4.1 Experimental Results

Shot-to-Shot Autocorrelation Traces

Due to its straightforward implementation, the AC traces are detected to characterize the optical instabilities due to the LCM from shot to shot. The shot-to-shot AC traces are compared in Figure 2.7 for the three different cases (without LCM, with cooled LCM and non-cooled LCM). The AC traces without LCM mainly fluctuate in their maximum height, while the shape and width remain nearly the same. This behavior is very similar for the cooled LCM. For the non-cooled

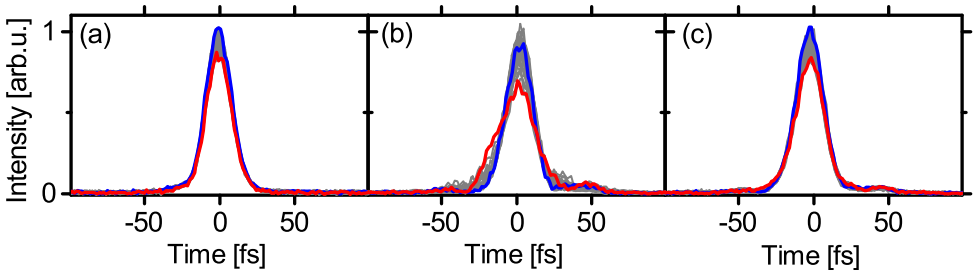

Figure 2.7: Autocorrelation traces measured (a) without, with the (b) non-cooled and (c) cooled LCM. Particular traces are selected and highlighted in color.

LCM, however, the overall AC shape strongly differs. For some traces, wings of different shape and intensity appear on both sides of the traces. This instability can be numerically quantified by fitting the traces to determine the pulse duration. The individual traces are fit (not shown) with a Gaussian to determine the pulse duration via the width of the Gaussian. Thus, the relative standard deviation of these values is used as a measure for the stability of the shape of the laser pulses. For the measurement without LCM, the pulse duration has a stability of 0.65 %. The non-cooled LCM significantly increases the value to 7.2 %; however, the cooling reduces it to 2.0 %.

The instability is not only present in the AC traces with maximum voltage at all pixels of the LCM (Figure 2.7), but can also be clearly observed in AC traces of shaped pulses (Figure 2.8). Linear chirp (100 fs^2) and multipulse (interpulse spacing $b = 100fs$) are chosen which are typical for experiments with LCMs [12, 13, 17, 63]. The instability of the linearly chirped pulse for the non-cooled LCM is for this example stronger than for the unshaped pulse. For cooling the LCM, a clear improvement is achieved for both parametrizations with a final instability comparable as for the unshaped pulse. Although this clearly shows that the instability as well as the cooling effect is independent of the calibration of the LCM and of the voltage control of the single pixels, the instability has different effects on different parameterizations. For example, for multipulse parameterization, the relative amplitudes of the subpulses are strongly affected (by almost a factor of 3), while the interpulse separation is only slightly disturbed (by less than 5 %).

Optical instabilities in the AC signal as observed in Figure 2.7 and Figure 2.8

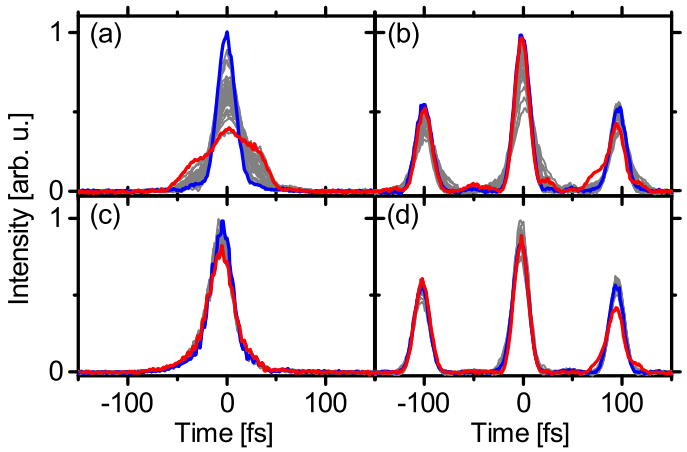

Figure 2.8: Autocorrelation traces with a non-cooled (a, b) and cooled (c, d) LCM for different phase parametrizations; (a, c) chirped pulses second-order Taylor (100 fs^2) and (b, d) multipulses (interpulse spacing 100 fs). Particular traces are selected and highlighted in color.

do not necessarily need to be caused only by instabilities of the optical phase, but they can also be caused by instabilities in e.g. the pulse energy, the beam direction after the LCM as well as beam overlap during the AC process. In order to verify and exclude other origins for the instabilities in the AC traces, three additional measurements (energy, pointing stability and SH signal) are performed. The absolute energy and pointing of the beam going through LCM are also measured shot-to-shot (not shown). The relative standard deviation for both quantities over 20000 pulses is mainly determined by the laser-typical noise (1.1 %) and does not change whether a mask is used or whether it is cooled or not. Consequently, these quantities do not cause the instabilities seen in the AC traces of the non-cooled LCM. The SH signal alone is equally sensitive to the optical phase, but it is not sensitive to other parameters like beam pointing stability and beam overlap in the AC process. Differences for the cooled and non-cooled LCM are clearly visible in the pure SH signal of both LCMs. Without LCM, a sequence of 20000 pulses has a relative standard deviation of 1.3 %. This value increases to 6.7 % for both non-cooled LCMs. Cooling the LCM improves the stability to 4.9 and 4.3 % for LCM 1 and LCM 2, respectively. These results clearly show that the instability detected in the AC and SH measurements have the same source, i.e., the optical phase of the laser pulse.

Time Dependence of the Phase Noise

To gain more insight into the instability's time dependence and the changes caused by the LCM and temperature dependence, the power spectra of the SH signal detected for both LCMs are determined shot-to-shot. The spectra look very similar for both LCMs. The power spectra on a linear scale (Figure 2.9(a,b))

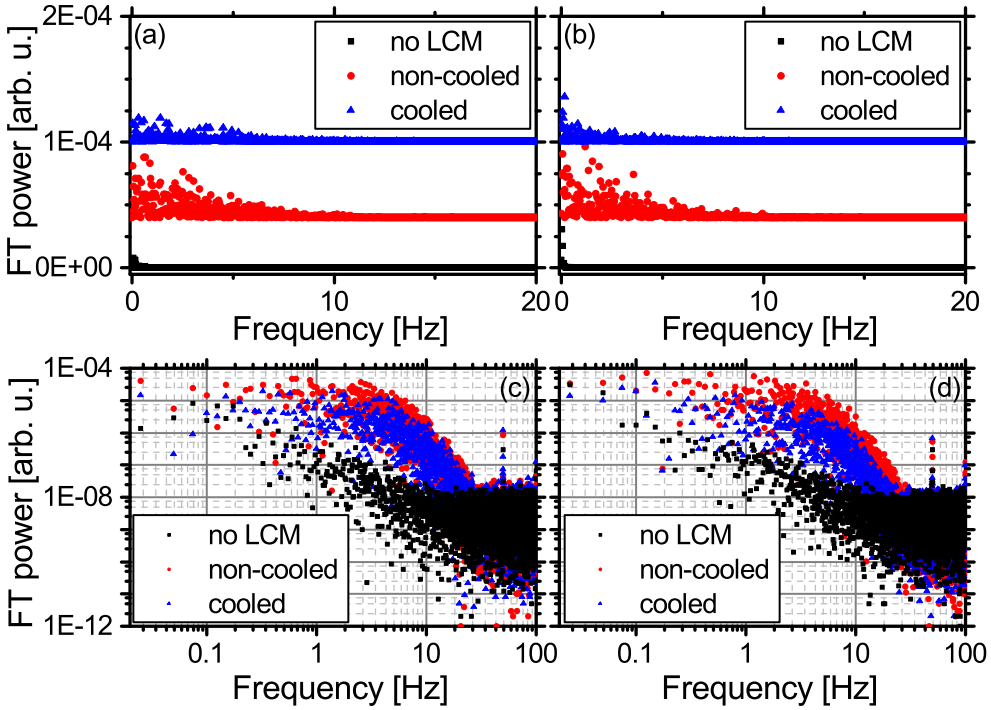

Figure 2.9: Power spectra of the experimental SH signal for LCM 1 (a,c) and LCM 2 (b,d) on a linear (a,b) scale without LCM (black squares), after the non-cooled LCM (red circles) and after the cooled LCM (blue triangles). The spectra look very similar for both LCMs. The linear scale in Figure 2.9(a) clearly illustrates the impact of the LCM and of its cooling. The log-log representation of the same data sets (c,d) shows that without LCM, the spectrum scales with $1/f^2$ for $f < 27$ Hz. With LCM frequency components contribute uniformly for $f < 1$ Hz. Up to $f = 27$ Hz, the spectra scale with $1/f^n$ with n changing from 2 to 5. The shape of the power spectrum for the cooled and non-cooled LCM is the same but the power of the components differs for $f < 27$ Hz. In all cases, the components for $f > 27$ Hz are distributed uniformly with powers two orders of magnitude smaller than in the low-frequency range.

mainly show components with frequencies $f < 1$ Hz for the measurement without LCM. Frequency components up to $f = 10$ Hz contribute clearly to the power spectra for the experiments with LCM. The components for the non-cooled LCM are on average twice as strong as for the cooled LCM. The linear scale in Figure 2.9(a) clearly illustrates the impact of the LCM and of its cooling. The same power spectra are plotted on a log-log scale (Figure 2.9(c,d)). This representation shows higher frequency components and the frequency dependence in more detail. Without LCM, the spectrum scales with $1/f^2$ for $f < 27$ Hz. Such a frequency dependence is typical of laser systems [64–66]. In the cases with LCM (cooled and non-cooled), components for $f < 2$ Hz are constant and most dominant. Up to $f = 27$ Hz, the spectrum scales with $1/f^n$ with n changing from 2 to 5. The shape of the power spectrum for the cooled and non-cooled LCM is the same but the power of the components differs for $f < 27$ Hz. In all three cases, the components for $f > 27$ Hz are distributed uniformly with powers two orders of magnitude smaller than in the low-frequency range.
Although the architecture of the two LCMs is not exactly the same (LCM 1 has two displays while LCM 2 has only one), the experimental results above and the observed temperature dependence undoubtedly shows that the same physical mechanism is behind the experimental phase instability. A more quantitative comparison between a single and double mask is at the moment not possible as there are too many unknown differences between the two LCMs as e.g. the effective thickness of the LCs, their material and properties as well as the modulation frequency.

In summary, the experimental AC traces with unshaped and tailored pulses (Figures 2.7 and 2.8) show two important features to understand the source of the phase instability. The first one is the strong temperature dependence, which clearly indicates a temperature-dependent physical mechanism. The second one, which is not as obvious as the first one, is especially depicted in Figure 2.7(b). Not all AC traces are equally affected, i.e. there are traces which strongly differ (e.g. the red trace) from a Gaussian shape while others (e.g. the blue trace) do not. Since a single AC trace takes more than 250 ms (250 laser pulses at 1 kHz repetition rate) to acquire, this behavior suggests that a low-frequency noise must be the main source for the experimental phase instability. This is

corroborated by the power spectra (Figure 2.9), which shows the presence of low-frequency components with higher amplitude when the LCM is used. Perhaps even more interesting than that, the behavior observed in Figure 2.7(b) also suggests an additional feature of the phase instability. The asymmetric traces in Figure 2.7(b) suggests that several spectral components of the laser spectrum passing through different pixels of the LCM must be under the effect of a similar phase instability. Based on these considerations, a numerical noise model is implemented to reproduce the experimental shot-to-shot AC with cooled and non-cooled LCM.

2.4.2 Simulation Results

In the numerical simulation, several approaches in respect to the noise are implemented.
The first one is uniform noise, which is applied to all spectral components. The amplitude of the noise is varied by changing the range of the phase between ± 0.5 and ± 2 rad. The resultant AC traces are shown in Figure 2.10. The peak intensity of the traces decreases with increasing noise amplitude. Variations between single AC traces become only visible, when the peak intensity is already decreased by a factor of two. However, no asymmetries appear as in the experimental AC traces.
The next approach is based on completely uncorrelated noise with $1/f^2$ power spectrum. Also in this case, the simulated AC traces are affected only in the intensity and the traces are symmetric. These results hold for noise with intensities over several orders of magnitudes as well as for other power spectra with higher noise order e.g. $1/f^3$ or higher. All these types of noise can be excluded as reason for the temperature dependence of the experimental AC traces as there is no decrease in the AC intensity is observed.
Based on the experimental results, a more complex approach is used, where $1/f^2$ noise with a coupling between pixels is combined with a noise amplitude over all pixels (see Section 2.3.2 for details), and good agreement with the experiment could be achieved. The amplitude of the noise is chosen to introduce 1.2 radian as a maximum additional phase in order to reproduce qualitatively the experi-

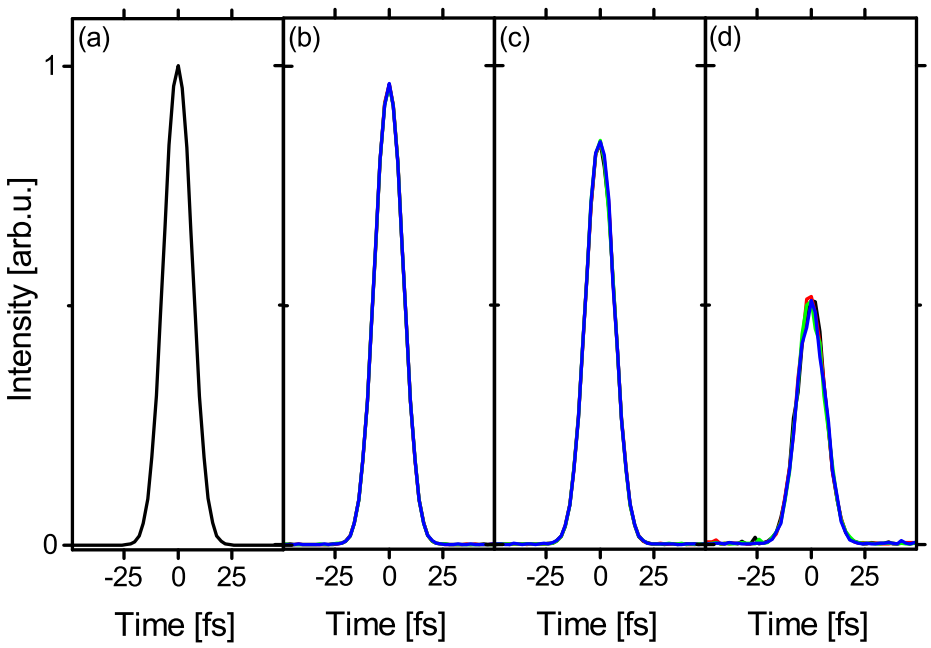

Figure 2.10: AC traces for a noise-free (a) phase and when the amplitude of the noise is varied by changing the range of the phase to (b) ± 0.5, (c) ± 1 and (d) ± 2 rad. The peak intensity of the traces decreases with increasing noise amplitude. Variations between single AC traces become only visible, when the peak intensity is already decreased by a factor of two (d).

mental AC. In the numerical simulation, the cooling effect is indirectly simulated by reducing the noise amplitude by a factor of 2. Under these assumptions, Figure 2.11 shows the simulation results for all three parametrizations (TL, chirp, multipulse) under cooled and non-cooled conditions. In a very good agreement with the traces depicted in Figures 2.7(b) and 2.8(a)-(b), Figure 2.11(a)-(c) displays the same asymmetrically distorted traces observed in the experimental traces. Moreover, the distortion is strongly suppressed when the noise amplitude is halved (Figure 2.11(d)-(f)), which qualitatively replicates the experimental temperature dependence.

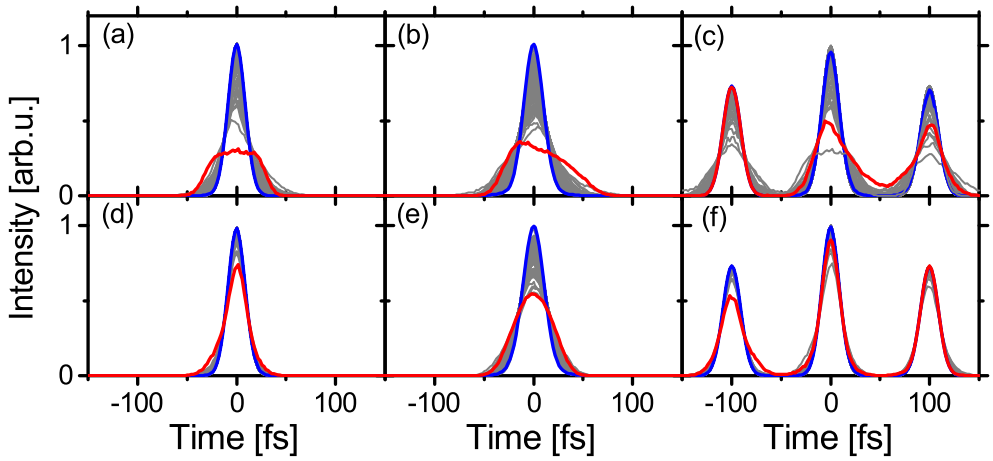

Figure 2.11: Simulation of shot-to-shot AC traces for the non-cooled (a)-(c) and cooled (d)-(f) cases for different parametrizations of the phase: (a), (d) TL, (b, e) linear chirp of 100 fs^2 and (c), (f) multipulse with a interpulse distance of 100 fs. Particular traces are selected and highlighted in color.

2.5 Discussion

After the numerical simulation of the experimental temperature dependence, there is still a central question about under which experimental conditions the LCM phase noise as described above can be observed or even minimized.
In time-resolved spectroscopy, there are basically two ways of averaging optical signals, which are also crucial for neighboring research fields like coherent control. One way is based on the N-times acquisition of a given optical signal in synchronization with the laser repetition frequency without changing any parameter (e.g. delay between pump and probe). After these N signals are acquired and averaged, parameters are changed (e.g. a new delay between pump and probe). Since the scanning of parameters takes place step-wise, this is called step scan. Obviously this way of averaging can be very sensitive particularly to low-frequency noise for large N. Another approach for averaging signal often used to overcome low-frequency noise is the so-called rapid scan technique. In this method, only one single optical signal (i.e. one laser shot) is acquired before experimental parameters are changed. This way, a single scan is made of only a few number of laser pulses. The averaging over many (typically tens or hun-

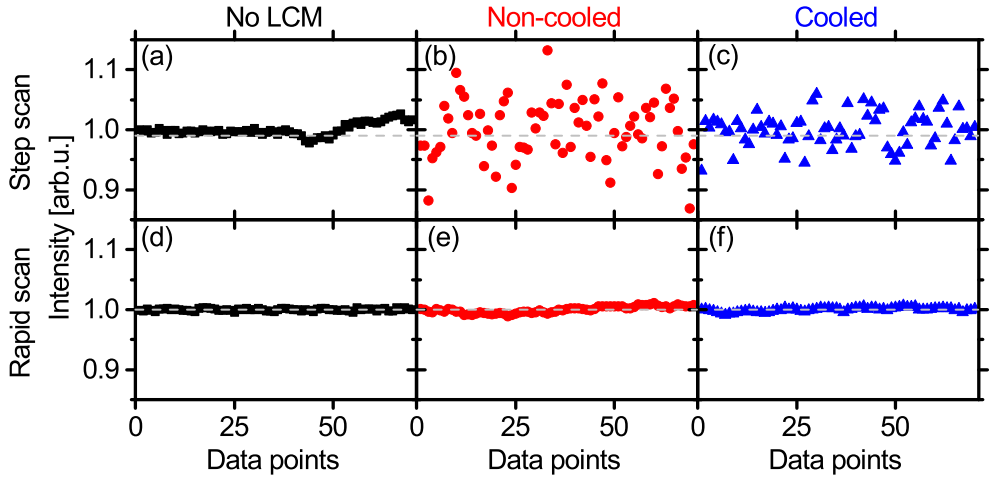

Figure 2.12: A comparison between (a-c) step scan and (d-f) rapid-scan averaging. For both schemes 70 data points are calculated from the SH signal of 4900 adjacent laser pulses. (a), (d) without LCM (black squares), with (b, e) non-cooled (red dots) and (c, f) cooled (blue triangles). The gray dashed line is a guide to the eye for the deviation of the points from the mean over the signals from all 4900 laser pulses.

dreds) of scans leads to a data set, which is free of low-frequency noise, i.e. like applying a high-pass filter. This technique of averaging optical signals has been exploited in, for example, many multidimensional time resolved spectroscopies [67–69].

First, the average scheme should be discussed for a sequence of 4900 SH signals. The low-frequency noise described for LCMs in the previous sections can be strongly suppressed when a rapid-scan averaging is applied. To illustrate the influence of the averaging on the LCM phase noise, the experimental SH data are evaluated with these two averaging schemes, namely rapid and step scan (Figure 2.9). In the step-scan averaging of the SH intensity (Figure 2.12(a-c)), each data point is the average of $N = 70$ laser pulses, which are detected successively. For rapid scan (Figure 2.12(d-f)), each data point is also the average of $N = 70$ laser pulses but not detected successively (c.f. Figure 2.13). The differences between the averaging approaches and the effect on suppression of the LCM phase noise are striking. In all cases (no LCM, non-cooled and cooled LCM), the instability of the SH signal averaged with rapid scan is by one order of magnitude smaller than with step scan. In general, the data show that using rapid-scan averaging

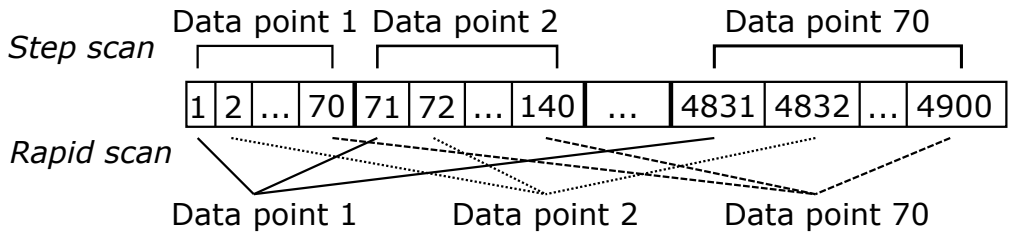

Figure 2.13: Visualization of step-scan and rapid-scan averaging for the same set of data consisting of 4900 shots. Adjacent shots are averaged by step scan for a data point, while shots, which are distributed across the sequence of data, are averaged by rapid scan for a data point.

(Figure 2.12(d-f)) leads to an almost noise-free measurement, independent of whether the LCM is cooled or not. A noteworthy observation concerns the rate of the rapid-scan averaging. Here $N = 70$ is chosen, which means that signals separated by 70 ms from each other are averaged as a data point which allowed an almost complete suppression of the LCM phase noise. This parameter must be carefully chosen according to the power spectrum and its main spectral contributions though.

Another central aspect is the consistent results for the SH intensity for both LCMs. It hints that the LCM phase noise should appear in all kind of experiments, in particular when step-scan averaging is used. However, to our knowledge, this has not been the case. There are several examples of e.g. control experiments using similar LCMs, with reported phase stability orders of magnitudes better than the ones recorded here [22, 23]. The explanation for that resides on experimental parameters like the laser repetition rate and the tailored spectral bandwidth. Experiments using sources with repetition rates of several hundreds of kHz up to MHz can easily average well more pulses than what is feasible with kHz sources (like in this work). Moreover, averaging e.g. 70 laser pulses with an 80 MHz laser takes less than 1 µs, while for a 1 kHz laser it takes 70 ms. This illustrates very clear that high repetition sources are well less sensitive to low-frequency noise than sources with low repetition rate. More important than that is perhaps the tailored spectral bandwidth. Most experiments using LCM are still performed using spectral sources with a bandwidth of a few hundreds of wavenumbers spectrally spread over several hundreds of pixels of the

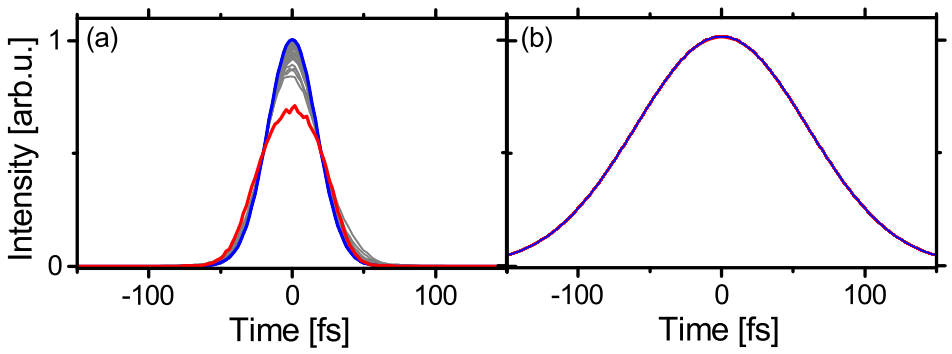

Figure 2.14: Simulation of shot-to-shot SHG-AC traces for the non-cooled, TL cases for pulses with pulse durations of (a) 30 fs and (b) 100 fs. Particular traces are selected and highlighted in color. Phase noise was the same as in Figure 2.11(a)-(c).

LCM. Very few experimental works have been performed with bandwidths over 1000 cm^{-1} like in this work. A phase noise of few radians per pixel, as observed and simulated here, has a very small effect on a laser with smaller bandwidth. For example, this is further illustrated in Figure 2.14. While a 30 fs pulse is still affected by the phase noise, which is used for the simulation shown in Figure 2.11(a)-(c), a spectrally narrow 100 fs pulse remains completely unaffected.

Finally, possible origins of the phase instability still remain to be discussed. The working principle of LCMs is based on the change of the phase by the orientation-dependent refractive index of the birefringent nematic LC molecules. The phase control is realized by an external square wave voltage. One cannot exclude without further experimental work, that nematic LCs under such an electric field are completely oriented without any additional orientation dynamics. A small variation of the orientation can cause large changes in the birefringence, and therefore, change in the optical phase. For example, the phase instability experimentally observed and simulated in this work is on the order of one radian. This amplitude corresponds to a variation of about 10° in the LC orientation, according to the LCM manufacturer and calibration curves. Therefore, one plausible cause for the phase instability is the ability of LCs to perform a small amplitude libration-like movement constrained by the applied control voltage. Cooling of the LCM electronics itself may also play a role in the phase

instability if the amplitude of the applied square wave is not stable, affecting the actual phase. However, the fact that the phase instability occurs for two LCMs from different manufacturers and with different electronics, hints strongly at a LC molecular orientation origin. This assumption is furthermore supported by the observed temperature dependence. In the literature about the general properties of nematic LCs, a temperature dependence of the orientational order and mobility is stated; while the orientational order decreases with increasing temperature, the mobility increases [70, 71]. The mobility of the LCs along the molecular axis can be even observed as flicker under the microscope [72]. The flicker increases with increasing temperature. The fact, that it is observed in real time, indicates that these movements occur with a typical rate of a few Hz to several tens of Hz. Such a rate matches the frequency of the dominant noise observed in the SH signal (Figure 2.9). This agreement confirms that the movement of the LC molecules causes the phase noise and that the latter is observed in the experiments. It is interesting to note that although the reduction of the LC orientation mobility via cooling leads to an increase of the phase stability as shown above, cooling of the mask is not always desirable in optical applications. Rapid phase mask changes by overdrive switching, for example, is ultimately limited by the molecular re-orientational movement of the LC [31], and cooling in that case would constrain how fast the phase mask can be changed. Therefore, the optimal temperature of the LCM strongly depends on the application. An improvement for reliable performance for various applications could be a shaper with temperature control, which is currently not provided by any company.
Beside the origin of the phase instability, the coupling between pixels across the LCM, which was required for the simulation of the experimental SHG-AC results, is also surprising. Orientation coupling between nematic LC over several mm even cm has not been reported and is above the scale typically known for LC coupling. A potential candidate for the source of this coupling is the LCM electronics itself. To generate several hundreds of various AC voltages and to apply these to the LC pixels requires more than one circuit board. Therefore, probably a certain number of AC voltages shares the same temporal phase, which can differ from the one generated by another board. As the generation of AC voltages is not synchronized with the laser source and the propagation time of the light through the LCM is typically smaller than 100 fs, such temporal phase

shift could be the reason for the coupling between the pixels. However, this possible explanation is only relevant under the assumption that the orientation and therefore the refractive index of the LC molecules is sensitive to the intensity of the electric field within a period of the AC field (Figure 2.4), which is not sure. For this reason, the coupling is still an open question and should be investigated in a future work.

2.6 Conclusion

Precise and noise-free tailoring of ultrashort laser pulses with LCM is a challenging experimental business. In this work, a low-frequency phase noise generated by LCMs is reported for the first time. This phase noise leads to very strong pulse deformations, even when no phase parameterization is applied. The experimental power spectrum and the strong temperature dependence of that phase noise hints at a $1/f^2$ noise component due to the thermally activated libration of the nematic liquid crystal molecules in the LCM. This is further corroborated by a numerical simulation of an autocorrelation using a phase noise with similar features. In spite of the large effect of this phase noise on the experimental laser output of the LCM, it is possible to strongly minimize it by a careful choice of experimental parameters. The first parameter is the operating temperature of the LCM, which improves the shot-to-shot stability of the output tailored pulse by a factor of two, when the LCM is externally cooled. The second parameter is the signal averaging approach. A rapid-scan averaging leads to a suppression of the low-frequency phase noise by an order of magnitude. The combination of these two strategies is a central knob in order to apply LCMs to spectrally broad laser pulses with high precision. It offers a promising improvement for the application of shaped pulses, e.g. for coherent control experiments where only small differences in the shaped pulses are important.

Coherent Control by Excitation with Chirped Multipulses

3

In this chapter, a systematic study of coherent control within a simple molecular system is presented The goal was to selectively excite vibrational wave packets on the ground and excited electronic states, as well as to manipulate the population in both states, in Nile Blue by spectral and phase shaping of femtosecond laser pulses. The resultant enhancement of population and vibrational coherence in the ground and excited states are quantified and should be seen as an indicator of how successful coherent control of these two states can be.
The chapter starts with the motivation for the project including related key results reported in the literature. Next, the concept of experimental method, transient absorption (TA) spectroscopy, is explained, followed by the description of the possible contributions to the signal and the experimental set-up. Afterwards, the acquisition and processing of broadband TA data in combination with rapid-scan averaging are outlined. Finally, the the single steps of data analysis are depicted with the goal to determine enhancement factors due to shaped excitation. General results from the TA measurements follow this, whereby various effects on the vibrational coherence and finally the enhancement due to shaped pulses are presented. These results are discussed in detail, as well as compared with observations reported in the literature, and subsequently summarized.

3.1 Motivation

Control experiments in the low-intensity regime are of high interest as light-driven reaction in nature typically occur at very low intensity. The goal is to understand the underlying processes and to even control them by examining them under comparable intensity conditions as in nature but with coherent light sources. In the past, the parameters for successful control experiments have often been found by chance, and most probably there have been many trials which failed. Nevertheless, there were well-known mechanisms stated in literature. Typical examples of control parameters, which influence population and vibrational coherence, are linear chirp and multipulse excitation. Nowadays, it is regarded that a negatively chirped broadband excitation pulse enhances the vibrational coherence in the ground state compared to a transform-limited pulse [12]. To examine the second mechanism, multipulse excitation, a pulse train of transform-limited pulses is generated, where the interpulse spacing is equal to the period of a molecular vibrational mode. The first application of such multipulses was the filtering for one specific mode, which matches the interpulse distance, while other modes are suppressed. Such filtering was utilized for selective excitation of modes in a crystalline sample [73]. Furthermore, multipulses allow the selective excitation of modes in the ground and excited state in the gas phase using four-wave-mixing as shown in Ref. [74, 75]. Later the filtering effect was shown in single-beam CARS [76, 77]. The phenomenon of multipulse filtering is especially promising as the pulse duration of the single subpulses is the same while the interaction is spread in time. It can be seen as an alternative to spectral narrowing, where the excitation spectrum is made narrower to ensure that only specific modes are addressed in order to gain selectivity [78–80]. However, the drawback of spectral narrowing is the decrease in temporal resolution. The idea to enhance vibrational modes by use of multipulses arose later [14, 81]. In Ref. [14], the spectral detuning of the excitation, came into play as an additional parameter. This experimental and theoretical work shows that a near-resonant multipulse enhances the population and the vibrational coherence in the excited state compared to a transform-limited pulse [13, 14]. For various experimental studies, which examined the vibrational coherence in

the ground or excited state, the dye Nile Blue or other oxazines were chosen as prototype molecules [12–14, 82–85]. These molecules offer the advantage of a dominant low-frequency mode around $600\,\mathrm{cm}^{-1}$. Due to the dominance of the mode around $600\,\mathrm{cm}^{-1}$ in Nile Blue, the molecule was also addressed as a prototype molecule in a theoretical study to test a quantum-mechanical theory. It was possible to simulate observed transient spectra successfully with a one-dimensional system of two displaced harmonic potential surfaces [86]. This simulation shows not only that the dynamics is dominated by this single mode but also that mainly two electronic states contribute to the dynamics of Nile Blue. That this approximation is reasonable is also confirmed by the agreement between experiment and theory, where Nile Blue is simulated with a non-perturbative, time-dependent density matrix approach for a four-level system [14].

In the scope of the systematic study within this thesis, several questions are addressed. First, the effect of linear chirp on the ground-state vibrational coherence is examined in dependence on the excitation spectrum to evaluate if the Based on these various works stated in literature, a systematic study was performed in the scope of this thesis. It examined the enhancement of population and vibrational coherence in the ground and excited state of Nile Blue. The temporal shape as well as the spectrum of the excitation pulse were parameters in this study. The excitation spectrum was tuned across the absorption spectrum of Nile Blue. The temporal shaping included linearly chirped pulses, multipulses and the combination of these two to examine the interplay of these two types of temporal shaping. The main goal of the study is to provide a guideline for parameter sets, which allow the successful performance of control experiments in the future.

3.2 Experimental Method: Transient Absorption Spectroscopy

The experimental method for the control study is transient absorption (TA) spectroscopy. TA allows to monitor molecular processes on the femtosecond to nanosecond scale. Examples for these processes are energy transfer, electron transfer and radiative decay. In a typical TA experiment, a first pulse excites a fraction of sample molecules initiating a photophysical reaction or photochemical process. The resultant new electronic configuration of the excited molecules leads to a modified absorbance of the sample. The difference in absorbance is sampled by a second pulse, called probe, as a change in transmittance. The temporal delay between excitation and probe pulses is varied by elongating the relative optical pathway. This approach allows for measuring the temporal evolution of the initiated process and therefore, to unravel photochemical properties of the system.
To resolve ultrafast molecular dynamics with this technique, femtosecond pulses are required. Such pulses need a certain spectral width as discussed in Section 2.2.1. Therefore, on top of the electronic excitation, a manifold of vibrational levels can be coherently excited, whenever the spectrum of the excitation pulse exceeds energetic separation of the vibrational states. The initiated wave packet performs coherent oscillations on the potential energy surface (Figure 3.1). These oscillations, also known as quantum beats, appear with the characteristic frequency of the addressed molecular mode. Their strength depends on the number of vibration levels included. They usually disappear within a few picoseconds due to damping and vibrational dephasing.

Experimentally, the change of the absorption spectrum is measured via the optical density, OD, of the sample. In the static case, the optical density can be described by the Lambert-Beer law as

$$\begin{aligned} OD &= c\varepsilon d \\ &= \log\left(\frac{I_0}{I}\right), \end{aligned} \tag{3.1}$$

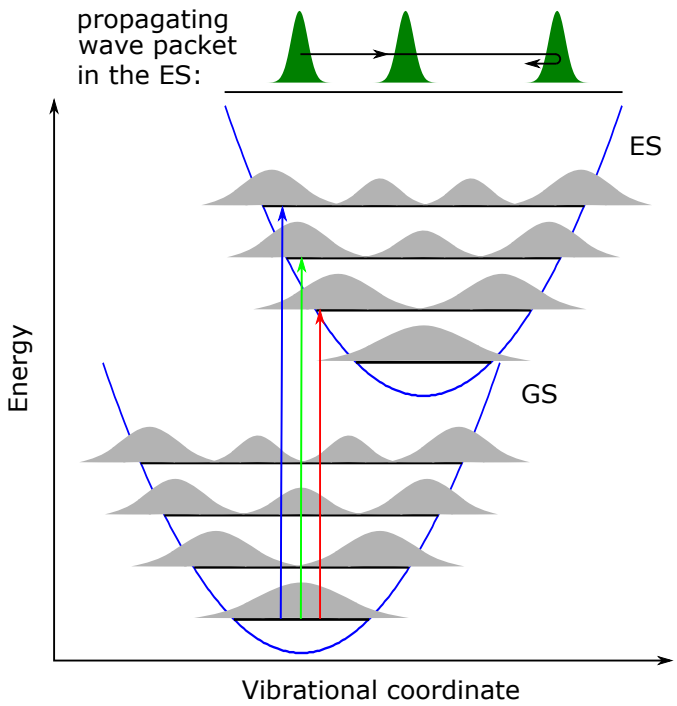

Figure 3.1: Visualization of vibrational coherence. A broadband pulse (indicated by three colored arrows) excites several vibrational levels in the excited state (ES). The resulting wave packet propagates on the potential energy surface with a frequency, which is equal to the spacing between the vibrational levels.

where c is the concentration of the absorbing substance, ε is the molar extinction coefficient, d is the path length in the sample and I_0 (I) is the intensity of the ingoing (outgoing) probing light. To observe a dynamical change in optical density, ΔOD, first the initial excitation pulse passes the sample and after the time delay τ the probe pulse passes the same sample volume and it is detected. As a reference, the probe pulse is additionally measured, when the excitation pulse did not pass the sample. The effect of the initial excitation is determined by subtracting the optical density without (OD^{Off}) from the one with (OD^{On}) excitation:

$$\begin{aligned} \Delta OD &= OD^{On} - OD^{Off} \\ &= \log\left(\frac{I_0}{I^{On}}\right) - \log\left(\frac{I_0}{I^{Off}}\right) \\ \Delta OD(\lambda, \Delta t) &= \log\left(\frac{I^{Off}(\lambda,\tau)}{I^{On}(\lambda,\tau)}\right). \end{aligned} \tag{3.2}$$

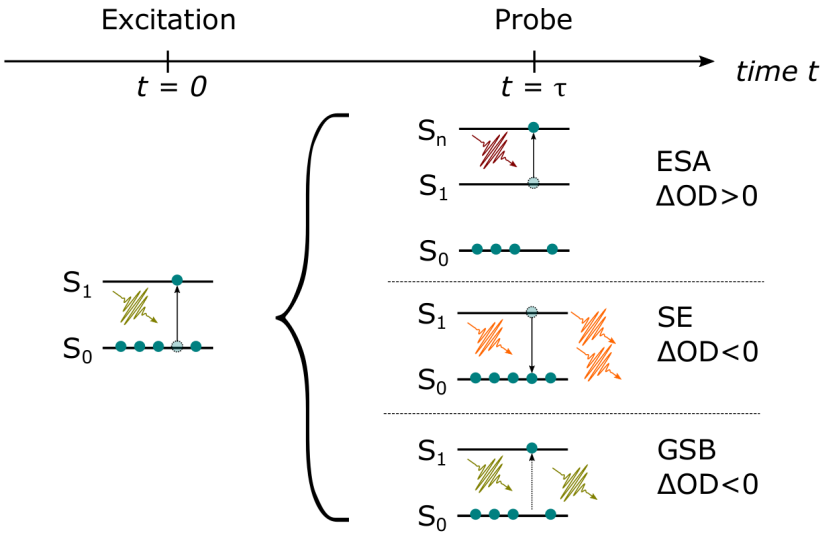

Figure 3.2: At $t = 0$, the excitation pulse promotes the molecule from the ground state (S_0) to the excited state (S_1). At $t = \tau$, the probe pulse can initial three different processes, which contribute to the TA signal. As the number of molecules in the ground state is decreased, the probe pulse is less absorbed, causing a ground state bleach (GSB). Additionally, the molecules in the excited state can be stimulated back to the ground state by the probe pulse, known as stimulated emission (SE). Alternatively, the molecules in the excited state can absorb the probe pulse to reach an even higher level (S_n), causing excited state absorption (ESA).

Such a difference in optical density normally depends on the probe wavelength λ as well as on τ.

3.2.1 Signal Contributions

The TA signal is dominated by mainly three different processes, namely ground state bleach, stimulated emission and excited state absorption (Figure 3.2).

Ground state bleach

As the excitation pulse promotes a fraction of the molecules to the excited state, the number of molecules in the ground state decreases. Consequently, the probe

pulse is less absorbed. Therefore, a negative signal, called ground state bleach (GSB), occurs in the TA signal. Its spectral shape is comparable to the one of the absorption spectrum.

Stimulated emission

The second negative signal appears due to stimulated emission (SE). Using the simplified picture of a two-level system, the probability for absorption from the ground to the excited state is equal to the probability for stimulated emission from the excited state back to the ground state, i.e. the corresponding Einstein coefficients are equal. Therefore, initially excited molecules are stimulated back to the ground state by the probe pulse. SE is limited to optically allowed transitions. Its spectral profile corresponds to the fluorescence spectrum of a molecule in the excited state. As the fluorescence is red-shifted in comparison to the absorption due to the Stokes shift, the SE is on the red wing of the GSB signal. The stimulated photons are emitted in forward direction, thus, they are detected together with the transmitted pulse.

Excited state absorption

Alternatively to the stimulated emission, molecules in the excited state can absorb photons of the probe pulse to reach even higher lying states. This process is known as excited state absorption (ESA). As it causes a reduction of the transmitted probe pulse, ESA delivers a positive contribution to the TA signal.
For all three processes, the population is assumed to be unaffected by the probe pulse, whose intensity is kept low compared to the one of the excitation pulse for this reason.

For the sake of completeness, product absorption should be mentioned as fourth possible contribution to the TA spectrum. As it does not play a role in this thesis, interested readers are referred to Ref. [87].

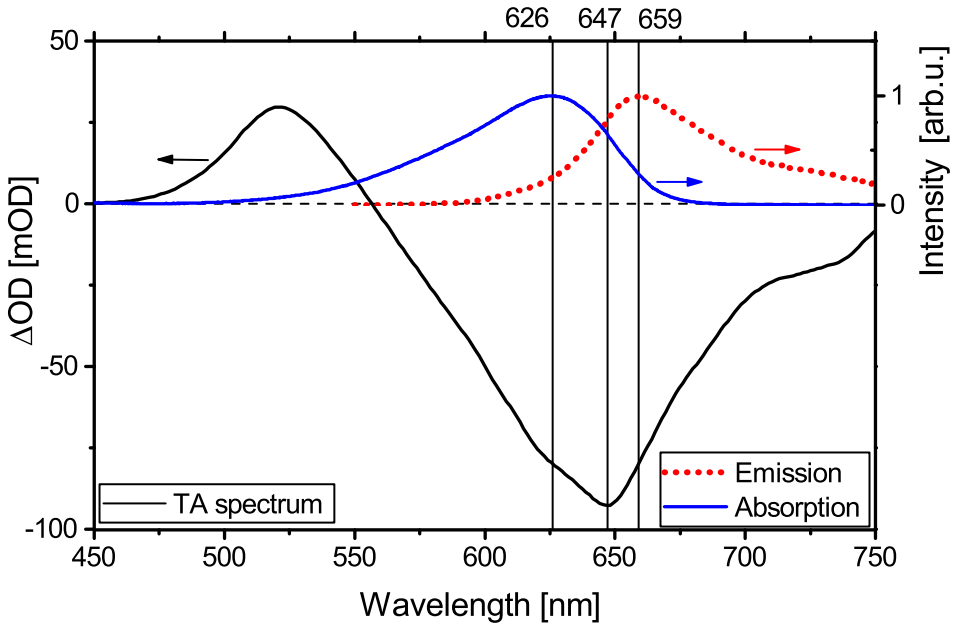

Figure 3.3: A typical TA spectrum of Nile Blue after 5 ps (black) in comparison with absorption spectrum (blue) and emission spectrum (red dashed, adapted from [88]) of Nile Blue. ESA predominantly contributes to the positive signal while GSB and SE are spectrally overlapping and sum up to the negative TA signal.

An example of an TA spectrum is shown in Figure 3.3 for Nile Blue, which acts as a sample molecule in this chapter. The ESA dominates around 520 nm. The contributions of GSB and SE overlap with a peak at 647 nm, between the maxima of absorption and fluorescence spectra. A distinction is not directly possible and can only be assumed from the absorption and fluorescence spectra.

3.2.2 Experimental Set-Up

The light source for the experiments is a Ti:sapphire amplifier laser system (Libra from Coherent) with a repetition rate of 1 kHz. The output pulses are centered at 800 nm and have a duration of 100 fs. A portion of 300 µJ per pulse is sent through a NOPA as in Chapter 2 to generate sub-15 fs pulses in the range from 540 nm to 635 nm for the experiments. This output acts as excitation pulse for the

TA measurements. A small fraction of the fundamental laser at 800 nm is focused

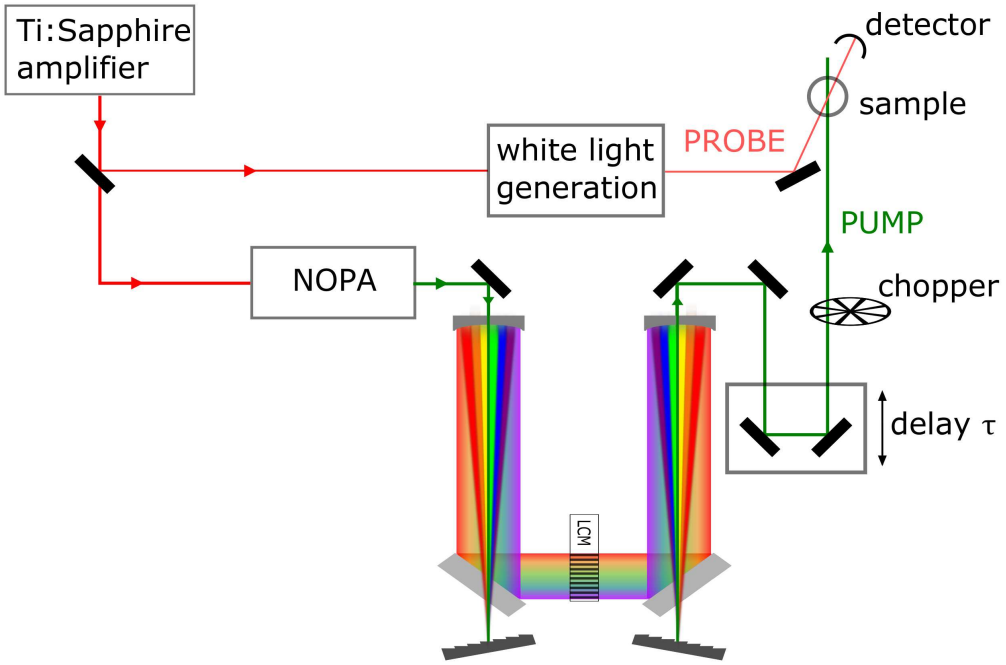

Figure 3.4: Simplified schematic of the experimental set-up, where the excitation pulse passes a shaper set-up. A small fraction of the Ti:sapphire amplifier laser system is used to generate white light continuum. It is focused into the sample and detected afterwards by a multichannel detector, which resolves the spectrum of the probe pulse. Simultaneously, a one-stage non-collinear optical parametric amplifier (NOPA) is pumped, whose output acts as the excitation pulse. After the shaper, this pulse is delayed with respect to the probe pulse and every second pulse is blocked by a rotating chopper wheel. The excitation pulse is also focused into the sample, overlapping there with the probe pulse.

into a sapphire substrate of 2 mm thickness to generate white light continuum (for details see Ref. [89] and references therein). Its spectrum ranging from about 450 to 770 nm acts as broadband probe for the TA measurements. The white light continuum is positively chirped due to processes like self-phase modulation and group velocity dispersion during its generation [90, 91].
For the realization of the temporal delay between excitation and probe, one of the pulses has to be sent through an optical delay line. The latter is a retroreflector mounted on a piezo, driven by a triangle waveform, or on a high-precision motorized computer-controlled translation stage (both from Physik Instrumente).

Typically, the excitation pulse is delayed, while the probe pulse is fixed. In the present work, the excitation pulse is delayed for transients over hundreds of picoseconds and the probe is delayed for transients, which cover less than 3 ps, for practical reasons. Before the excitation pulse reaches the sample, it passes a mechanical chopper wheel, which is a slotted rotating disk blocking every second pulse. It allows to measure the probe spectrum for a sample, which has not be disturbed by the excitation pulse. The polarization of both beams is kept parallel. They are focused into the sample to a diameter of less than 70 µm by spherical mirrors with a focal length of 20 cm, where the diameter of the probe is kept smaller than the one of the excitation beam. A uniform overlap of the two beams inside the sample volume is checked carefully.
The liquid sample is pumped by a flow system through the cell of 500 µm thickness. The excitation beam is blocked after the sample. The probe beam is collimated and sent into a prism-based spectrometer. The spectrally dispersed components are projected on a photo diode array (PDA) consisting of 256 pixels. Typically, wavelengths ranging from 450 nm to 750 nm are recorded with a spectral resolution of 0.6 nm/pixel.
A 4f set-up with a spatial light modulator is added to the set-up after the NOPA to allow the use of shaped excitation pulses. This additional pathway has to be compensated for in the pathway of the probe pulse to still ensure temporal overlap of both pulses inside the sample. For the experiments described in the following, the same shaping set-up as for the measurements in Chapter 2 with LCM 1 was utilized.

3.3 Data Acquisition and Processing

In the following, the procedure of data acquisition is described for the case that the time delay is introduced by the continuously moving piezo stage. Figure 3.5 visualizes the measurement scheme. The delay stage is driven by triangle signal from a waveform generator. Additionally, the generator delivers a square waveform, which allows one to determine the moving direction of the piezo stage. The current position of the stage is delivered by the stage controller.

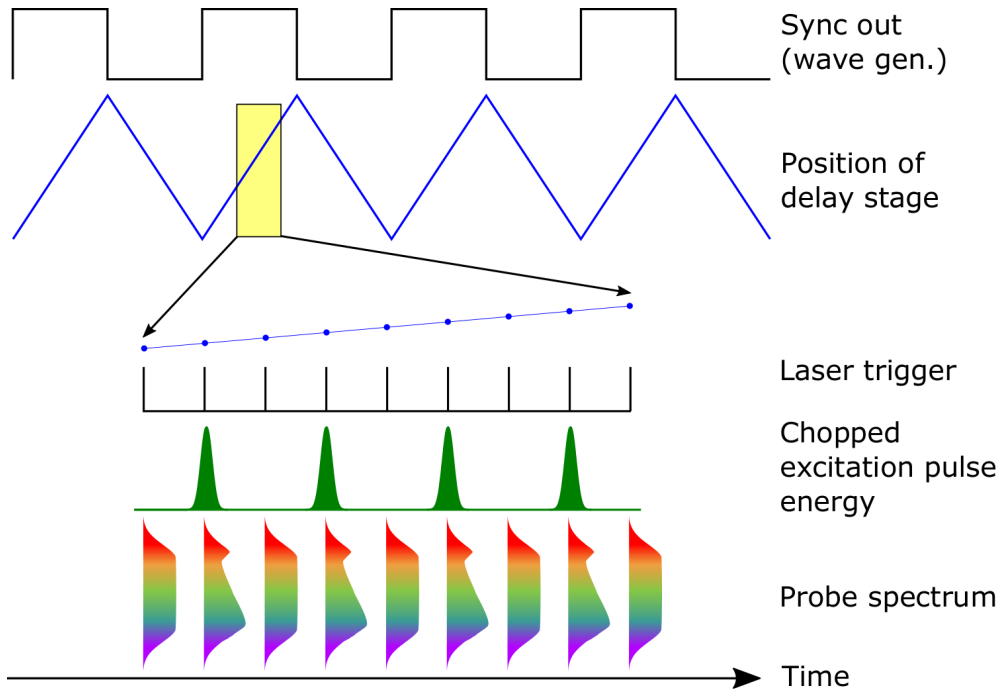

Figure 3.5: Measurement scheme using rapid-scan averaging. The piezo for the time delay is moving continuously, while its moving direction can be extracted from the signal of the wave generator (sync out). The laser triggers the acquisition of the piezo position, the energy of the excitation pulse and the probe spectrum. For every second pulse, the probe spectrum is modified as the excitation pulse interacted with the sample in advance. The difference in the absorption is determined by calculating the ratio of two adjacent probe spectra.

From the calibration of the stage, a time axis for the temporal delay between excitation and probe pulse is determined. The trigger output from the laser synchronizes the rotation of the chopper wheel to ensure that every second excitation pulse is blocked. A small fraction of the chopped excitation pulse is detected by a photodiode. Only if the excitation pulse is not blocked, light hits the photodiode. It allows one to assign for each acquired probe spectrum if the excitation hit the sample or not. Simultaneously, the probe spectrum is measured spectrally resolved behind the sample for each laser pulse. The complete data sets are saved in real time and the TA signals are calculated afterwards.

In the course of data processing, the data sequences are cut according to the

single ramps of the piezo stage and all data points close to the turning points of the piezo stage are removed. Next, the TA signal is calculated for the time delay if the excition pulse could pass the chopper, over the whole probe spectrum using Eqn. (3.2). As the probe pulse is not measured for the identical time delay due to the continuously moving delay stage, the mean of the two probe spectra before and after this specific pulse is taken as reference signal, i.e. if the excition pulse is blocked. Finally, all transients from one measurement cycle are averaged considering the time inversion due to the moving direction of the piezo stage and one data set-up of spectrally resolved transients is received.

3.4 Data Analysis

Goal of the data analysis is to extract information about the population and the vibrational coherence at specific probe wavelengths corresponding to the ground and excited state. The different steps of the data analysis are first the time-zero correction, then a polynomial fit of the transients to determine the population, followed by a Fourier analysis of the residuum. This Fourier analysis includes windowing and zero-padding for a clean Fourier transform. The height of the peaks in the Fourier spectrum quantifies the vibrational coherence in the probed state. Finally, enhancement factors are calculated to compare population and coherence for different temporal excitation pulse shapes.
In the following, the steps are explained for a single transient. Nevertheless, they are applied in parallel across the whole probe spectrum. Ground state and excited state are later assigned to different probe wavelengths according to the shape of the TA spectrum.

3.4.1 Time-Zero Correction

Around $\tau = 0$, the nonlinear interaction of excitation and probe pulse occurs as coherent artifact. As mentioned previously, the broadband probe pulse is

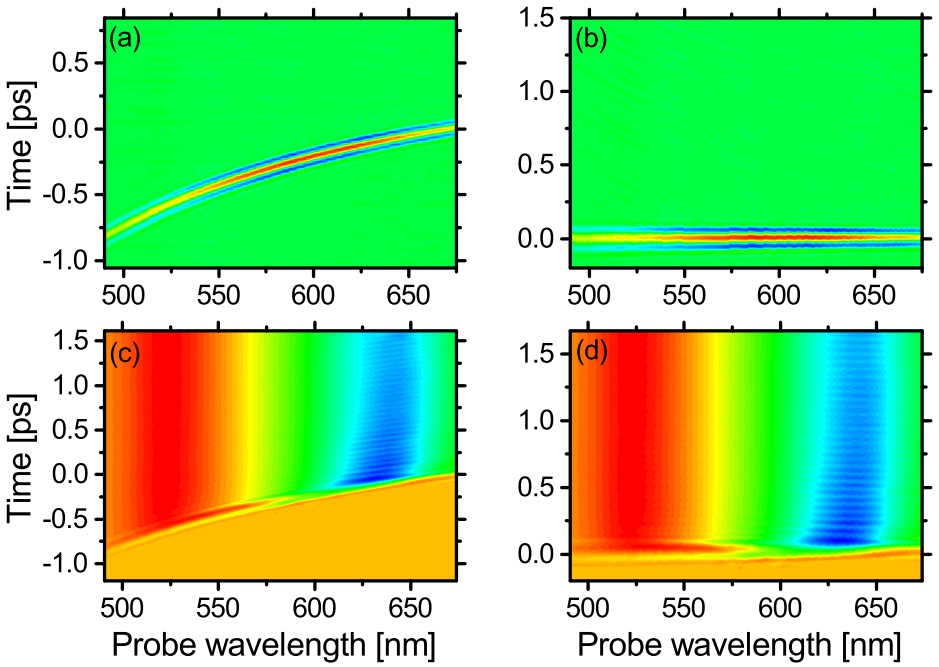

Figure 3.6: 2D TA data from the pure solvent (a) and from dissolved sample (c). The time for maximum signal for each probe wavelength is determined from the pure solvent data (a) and plotted with a polynomial of order four. The solvent data and also the data with sample (c) are corrected by this function, resulting in (b) for the solvent data and (d) for the data with sample. Consequently, the data for all probe wavelengths share the same zero-point, which is crucial for further data processing.

positively chirped. Thus, the different components of the probe spectrum interact at different times with the excitation pulse in the sample. This causes a time-dependent coherent artifact and makes a dispersion correction necessary to ensure that the whole probe spectrum shares the same zero point ($\tau = 0$) for the later analysis. This time-zero function can be determined from pure solvent data [89]. The time with maximum signal is identified for every transient from the solvent data. These points in time are plotted versus probe wavelength and they are fitted with a polynomial of order four, providing the time-zero function. For the dispersion correction of the data with sample, the time axis of each transient is shifted by the corresponding value of the time-zero function (c.f. Figure 3.6). The shape of the coherent artifact depends on the temporal shape of both involved pulses as shown for transform-limited and multipulse excitation in Figure 3.7

for two different excitation and probe wavelengths. However, the solvent data are only recorded for TL excitation and used to correct for the coherent artifact of all temporal excitation shapes as the polynomial fit is independent of such temporal shapes.

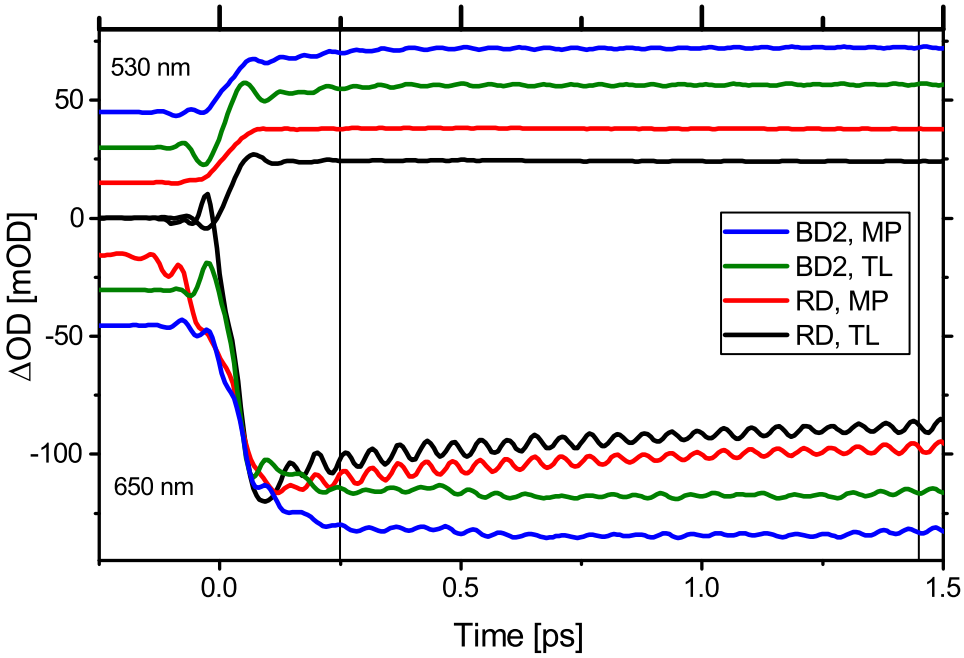

Figure 3.7: Transients of Nile Blue probed at 530 and 650 nm after excitation with a transform-limited (TL) pulse and a multipulse (MP) and a red-detuned (RD) and a far blue-detuned (FBD) excitation spectrum. (These excitation spectra are depicted in Figure 3.13.) The shape of the coherent artifact around $\tau = 0$ as well as the strength of the oscillatory contribution to the transient depends on the excitation wavelength and its temporal shape. The end of the shaping window, which is excluded from the data analysis, is set to 0.25 ps. The Fourier analysis is applied to data over 1.2 ps between 0.25 and 1.45 ps. The curves are plotted with horizontal offset for more clarity and easier comparison.

3.4.2 Shaping Window

The coherent artifact is spread over a few hundreds of femtoseconds in the case of a multipulse excitation and in addition intra-multipulse interferences occur,

which lead to further distortions of the signal [92]. This part of the data, also called shaping-window, has to be excluded from the further analysis to ensure a correct quantification of the vibrational coherence. The end of the shaping window is set to 0.25 ps (see Figure 3.7) for the analysis of the data.
As the shaping window is excluded from the data analysis, the time-zero correction described before is sufficient and no further subtraction of the coherent artifact [93] is necessary.

3.4.3 Polynomial Fitting

Before the data can be correctly fitted, they have to be corrected for scattering of the excitation pulse. As the spectra of excitation and probe overlap, part of this scattered light is detected together with the probe light causing a distortion of the spectrally resolved TA signal. Although the experimental set-up, especially the flow cell window, is optimized to minimize scattering, the latter cannot be completely suppressed and has to be taken into account for the analysis. The scattering contributes to the transient absorption signal in the spectral range of the excitation as a positive offset as it is only detected if the excitation pulse is not blocked by the chopper. The offset is independent of the time delay between excitation and probe pulse. Thus, it even appears if the excitation is delayed with respect to the probe, i.e. $\tau < 0$, when no TA signal exists. As a consequence, affected transients can be easily corrected by subtracting the offset measured for $\tau < 0$. This correction is crucial for the analysis of the data as the signal height, which could be distorted by such an offset, is used as a measure for the population later.
After this correction, every transient is fitted with a polynomial of order four within a time span of 1.2 ps starting after the shaping window (green curve in Figure 3.8). The mean of this fit over the last 90 fs is finally used as a measure of the population.

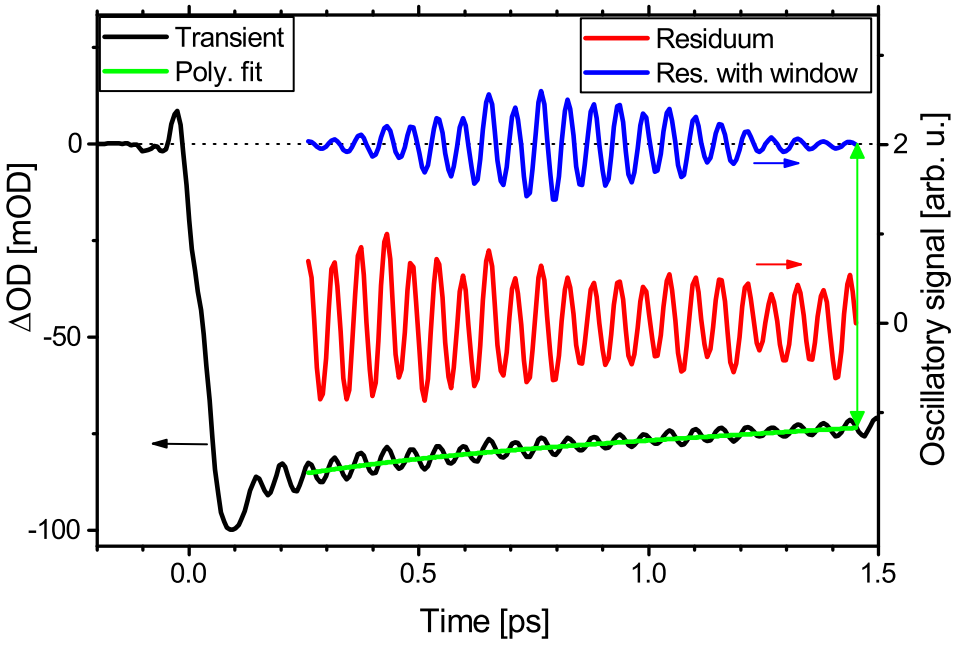

Figure 3.8: Transient (black) of Nile Blue probed at 650 nm after excitation with a TL pulse. In the time window from 0.25 to 1.45 ps the transient is fitted with a polynomial of order four (green). The residuum (red) is multiplied with a Gaussian window (result in blue) before zero-padding and FT are applied. This procedure is done for all wavelengths across the probe spectrum. The vertical green arrow indicates that the fitted TA signal at 1.45 ps is taken as measure for the population.

3.4.4 Fourier Analysis

The vibrational coherence of specific modes within the molecule is proportional to the oscillatory component in the TA signal. For its quantification, the oscillatory signal is analyzed via Fourier transformation (FT). As described previously, the oscillatory signal is determined by subtracting a polynomial fit from the transient. The resultant residuum (red curve in Figure 3.8) is normalized by the corresponding value for the population and it typically consists of about 200 data points.

The time span of 1.2 ps is a compromise for the FT between spectral resolution and quantifying the decaying oscillations, i.e. longer time span reduces the FT

signal further including a higher level of noise. To exclude artifacts occuring from rash FT, two more steps of processing, namely windowing and zero-padding, are necessary before FT is applied.

Windowing

The time span for the FT is in spectroscopy usually chosen independent of the periods causing the oscillatory contributions of the TA signal. Therefore, the time span is normally not a multiple of (all) these periods. As a consequence, a smoothing at the beginning and end of the data sets is required to exclude artificial frequencies in the FT spectrum (c.f. blue curve in Figure 3.9(a)).

Windowing [94] is applied for this reason by multiplying the transient with a Gaussian window function. Thus, the decay of the residuum to nearly zero at the edges is achieved (dark blue curve in Figure 3.8) and only true frequency components appear in the FT spectrum (c.f. black curve in Figure 3.9(a)).

Zero-Padding

The spectral resolution in the FT spectrum is limited by the maximum time window, which is Fourier transformed. For a time span of $\Delta t = 1.2$ ps the spectral resolution (in wavenumbers) is given by

$$\begin{aligned} \Delta\tilde{\nu} &= \frac{1}{c\Delta t} \\ &= 27.8\ \mathrm{cm}^{-1}, \end{aligned} \tag{3.3}$$

where c is the speed of light. The limit for resolvable wavenumbers in the FT spectrum cannot be circumvented. However, it is possible to increase the sampling to determine frequencies in the spectrum more precise by the use of so-called zero-padding, where the number of points per data set is increased by adding a certain amount of zeros [94].
The effects of zero-padding are demonstrated for two data sets shown in Figure

3.9(b). The data points of the FT spectrum without zero-padding are spaced by 27.8 cm^{-1}. With zero-padding the number of points is increased from 189 to 8192 ($= 2^{13}$). In this case, the sampling of the resultant FT spectrum is 0.64 cm^{-1}, allowing for a smooth curve. The two curves for a transform-limited excitation in the graph shows that the position of the maximum peak is shifted by 10 cm^{-1} due to zero-padding, although both curves are based on the same data set. Furthermore, the amplitude of a peak can be misleading as a second data set shows. The amplitudes of the peaks are different without and with zero-padding, especially comparing the amplitudes for multipulse and transform-limited excitation gives different results with and without zero-padding. This second effect is even more significant for the study presented as the amplitudes of the peaks are used as a measure for vibrational coherence and the ratio between these values for different data sets are determined to quantify the effects of different temporal shapes of the excitation pulse.

3.4.5 Enhancement Factors

The final step of the data analysis is the determination of the enhancement factors of population , ε_{Pop}, and vibrational coherence, ε_{coh}, due to the various temporal excitation pulse shapes. The factors are calculated as ratio between the population (coherence) of the shaped pulse, $p(\phi'', MP)$ ($A_{FT}(\phi'', MP)$), and, as a reference, the population (coherence) of a TL pulse, $p(TL)$ ($A_{FT}(TL)$). Expressed as formulas the enhancement factors are for the population

$$\varepsilon_{Pop} = \frac{p(\phi'', MP)}{p(TL)} \tag{3.4}$$

and for the coherence

$$\varepsilon_{coh} = \frac{A_{FT}(\phi'', MP)}{A_{FT}(TL)}. \tag{3.5}$$

The procedure of determining the enhancement factor is visualized in Figure 3.10, where the population is measured for TL, negatively and positively chirped ($\pm 50 fs^2$) excitation (Figure 3.10 (a)). The value for TL is taken as a reference to

determine the enhancement due to chirp (Figure 3.10 (b)). The same procedure is repeated for different excitation shapes.
It is important to notice that in the case of negative TA signal, the enhancement factor for the population has to be inverted as a less negative signal corresponds to more population in the ground state. This can be easily understood by looking at a single transient within the bleach region (e.g. data at 650 nm probe in Figure 3.7). For longer delays the absolute value of the signal decreases as the population in the ground state increases. Thus, the ratio of the signal between long and short delay is smaller than one.
The enhancement factors shown in this chapter are obtained by the data analysis as described here.

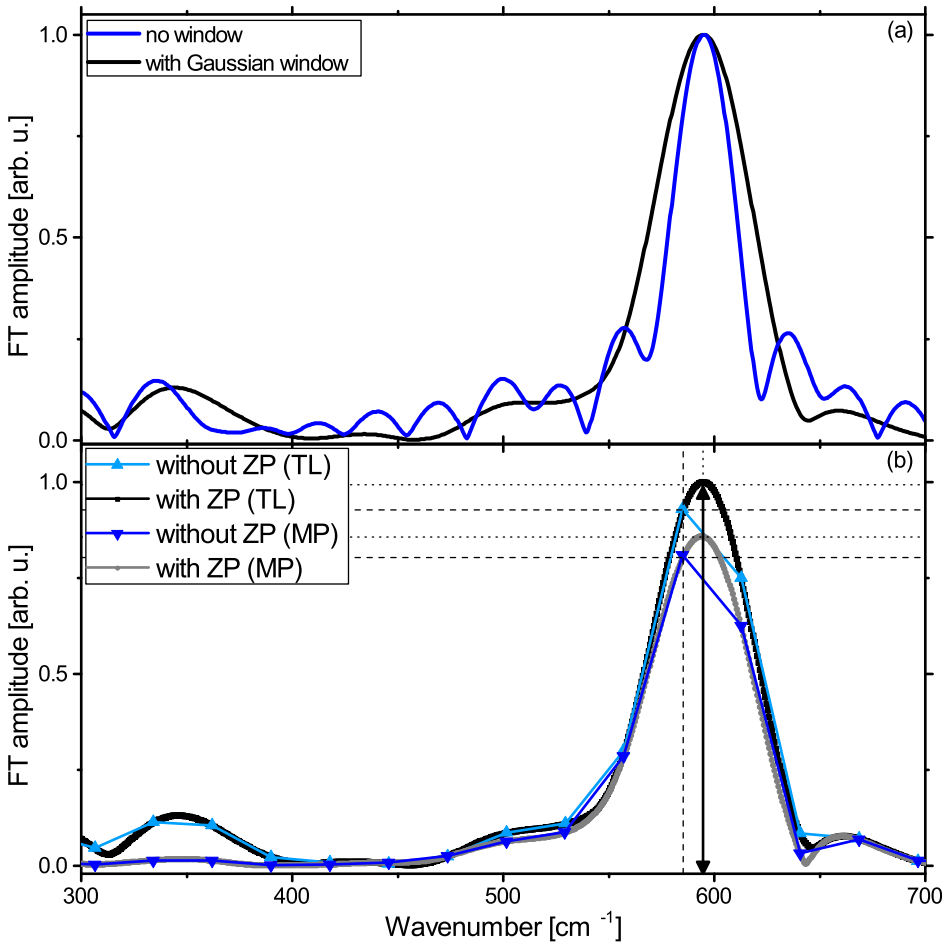

Figure 3.9: (a) FT spectra with pure data (blue) and after windowing with a Gaussian function (black). As there is no periodicity of the signal at the edges of the FT window, an instantaneous jump of the signal appears, which causes side loops as seen here (blue). The application of a window function across the FT window smooths the edges efficiently (black). However, the width of the main peak increases at the same time.
(b) Visualization of the effect of zero-padding (ZP) of a transient probed at 650 nm after excitation with a transform-limited (TL) pulse and multipulse (MP). The sampling is increased by zero-padding to ensure a correct determination of the peaks as only with zero-padding the correct central wavenumber and amplitude of the peaks can be determined. The height of the maximum with zero-padding is used as a measure for the vibrational coherence. The lines are a guide to the eye about the discrepancy between the analyses with and without zero-padding. The arrow (only for TL excitation) indicates that the FT amplitude is taken as a measure for the vibrational coherence.

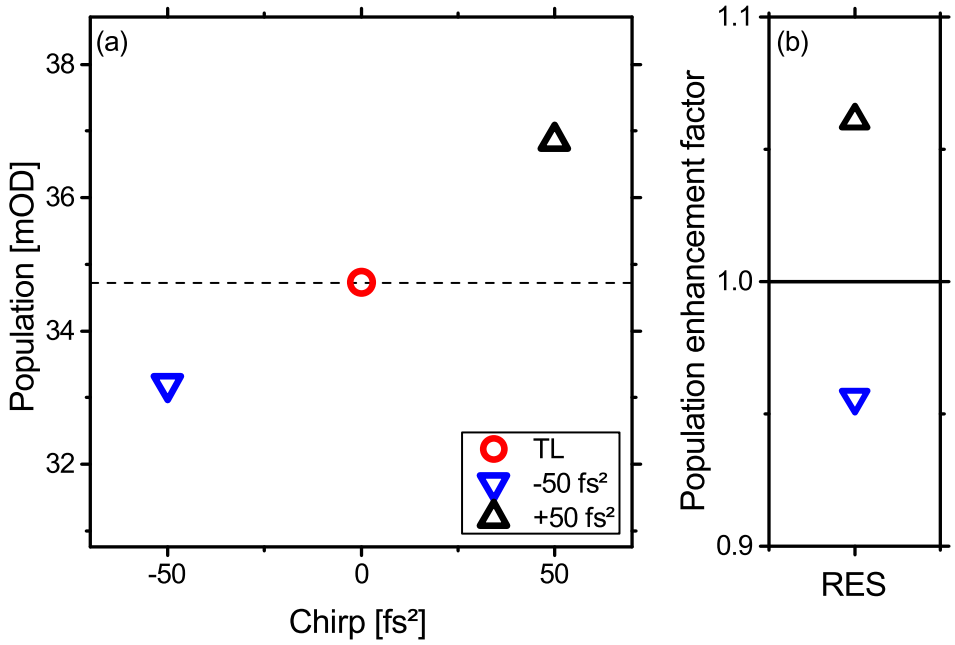

Figure 3.10: (a) The population is plotted versus the applied chirp to the excitation pulse. The value for TL excitation (red circle) is taken as a reference to calcuate the enhancement factor ε_{Pop} according to Eqn. (3.4) due to positively (upwards pointing black triangle) and negatively (downwards pointing blue triangle) chirped excitation. (b) As a result, the various enhancement factors ε_{Pop} are plotted versus the excitation spectrum. (Here for the resonant spectrum, which is shown in Section 3.13.)

3.5 Experimental Details

The principle of femtosecond pulse shaping was explained in Section 2.2.1. Beside the shaping to linearly chirped pulses and multipulses, chirped multipulses are applied in the systematic study. As a further parameter the excitation spectrum is tuned across the absorption spectrum of the prototype molecule, Nile Blue. These three aspects are described in the following.

3.5.1 Chirped Multipulses

The two phase modulations, chirp and multipulse, can also be combined. In the scope of this thesis, the combination is realized by directly summing up the two phase terms given in Eqn. (2.2) (for $b_2 \neq 0$) and Eqn. (2.4). In the case of a multipulse, each subpulse is a replica of the original pulse, with the possibility of exhibiting offsets in the phase yet maintaining the same pulse envelope. In analogy, a chirped multipulse consists of a sequence of identically chirped subpulses. In an illustrative picture this can be understood as the transform-limited pulse is first chirped and then, in a second step, the multipulse, which maintains according to (2.8) the temporal character of the original pulse, is generated.

Examples for the spectral phases of chirped pulses, multipulses and chirped multipulses are shown in Figure 3.11. The effect of various linear chirp values on the multipulse is shown in Figure 3.12[1]. Each of the subpulses is chirped independently from each other by adding the phases for linear chirp and multipulses (Figure 3.12(d)-(e)). However, for increasing values of the linear chirp, spectral contributions of adjacent subpulses overlap (Figure 3.12(e)-(f)) leading to interferences between the subpulses (Figure 3.12(b)), which can even cause a modulation of the interpulse distance (Figure 3.12(c)). To avoid such kind of distortions as well as for systematic reasons the chirp value is kept constant while the sign is modified, $\phi'' = \pm 50\,\mathrm{fs}^2$.

[1] The corresponding representation of transform-limited, linearly chirped and multipulse is shown in Figure 2.1

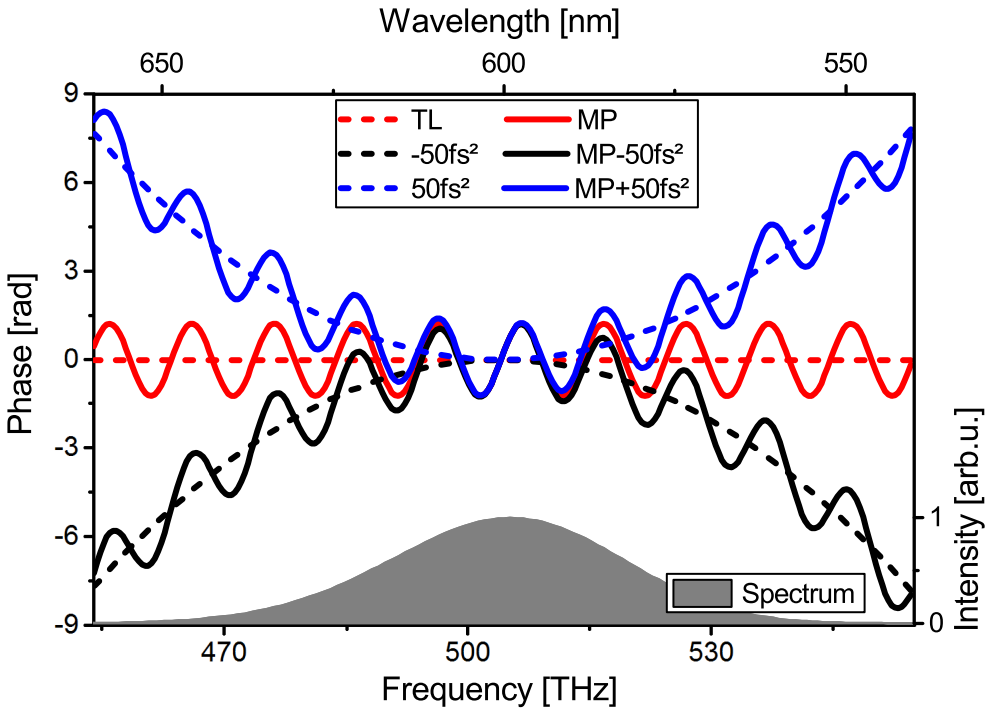

Figure 3.11: The spectral phases for chirped pulses ($\pm 50 fs^2$), multipulses ($a = 1.23$, $b = 56\,fs$, $c = 0$) and chirped multipulses as the sum of the previous phases. They can be applied for example to a Gaussian spectrum centered at 600 nm. The corresponding temporal distributions are shown in

The variation of the temporal shape of the excitation pulse is realized by the LCM, which was already utilized for the study in Chapter 2. The interpulse distance of the multipulse is in the scope of this study set to 56 fs matching the ring-breathing mode of Nile Blue.

The correct performance of the LCM is checked in advance to ensure reliable measurements. The quadratic dependence of the energy across the spectrum as a function of the amplitude applied to the LCM verifies correct amplitude shaping (not shown). Second-harmonic autocorrelation traces of chirped pulses and multipulses, i.e. pure phase modulation, show the correct parameters of pulse duration (c.f. Eqn. (2.3)), interpulse distance and relative height. Comparing the spectra of these differently shaped pulses shows that the spectral shape is

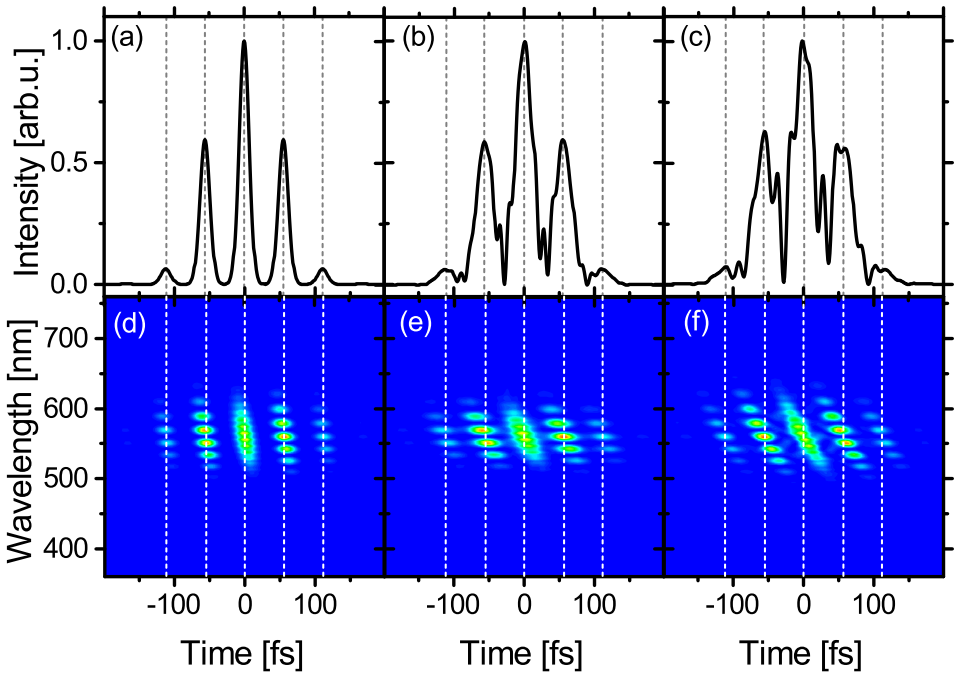

Figure 3.12: Simulated temporal distributions and 2D representations (wavelength versus time) for chirped multipulses with linear chirp of $\phi'' = 50\,\mathrm{fs}^2$ (a, d), $\phi'' = 100\,\mathrm{fs}^2$ (b, e) and $\phi'' = 140\,\mathrm{fs}^2$ (c, f). Such a 2D representation clearly visualizes that all subpulses of a chirped multipulse have the same linear chirp when the spectral phases of linear chirp and multipulse are added up. Increasing the linear chirp leads to interferences between the subpulses of the chirped multipulse as the temporal distribution shows (b, c), which can cause a modification of the interpulse distance (c). The corresponding 2D representations (e, f) show that spectral components of different subpulses overlap in time.

unaffected by pure phase modulation. Thus, correct and independent phase and amplitude modulation are sufficiently verified. Additionally, the beam profile of the shaped pulses at the position of the sample is checked to exclude space-time coupling [95].

3.5.2 Excitation Pulse

For this study the output of the NOPA acts as an excitation pulse. It is tuned to four spectra with central wavelengths between 560 and 635 nm across the absorption spectrum of Nile Blue as shown in Figure 3.13 and listed in Table 3.1. The pulse durations are kept around 12 fs. Two of the spectra (labeled as

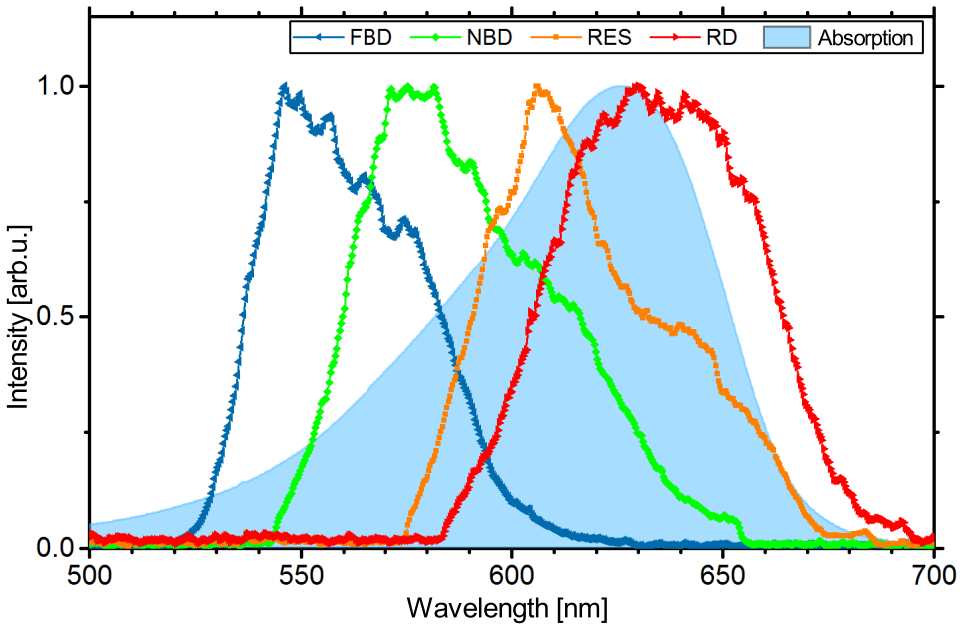

Figure 3.13: Absorption spectrum of Nile Blue in methanol (bright blue shaded) and the four different excitation spectra. Two of the spectra (labeled as FBD (blue), NBD (green) are blue-detuned with respect to the maximum of the absorption spectrum. They are overlapping with different parts of the blue edge of the absorption spectrum. The third spectrum (RES (orange)) is resonant with the main peak of the absorption spectrum and the last one (RD (red)) is slightly red-detuned, covering the red edge of the absorption spectrum.

NBD as FBD) are far and near blue-detuned with respect to the maximum of the absorption spectrum. They overlap with different parts of the blue edge of the absorption spectrum. The third spectrum (RES) is resonant with the main peak of the absorption spectrum and the last one (RD) is slightly red-detuned, covering the red edge of the absorption spectrum. The energy per excitation

Abbreviation	FBD	NBD	RES	RD
Central wavelength λ_{cen} [nm]	562	590	620	635

Table 3.1: Abbreviations and central wavelengths of the four excitation spectra.

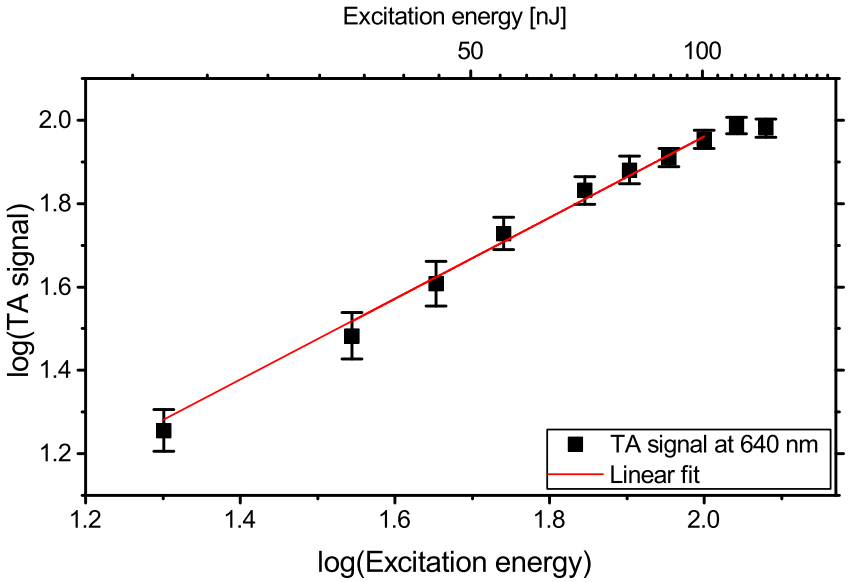

Figure 3.14: Dependence of the TA signal on the energy of the excitation pulse in a log-log scale for a far blue-detuned spectrum. The one-photon regime of the measurements is ensured as the slope is 0.96 ± 0.05.

pulse is varied from 25 nJ to 80 nJ depending on the spectral overlap between excitation and absorption spectrum to get a clean oscillatory signal over the whole probe spectrum. At the same time, it is ensured that the measurements are performed in the one-photon regime. For this reason, the dependence of the TA signal on the energy of the excitation pulse is examined for all excitation spectra. The energy and the TA signal are plotted in a log-log scale for a far blue-detuned spectrum in Figure 3.14. A linear fit of the data points for pulse energies smaller than 100 nJ has a slope of 0.96 ± 0.05, which indicates a linear dependence.
The energy per pulse iss carefully monitored for each measurement. For minor effects on the overall energy ($< 2\%$), the data sets are corrected by normalizing the data sets to the same pulse energy for each excitation spectrum to ensure microscopic effects and to exclude ensemble effects. For a sufficient signal-to-

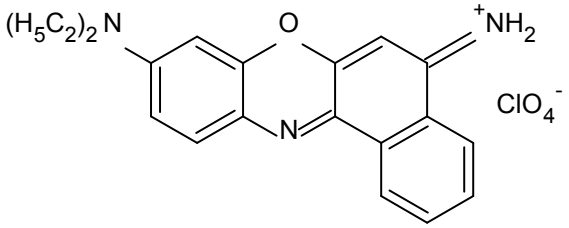

Figure 3.15: Chemical structure of the laser dye Nile Blue with the chemical formula $C_{20}H_{20}N_3O_5Cl$. The four six-membered rings are characteristic for Nile Blue and cause the dominant low-frequency mode at around 600 cm^{-1} (corresponding to a period of 56 fs) of the molecule.

Property	Value	Unit
Chemical formula	$C_{20}H_{20}N_3O_5Cl$	
Molar weight	417.85	g mol^{-1}
Molar absorption coefficient [96]	7.68×10^4	L mol^{-1} cm^{-1}
Absorption peak wavelength [96]	626.75	nm

Table 3.2: Chemical and optical properties of Nile Blue, which are relevant for the experiments. The values for molar absorption coefficient and absorption peak wavelength are given for Nile Blue dissolved in methanol.

noise ratio, 80 transients are acquired using the rapid-scan approach. Such a measurement is repeated up to ten times and averaged to receive one data set.

3.5.3 Nile Blue

The chemical structure of Nile Blue (5-Amino-9-diethyliminobenzo[a]phenoxazonium Perchlorate, $C_{20}H_{20}N_3O_5Cl$) is shown in Figure 3.15 and the properties, which are relevant for this study are given in Table 3.2.
As a laser dye, Nile Blue belongs to the family of oxazines. Their molecular structure has six-membered carbon rings in common, where one oxygen and one nitrogen atom are placed in one of the central, unsaturated six-membered ring. The Raman spectrum of Nile Blue dissolved in methanol is measured for a non-resonant excitation at 785 nm and shown in Figure 3.16. The Raman spectrum of Nile Blue shows a dominating mode to be at 592.1 cm^{-1} (corresponding to

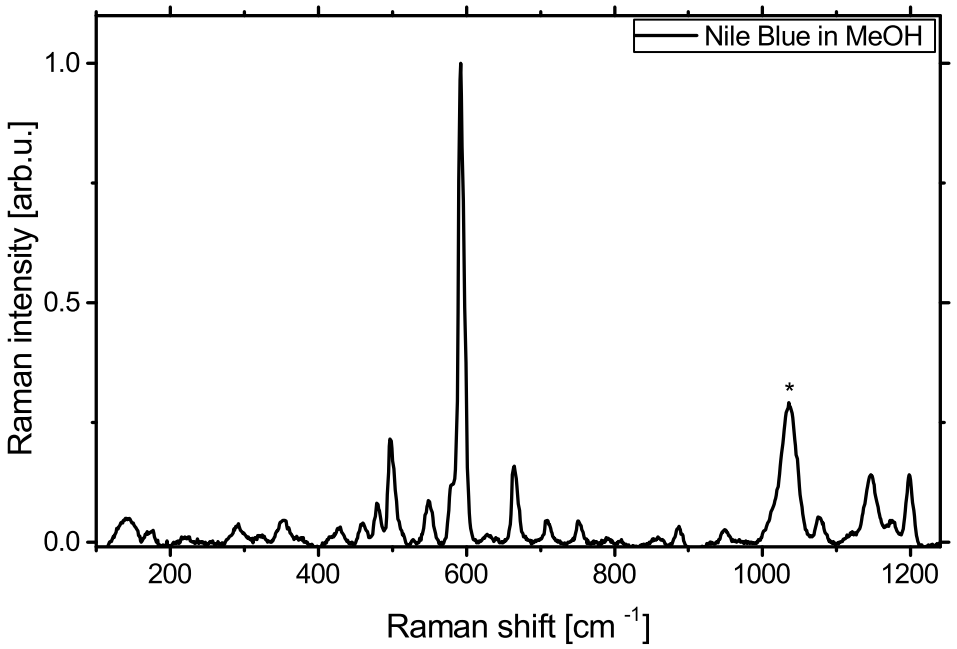

Figure 3.16: The non-resonant Raman spectrum of Nile Blue dissolved in methanol from a red-detuned excitation at 785 nm. The most dominant mode is at 592.1 cm^{-1}. Further low-frequency modes are located at 290.0, 354.8, 479.2, 497.0, 548.9 and 664.7 cm^{-1}. The peak at 1035 cm^{-1} (marked by asterisk) in the Raman spectrum is due to the C-O stretch in methanol.

a period of 56 fs). This mode is characteristic for oxazines and it is assigned to correspond to a ring breathing mode. The excited state of Nile Blue dissolved in methanol has a lifetime 1.3 ns, which was determined from fluorescence measurements [97]. Such a long lifetime indicates that the excited state predominated decays back to the ground state and no further intermediate states are involved. This is favorable for the study here as it allows the assumption to examine a molecular system of two relevant states. Furthermore, the low-frequency ring-breathing mode decays within a few picoseconds [81, 85, 98], which provides the possibility to study the mode over hundreds of oscillations with high accuracy. Apart from utilization of Nile Blue for such femtosecond studies, it is frequently utilized in spectroscopic research fields. Fundamental research into its molecular properties such as excited state structure and dynamics [99, 100], the intermolecular photoinduced proton transfer [101] and more recently, its excited state electric dipole moment [102] have been conducted. In more applied research avenues,

Nile Blue has often acted as prototype for various experimental techniques and analyses such as fluorescence-line-narrowing spectroscopy in glasses and polymers at 5 K [103] and two-dimensional analysis of integrated three-pulse echo signals [104]. For the sake of completeness, it should be mentioned that its favorable optical properties, especially its fluorescence, gave it many applications as a fluorescent label in biological and medical research (e.g. Ref. [105]).

For the TA measurements, solutions of Nile Blue (Radiant Laser Dyes) were made by dissolving the solid in methanol solvent (Sigma Aldrich, purity 99.8 %). The optical density was set to be 0.65 OD in the 500 µm flow cell at the absorption maximum. The steady state absorption was checked before and after each measurement series to exclude any degradation of the sample.

3.6 Results

3.6.1 General Results from Transient Absorption Data

In Figure 3.17, transient absorption spectra for various time delays between excitation and probe pulse are shown. There are two dominant features with opposite sign, which both diminish over time. In the region of positive signal (< 555 nm), excited state absorption (ESA) dominates with a peak at 525 nm. The negative signal (> 555 nm) in contrast represents an overlap of ground state bleach (GSB) and stimulated emission (SE). The peak signal appears at 647 nm, which is far away from the absorption maximum at 626 nm as the stimulated emission is red-detuned to the ground state absorption spectrum.
In the following, only data within the first 2 ps are taken into account as the oscillatory signal is used as a measure of the initiated vibrational coherence. Concentrating on a short span of time delays brings an advantage from an experimental perspective. The time delay can be introduced by a continuously moving piezo stage, which is limited to a maximum time delay of 3 ps in total, and thereby setting the experiment to a rapid-scan configuration. The advantages of this have already been shown in Chapter 2, especially with short acquisition

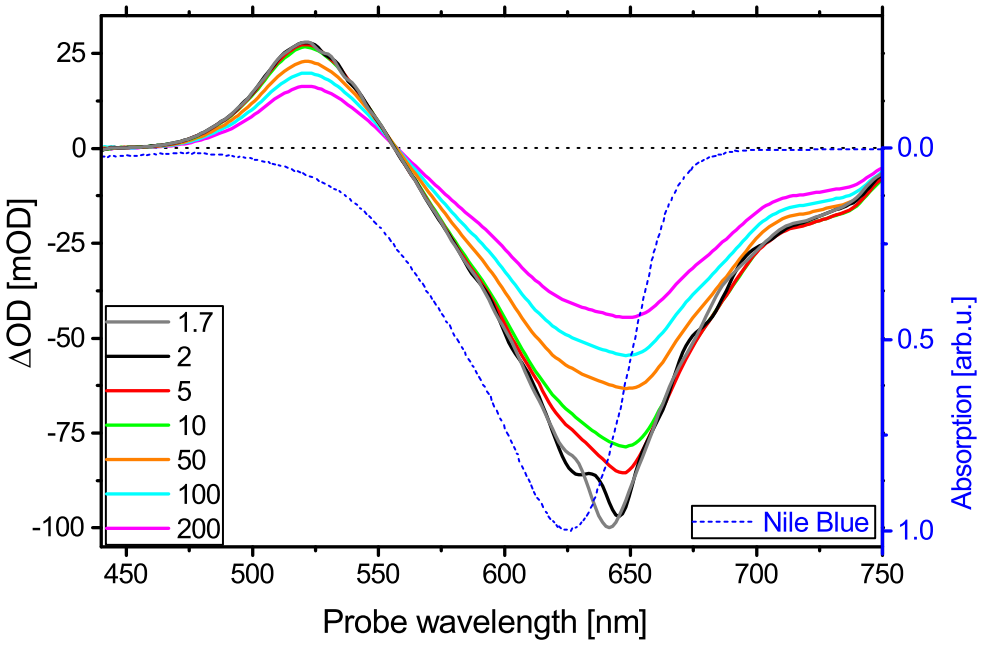

Figure 3.17: Transient absorption spectra from 450 nm to 750 nm for various temporal delays between excitation and probe pulse between 1.7 ps and 200 ps (given in the legend) for transform-limited near blue-detuned excitation with in comparison with the absorption spectrum of Nile Blue. In the region of positive signal (< 555 nm), ESA dominates with a peak at 525 nm. The negative signal (> 555 nm) in contrast represents an overlap of GSB and SE. The peak signal appears at 647 nm, which is far away from the absorption maximum at 626 nm. The data sets for 1.7 ps and 2 ps are overlapped by the oscillatory contribution of the vibrational coherence. They are roughly out-of-phase as the period of the oscillations is 56 fs. The oscillations are absent for 5 ps and longer.

times, which can be more easily realized for a short span of time delays and rapid-scan averaging.

A complete TA data set over 1.5 ps is shown in Figure 3.18 with the same dominant features previously seen. The oscillations can be clearly seen in the negative GSB region around the peak minimum (Figure 3.18, between 625 nm and 650 nm). To visualize the existence of the oscillations in the signal independent of the absolute height, the second derivative of the single transients across the spectrum is calculated and plotted in Figure 3.19. The sign distinguishes between the vicinity of a local maximum (negative second derivative, black in the figure) and the

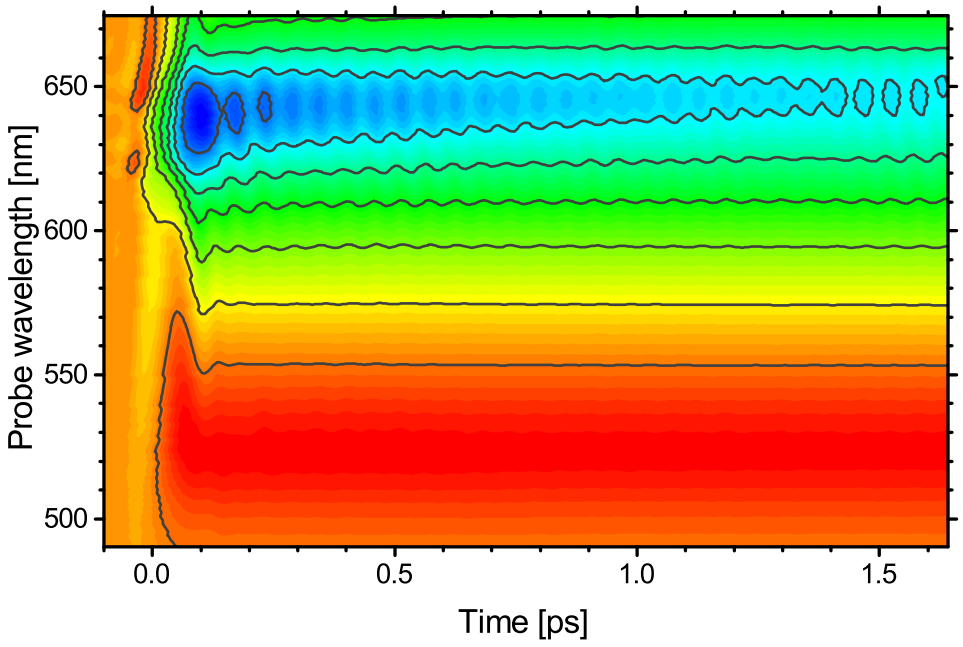

Figure 3.18: Transient absorption signal of Nile Blue as a function of time delay and probe wavelength after a resonant TL excitation. At time 0 ps an immediate change of the signal appears: For probe wavelengths smaller than 555 nm the signal is positive (red colors), for larger wavelengths it is negative (blue colors). The absolute amplitude at the minimum (around 647 nm) is about three times larger than at the maximum (around 530 nm). Across the whole TA signal a modulation of the signal with a period of 56 fs appears, which is visualized in Figure 3.19.

vicinity of a local minimum (positive, white). Advantages of this representation are that: first, small-amplitude oscillations are visible, as the sign is independent of the slow decay of the oscillations, and second, minimal data processing is necessary as slow kinetics do not have to be subtracted in advance. The vibrational coherence appears across the whole probe spectrum with one dominating mode of 56 fs. It is even visible around 555 nm, where the TA signal and the amplitude of the oscillations are close to zero. Nevertheless, it does not provide any information about the signal amplitude. Therefore, Fourier transform (FT) is applied in the following to quantify the amplitude of the oscillatory signal as a measure of the vibrational coherence of the system.

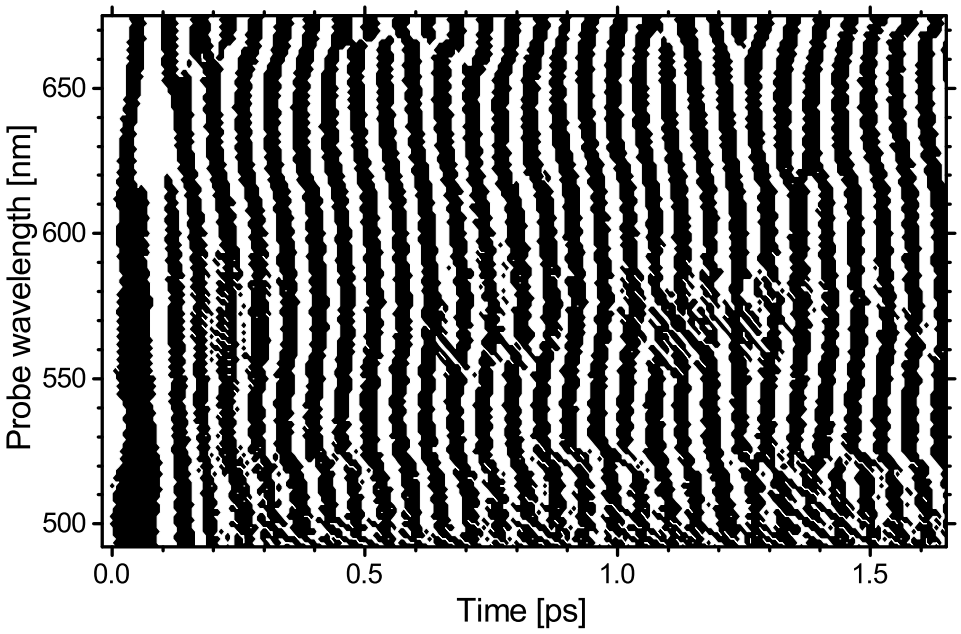

Figure 3.19: Sign of second derivative of the TA signal as a function of delay time and probe wavelength after the resonant TL excitation to visualize the vibrational coherence independent of the TA signal strength. White (black) corresponds to positive (negative) second derivative, occuring in delay ranges of concave upward (downward) TA signal. This method was inspired by Ref. [106]. The vibrational coherence appears across the whole probe spectrum with one dominating mode of 56 fs. It is even visible around 555 nm, where the TA signal and the amplitude of the oscillations are close to zero. Furthermore, this representation implies phase shifts appearing slowly around 625 nm and more abrupt around 520 nm, which are addressed in more detail in Section 3.6.2.

3.6.2 Vibrational Coherence

The Fourier analysis (described in Section 3.4.4) of the TA data provides the contributions of various molecular modes. The vibrational coherence of the ring-breathing mode in particular is quantified by the FT amplitude of the peak around 600 cm^{-1} as described in Section 3.4.4. In the following, the effect of parameters like the bandwidth as well as the spectral and temporal shape of the excitation pulse on the molecular modes and especially the ring-breathing mode are examined as these are possible parameters to control the vibrational

coherence. The FT provides not only the strength of the oscillation, i.e. the FT amplitude, but also the phase of the oscillation. The phase profiles in dependence on the probe wavelength allows for extracting information about the wave packet dynamics in the ground and excited state. Such dynamics are influenced by the temporal and spectral shape of the excitation pulse.

Effect of Different Temporal Excitation Shapes

The temporal shape of the excitation pulse is the central knob for performing coherent control experiments. For this reason, the effect of different temporal shapes of the excitation on the vibrational coherence are compared in the following. This comparison does not only take the ring-breathing mode into consideration, but also other low-frequency modes. The temporal shaping especially with multipulses allows for differently addressing modes. This can be crucial for the success of control experiments, which can be influenced by the coupling between various modes.
For various temporal shapes, the FT amplitude spectra at the probe wavelength of 610 nm are shown for a resonant excitation pulse in Figure 3.20. The FT spectrum for a TL excitation is dominated by the mode near 600 cm^{-1}. Additionally, modes around 50 and 300 cm^{-1} are visible. The overall shape for chirped excitation (50 fs^2) is similar, but the maximum amplitude is reduced. Using a multipulse with $b = 56$ fs instead, the maximum amplitude increases and the modes around 300 cm^{-1} disappear. The combination of multipulse and positive chirp, slightly decreases the height of the maximum while the multipulse character of the excitation still leads to the suppresion of the modes around 300 cm^{-1}. For comparison a multipulse, which is out of phase with respect to the ring-breathing mode, is used as temporal shaping of the excitation pulse. It is realized by increasing the interpulse distance by a factor of 1.5 from $b = 56$ fs to $b = 84$ fs. Using such a temporal shape causes a complete cancellation of the mode around 590 cm^{-1}. Also the mode around 300 cm^{-1} is attenuated in comparison to a transform-limited excitation. The mode around 350 cm^{-1} in contrast is still present although it is not perfectly in phase with a multipulse with $b = 84$ fs.

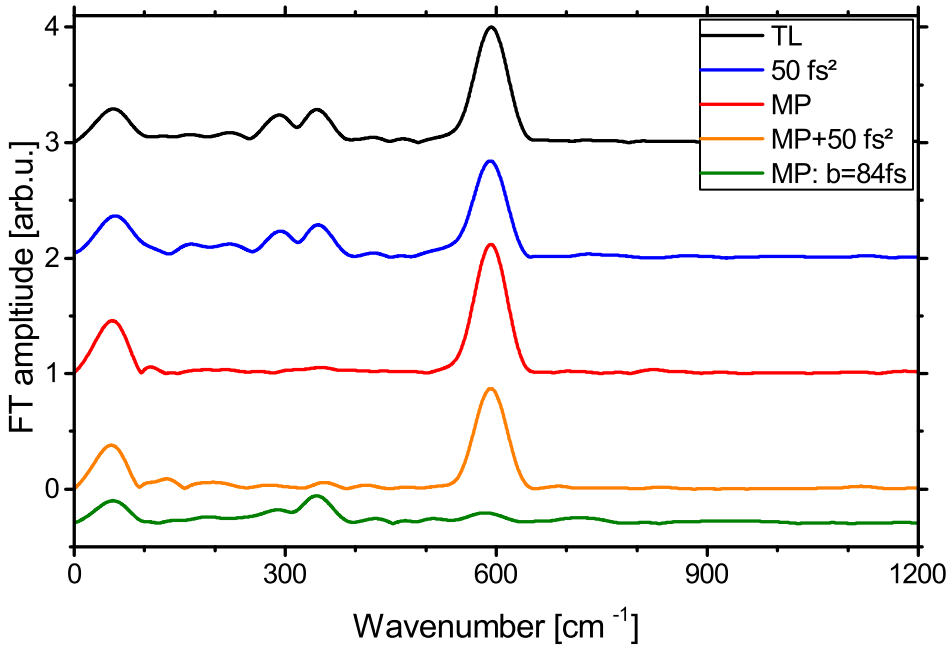

Figure 3.20: FT spectra for different temporal shapes for the resonant excitation probed at 610 nm. The overall spectrum for TL (black) and chirped (blue) excitation are similar while the amplitude of the mode near 600 cm^{-1} is reduced by positive chirp. A multipulse (MP) excitation with b = 56 fs (red) enhances this mode and suppresses modes around 300 cm^{-1}. The combination of multipulse and positive chirp (orange), decreases again the height of the maximum while the multipulse character of the excitation still leads to the suppresion of modes around 300 cm^{-1}. For b = 84 fs, i.e. an excitation out-of-phase to the dominating mode (green), in contrast nearly completely cancels the mode near 600 cm^{-1}, while especially the one at 350 cm^{-1} is still present.

The cancellation of the vibrational coherence by an out-of-phase multipulse shows that the vibrational coherence is very sensitive to the large variation of interpulse distance. In this context also the sensitivity of the ring-breathing mode about the exact multipulse should be examined. Therefore, the effect on coherence of multipulses with an interpulse spacing b of 53 fs, 56 fs and 59 fs, corresponding to wavenumbers of 565 cm^{-1}, 595 cm^{-1} and 629 cm^{-1}, respectively. It shows that already deviations of 5 % from the optimum interpulse distance decreases the vibrational coherence by up to 10 %.

Effect of Different Excitation Spectra

While the temporal shape of the excitation pulse is the central knob for control experiments, their success also crucially depends on the spectrum of the excitation pulse [14]. For this reason, the vibrational coherence, which is initiated by a TL pulse, is first compared for two spectra with the same central wavelength but different spectral bandwidths as well as for the four different excitation spectra shown in Figure 3.13. In all cases the excitation pulse is transform-limited.
The influence of the spectral width is examined for the far blue-detuned excitation spectrum The change of the spectral width is realized by blocking the spatially dispersed spectrum at the Fourier plane of the 4f set-up from both sides. While the central wavelength is maintained, the pulse duration elongates from 13 fs to 17 fs. The remaining spectrum covered a total bandwidth of 1700 cm^{-1} corresponding to less than 3 times the ring-breathing mode. The analysis shows that the absolute vibrational coherence of the ring-breathing mode drops to 85 % due to the reduced spectral bandwidth compared to the whole spectrum. It indicates that for a broader spectrum more vibrational levels are coherently excited, which allows for a higher control effect on the vibrational coherence.

In Figure 3.21 the vibrational coherence of the ring-breathing mode is shown in dependence on the probe wavelength. The maximum vibrational coherence appears in the region of negative TA signal between 620 and 645 nm for the red-detuned, resonant and near blue-detuned excitation spectra. For the far blue-detuned excitation, the vibrational coherence reaches about the same strength around 630 nm and 540 nm. The peak around 630 nm looks very similar even in the strength for both blue-detuned excitation spectra. In contrast, the data for resonant and red-detuned excitation show a double loop feature around a local minimum at 626 nm and 636 nm, respectively.
A second feature appears in the region of the ESA, between 520 nm and 545 nm. However, it appears with different intensities. For the far blue-detuned spectrum, it is as strong as the feature at higher wavelength. For the near blue-detuned and resonant excitation spectra, it is less intense. For the red-detuned excitation, the vibrational coherence is so weak in the ESA signal that it is close to a reliable detection limit.

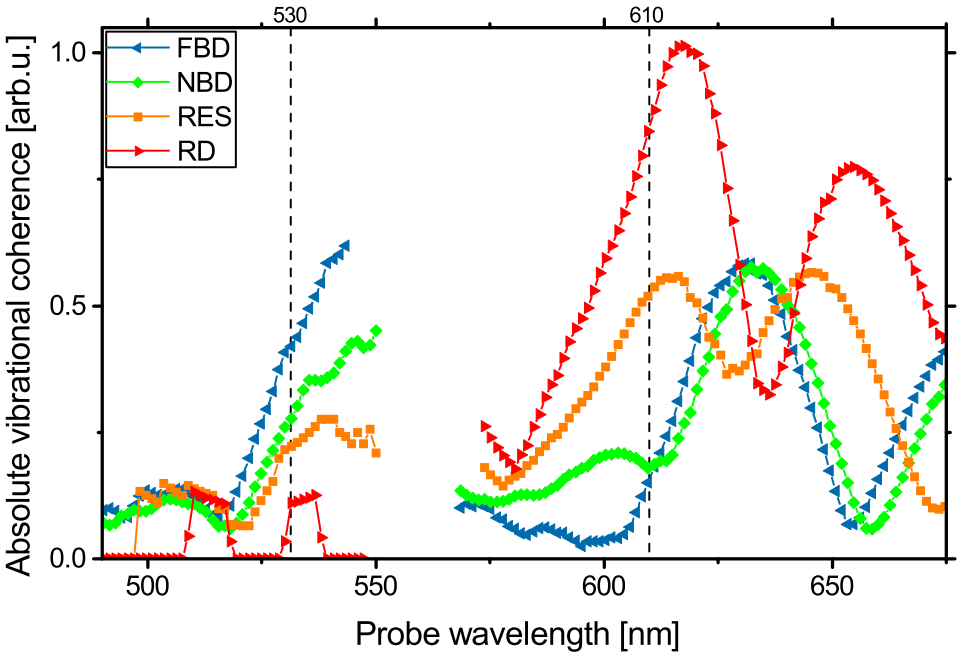

Figure 3.21: Absolute coherence plotted versus the probe wavelength for the different excitation spectra. The strongest vibrational coherence appears in the GSB signal for the near blue-detuned, resonant and red-detuned excitation. It has about the same strength in the GSB and ESA signals for far-blue detuned excitation spectrum. A second feature is visible around 530 nm, the position of the maximum ESA signal. The relative height of this feature compared to the maximum is strongest for the far blue-detuned excitation and decreases for near blue-detuned excitation and even further for the resonant excitation. This coherence is nearly not measurable for the red-detuned excitation. The two probe wavelength, which are examined in detail in Section 3.6.3 are 530 and 610 nm, labeled by dashed lines.

The data between 550 nm and 575 nm are cut as the TA signal, which is used for normalization, is close to zero and thus, causes divergent values for the vibrational coherence. Nevertheless, Figure 3.19 verifies its existence across the whole probe spectrum. Another feature appears for the far blue-detuned excitation, where at probe wavelengths from 570 to 605 nm the vibrational coherence is weaker than for the other excitation spectra. In conclusion, the vibrational coherence depends on the excitation spectrum and it also varied across the probe spectrum.

Phase of the Vibrational Coherence

Beside the FT amplitude also the FT phase is provides by the analysis of the oscillatory signal. The FT phase dependence across the probe spectrum provides information about the wave packet dynamics in the ground and excited state. As the vibrational coherence is influenced by the temporal and spectral shape of the excitation pulse, also effects on the FT phase are examined to get an insight into the modification of the wave packet dynamics in the ground and excited state.
Figure 3.19 indicates that the phase of the oscillatory signal changes across the probe spectrum as the second-derivate map shifts around 520 and 620 nm. In Figure 3.22 the oscillatory signal is shown for the probe wavelengths of 610 and 640 nm. The oscillations are just out of phase. The FT phase of the ring-breathing mode is plotted versus the probe wavelength (Figure 3.23) for all four excitation spectra to compare the impact of the different excitation spectra on the FT phase. The data sets for near blue-detuned, resonant and red-detuned excitation show a gradual change by π around the absorption maximum. The probe wavelength, where the change in phase starts, shifts from 615 nm (NBD) to 630 nm (RD). The data sets for far blue-detuned, near blue-detuned and resonant have a steep drop in the FT phase around 520 nm in common. This probe wavelength is blue-detuned to the maximum of the ESA signal.
It is also possible to extract the FT phase from 550 to 570 nm, where the TA signal is close to zero as no normalization is required for the phase information. An asymmetric peak appears at the same probe wavelength for the near blue-detuned, resonant and red-detuned excitation. The data for far blue-detuned does not show this signature. There is one steep jump around 615 nm and for increasing probe wavelength the FT phase decreases monotone.

Furthermore, the effect of the temporal shape on the FT phase is examined and also shown for the near blue-detuned excitation in Figure 3.24. It shows that the overall shape of the FT phase over probe wavelength does not depend on the tailoring of the excitation spectrum as the features around 520 and 620 nm look very similar. Only the shape of the peak around 570 nm varies between the temporal modulations.

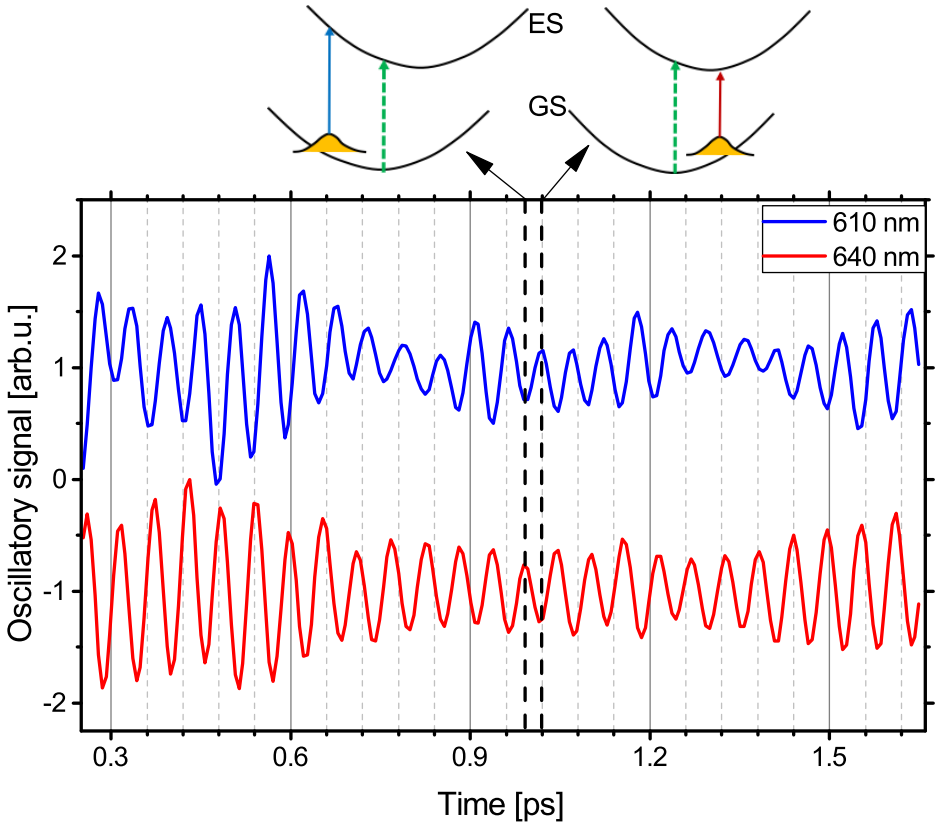

Figure 3.22: Oscillatory signal probed at 610 and 640 nm, corresponding to wavelengths on opposite side of absorption maximum (after TL near blue-detuned excitation). The oscillations of the two curves appear with a phase shift of π. Within half a period (corresponding to a phase shift of π) the wave packet travels from one side of the potential energy surfaces to the other one as visualized above the plot.

In summary, the FT phase of the vibrational coherence shows to be more sensitive to the spectral shape of the excitation pulse than to its temporal shape.

3.6.3 Enhancement of the Population and Vibrational Coherence due to Shaped Excitation

In this section, the effect of tailored excitation pulses on population and vibrational coherence is shown, which is the central part of the systematic study. The

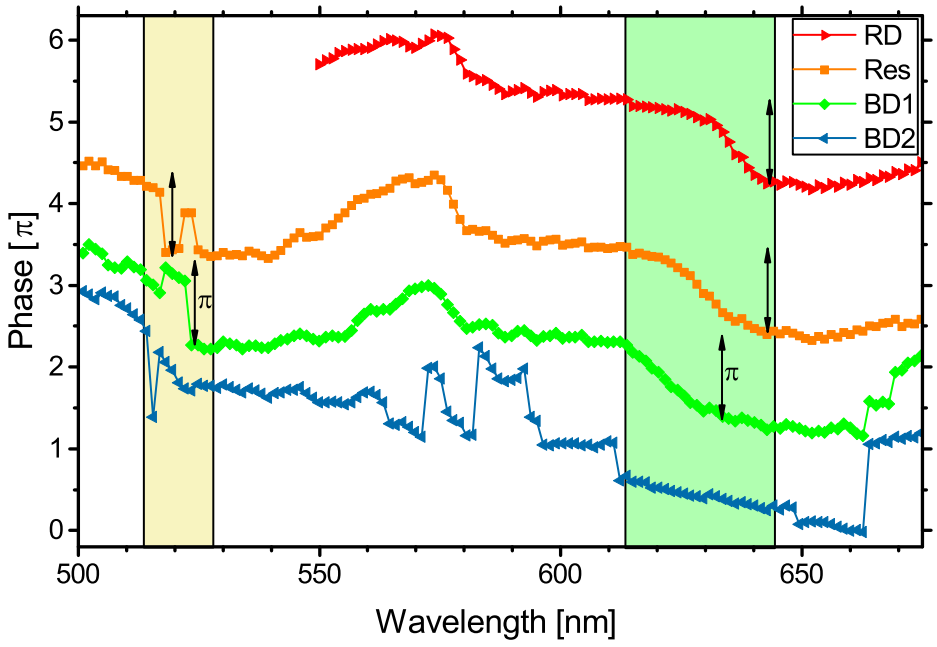

Figure 3.23: The FT phase of the ring-breathing mode is plotted versus the probe wavelength for the four different excitation spectra. Two π jumps (indicated by arrows) appear around 520 nm and 630 nm in the highlighted areas. For clarity, offsets between the curves are introduced.

population and vibrational coherence are determined from a polynomial fit of transients and the Fourier transform of the corresponding oscillatory signal, respectively, as described in Section 3.4. The enhancement factors for population and vibrational coherence quantify the effect on both quantities due to shaped excitation with respect to transform-limited excitation as defined in Section 3.4.5. These factors are determined for all excitation spectra over the whole probe range. However, due to clarity, the factors are only shown and discussed in the region of the ground state bleach (at 610 nm) and excited state absorption (at 530 nm) to make a statement about ground and excited state. While the ground state dynamics is probed around 610 nm, the corresponding TA signal is a measure for the population as well as the vibrational coherence in the ground state. In analogy, 530 nm probes the dynamics of the excited state and the provides information about the excited state population and the vibrational coherence. The errors on the enhancement factors shown in the following plots are determined from averaging the factors for several measurements.

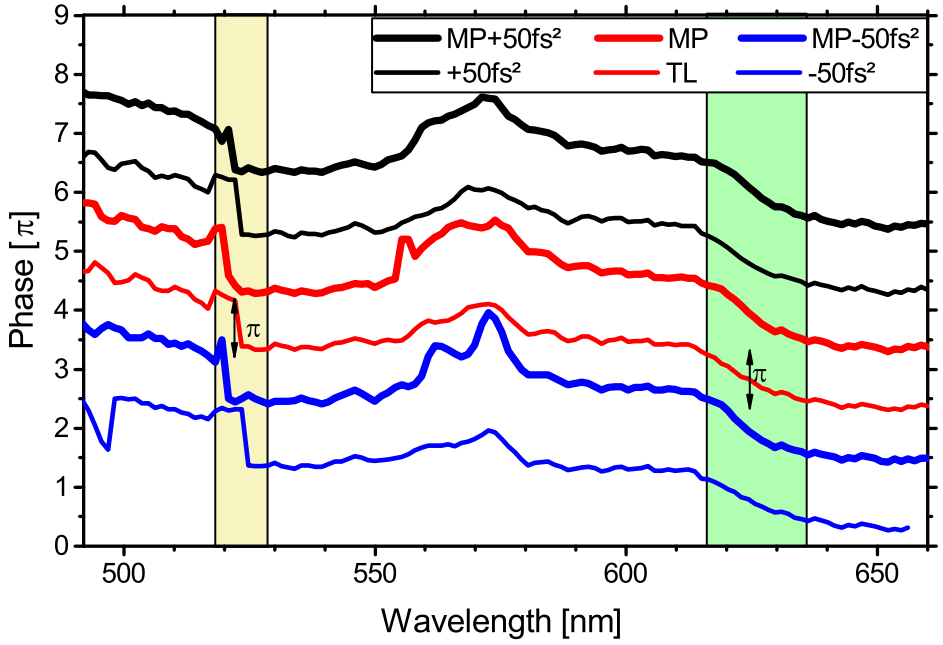

Figure 3.24: The FT phase of the ring-breathing mode is plotted versus the probe wavelength for different temporal shapes of the near blue-detuned excitation spectrum. The overall shape is nearly independent of the temporal shape. Two π jumps (indicated by arrows for the TL excitation) appear around 520 nm and 620 nm for all temporal shapes in the highlighted areas. For clarity, offsets between the curves are introduced.

Enhancement of the Population

As a first example, the effect of linear chirp in case of the resonant excitation on the population is examined. The TA signals are shown in Figure 3.25 for transform-limited as well as positively and negatively chirped resonant excitation pulses across the whole probe spectrum. The absolute values of the ESA and GSB signals increase for positive chirp. As the TA signal serves as a measure for the population (for the TL excitation indicated by the arrows), this means that the population in the excited state increases and the population in the ground state decreases[2]. For negative chirp it is inversed.
The enhancement factors due to temporal shaping, including chirped pulses, multipulse and chirped multipulses, with respect to TL excitation are determined

[2]For clarity: a more negative GSB signal implies that the ground state is more depleted

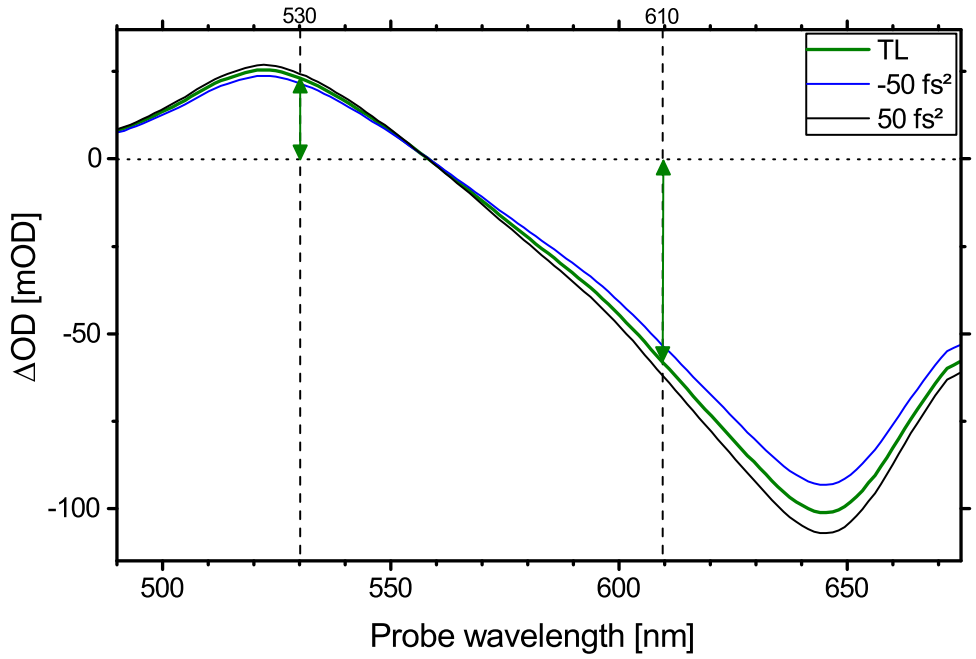

Figure 3.25: TA spectra for the resonant excitation with a TL pulse (green) as well as chirped pulses (50 fs^2 (black), -50 fs^2 (blue). The absolute values of the ESA and GSB signals increase for positive chirp, meaning that the population increases in the excited state and decreases in the ground state. In analogy, the reverse is true for negative chirp due to the decrease of the amplitudes. The arrows indicate which values of the TA signal are used as a measure for the populations in case of the TL excitation.

for the four excitation spectra and plotted for the two probe wavelengths 610 nm (Figure 3.26(a)) and 530 nm (Figure 3.26(b)) to quantify the enhancement of population in the ground and excited state due to shaped excitation pulses. The enhancement factors range between 0.9 and 1.15 for all probe wavelength and all excitation spectra. The maximum effect is observed for the resonant excitation while it is too small to distinguish for the near blue-detuned excitation spectrum. The data show three symmetries. First, tailored pulses, which show a positive enhancement at 530 nm, show a suppression at 610 nm and vice versa. Second, positive and negative chirp cause opposite impact. Third, enhancement of the multipulse is centered between the values for the two chirped multipulses. This last point can only be observed for red-detuned and resonant excitation, where

the impact is the largest. Furthermore, negative chirp and multipulses have a similar qualitative effect.

Enhancement of the Vibrational Coherence

The FT spectra for different temporal excitations are compared in Figure 3.20. Now, one takes a step back to visualize the differences in vibrational coherence which should be compared in the following. As an example, the same data sets as for Figure 3.25 are utilized and the oscillatory signal probed at 610 nm is shown for the resonant excitation with and without chirp in Figure 3.27(a). The overall shapes of the three curves are in good agreement and only the amplitudes of the oscillations are affected. Positive chirp causes a reduction of the amplitude while negative chirp increases it. To quantify the effect of the chirp the FT is determined as explained in Section 3.4.4. The comparison of the FT amplitude (Figure 3.27(b)) around 590cm^{-1} shows that the negative chirp leads to an enhancement of 10 %; the positive chirp causes a suppression of 15 %. One can deduce that the vibrational coherence is enhanced by negative chirp and suppressed by positive chirp using the resonant excitation spectrum. An intrapulse pump-dump mechanism as visualized in Figure 3.27(c) can explain the effect of chirp on the vibrational coherence in the ground state [12]. The blue wing of the negatively chirped excitation pulse creates a wave packet in the excited state, which is dumped back to the ground state by the red wing of the same pulse. This leads to an enhancement of the vibrational coherence in the ground state due to negative chirp. For positive chirp, this process is suppressed causing a reduction of the vibrational coherence in the ground state. As previously done for the population, now the enhancement factors for the vibrational coherence are calculated from the FT amplitudes (cf. Section 3.4.5) and plotted in Figure 3.28. It shows that the impact of tailored excitation on the vibrational coherence is more complex than on the population. The enhancement factors range between 0.6 and 1.5 for all probe wavelength and all excitation spectra. For ground and excited state, a symmetric behavior appears for chirped multipulses, i.e. enhancement factors for chirped multipulses are on opposite sides with respect to the one for the multipulse.

At 610 nm, the largest effects are observed for both blue-detuned spectra. Positive chirp, especially combined with a multipulse, shows the largest enhancement, while negative chirp and a negatively chirped multipulse shows about the same suppression of the vibrational coherence. Tuning the excitation to the resonant or red-detuned spectrum, the chirp dependence flips showing a strong impact of the excitation spectrum. Negative chirp leads to an enhancement and positive chirp suppresses the vibrational coherence, but the absolute value of the enhancement factors is less for these excitation spectra. The data display the tendency that the multipulse enhances the vibrational coherence for the near blue-detuned and resonant excitation, while it suppresses the vibrational coherence for the red-detuned. It has no effect for the far blue-detuned excitation.
At 530 nm, the data sets are more complex. The impact of the excitation spectrum in combination with chirp is less pronounced. Negative chirp suppresses the vibrational coherence with and without additional multipulse to a similar extent for all excitation spectra. Positive chirp enhances the coherence. While a positively chirped multipulse enhances the vibrational coherence for the far blue-detuned excitation, it causes a supression for the resonant excitation. For the latter excitation also the multipulse leads to a suppresion. For the red-detuned excitation, positive chirp and multipulse enhance the vibrational coherence.

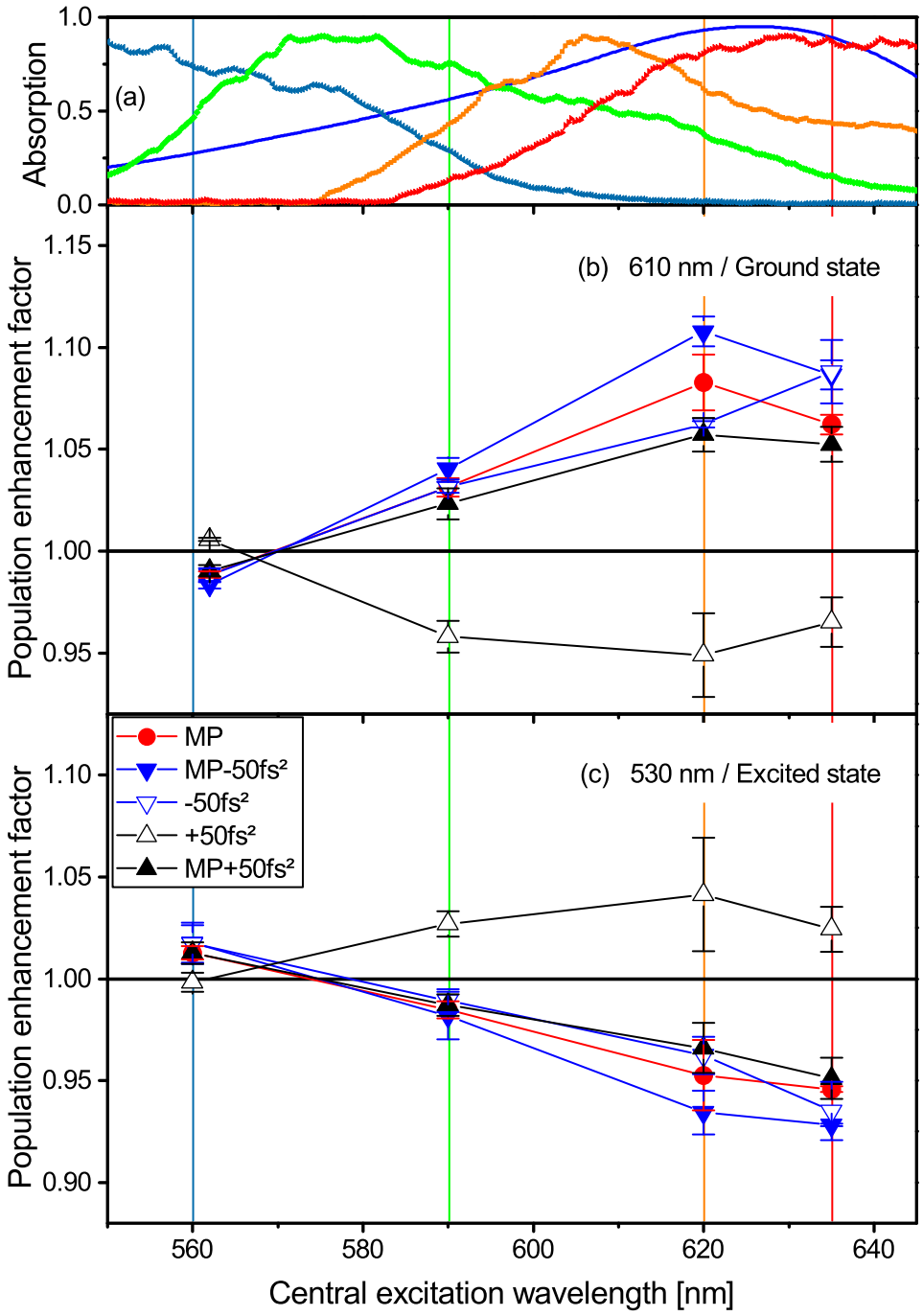

Figure 3.26: Enhancement factors for population for ground state (b) and excited state (c). For comparison the absorption spectrum and the four excitation spectra are shown (a); the labels are the same as in Figure 3.13.

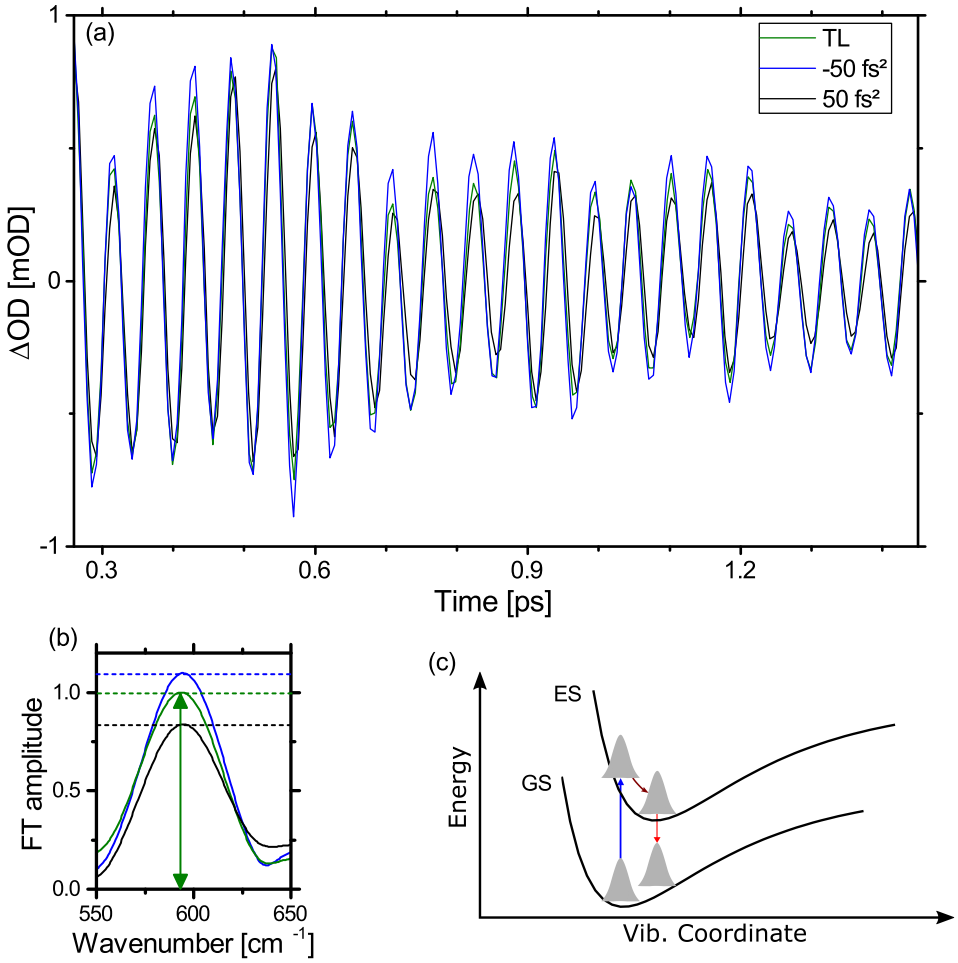

Figure 3.27: (a) The oscillatory signal probed at 610 nm for the resonant excitation with a TL pulse (green) as well as chirped pulses (50 fs^2 (black), -50 fs^2 (blue). (b) The corresponding FT spectra around 600cm^{-1} illustrating the impact of the linear chirp on the vibrational coherence. (c) A possible underlying process for the enhancement of the vibrational coherence in the ground state due to negative chirp has been proposed in [12] and is sketched here. The blue part of the excitation pulse creates a wave packet in the excited state, which is damped back to the ground state by the later coming red part of the pulse. For positive chirp, this process is suppressed.

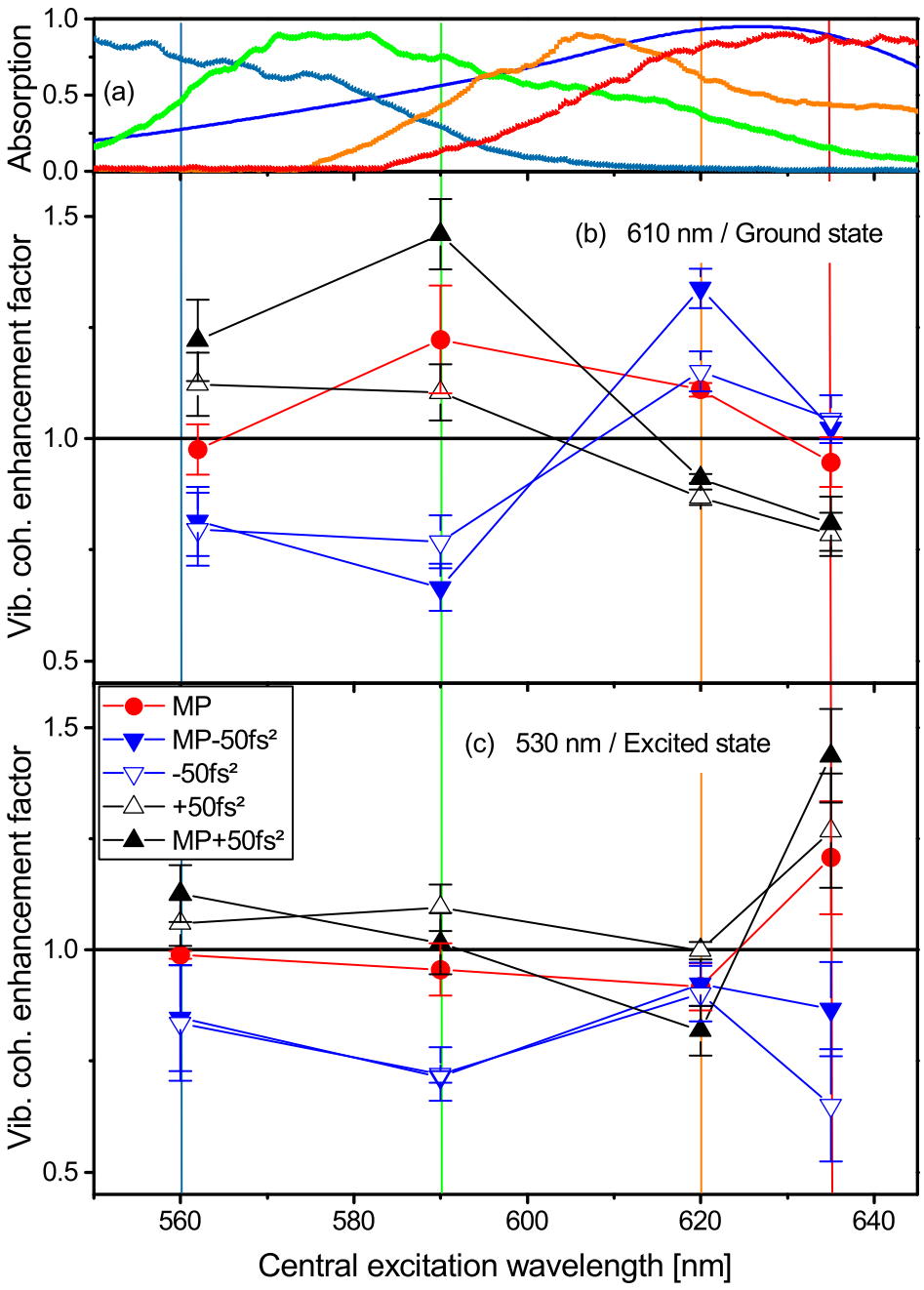

Figure 3.28: Enhancement factors for the vibration coherence for ground state (b) and excited state (c). For comparison the absorption spectrum and the four excitation spectra are shown (a); the labels are the same as in Figure 3.13.

3.7 Discussion

In the scope of the discussion, the results presented previously are discussed with literature. Furthermore, the control mechanism by shaped pulses should be interpreted in more detail because such a systematic study has not been performed before.

3.7.1 Vibrational Coherence

As the second-derivative map in Figure 3.19 is regular over time and across nearly the whole spectrum, one can conclude that the ring-breathing mode dominates the ground as well as excited state. This is in contrast to other molecular systems with several contributing modes. The peaks of the FT spectrum can crucially depend on the detection wavelength as shown for example for bacteriorhodopsin in Ref. [107].
To examine the contributions of further modes to the ground and excited state, FT spectra of both states are compared to the stimulated Raman spectrum.

Comparison with the Stimulated Raman Spectrum

The Raman spectrum of Nile Blue is measured (Figure 3.29(c)) for a better interpretation of the TA data. For best comparison, the Raman excitation wavelength should be chosen similar to the one used in TA. Therefore, the standard wavelengths 532 or even 633 nm of Raman microscopes would be favorable. However, the fluorescent background of Nile Blue is too dominant for these wavelengths and only the Raman peak of the dominant ring-breathing mode is resolvable. Consequently, the stimulated Raman spectrum is acquired with a red-detuned laser at 785 nm. As a minor compromise, it is compared to the spectrally resolved FT spectrum of the TA data for red-detuned excitation (Figure 3.29(a)). It is plotted with a logarithmic color code to allow for contributions from weak modes. The wavenumber axis is restricted to the resolution of the TA, focusing

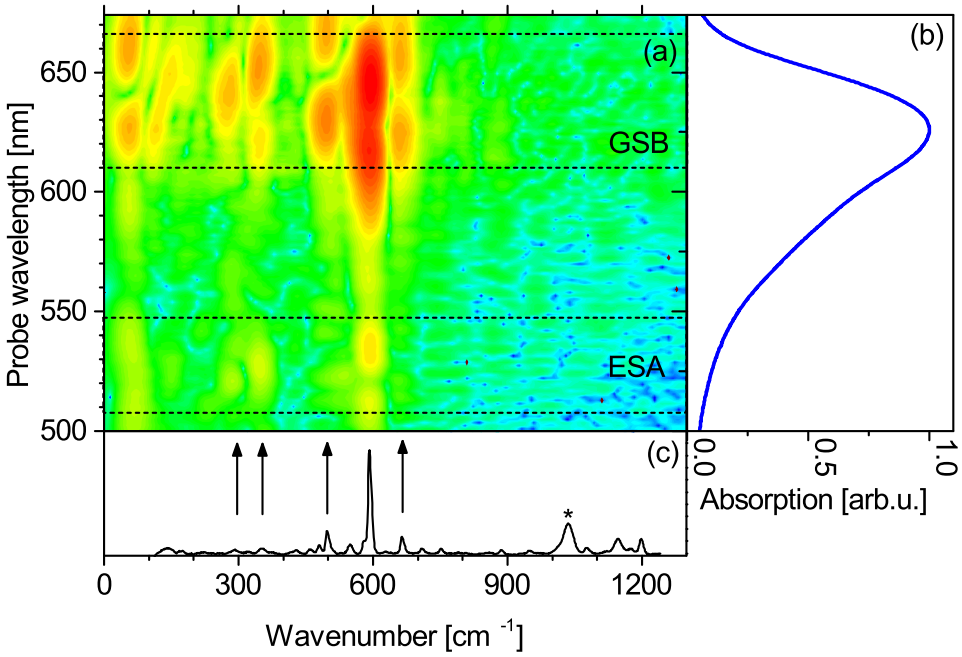

Figure 3.29: (a) FT spectrum versus wavenumber and probe wavelength after red-detuned transform-limited excitation. The color code is chosen to be logarithmic to be sensitive to other weak modes than the one around 600 cm^{-1}. This mode is most dominant around the absorption spectrum of Nile Blue (b). The FT spectrum can be directly compared to the non-resonant Raman spectrum (c) of Nile Blue dissolved in methanol from a red-detuned excitation at 785 nm. The (low-frequency) modes at 290.0, 354.8, 497.0, 592.1 and 664.7 cm^{-1} are in agreement with the FT spectrum in the GSB region and partially in the ESA region (both regions highlighted with a box).

on low-frequency modes. It shows the dominating mode to be at 592.1 cm^{-1}. Further (low-frequency) modes are at 290, 354, 497.0, and 664.7 cm^{-1}. These modes are also present in the region from 610 nm to 660 nm of the FT spectrum, only the mode at 548 cm^{-1} is hidden by the dominating mode due to the limited resolution of the FT. However, the modes in the Raman spectrum at 1145.8 and 1197.9 cm^{-1} do not appear in the FT spectrum.

The modes in the excited state (around 530 nm) are less pronounced, which is for the ring-breathing mode in agreement with the absolute vibrational coherence shown in Figure 3.21. Furthermore, the number of detected modes in the excited

state decreased. Beside the ring-breathing mode, only the modes at 290 cm^{-1} and 354 cm^{-1} appear while the ones at 497.0 cm^{-1} and 664.7 cm^{-1} are not visible

Effect of Different Temporal Excitation Shapes

The effect of multipulse excitation shown in Figure 3.20 proves that the vibrational coherence is addressable by the multipulse and especially, the vibrational coherence is canceled by an out-of-phase pulse with respect to the mode of interest. The peak at 50 cm^{-1} could be caused by a beating of two frequency modes as suggested in Ref. [84]. The modes have to be separated by 50 cm^{-1}. The Raman spectrum (Figure 3.16) shows at 548.9 cm^{-1} and 592.1 cm^{-1} relevant modes. In the FT spectra (Figure 3.20) these two modes cannot be resolved, but they contribute to the broad peak around 590 cm^{-1}. Other modes shown in the Raman spectrum, which are separated by about 50 cm^{-1} (at 290.0 cm^{-1} and 354.8 cm^{-1}; 497.0 cm^{-1} and 548.9 cm^{-1}; 592 cm^{-1} and 664.7 cm^{-1}) can be excluded as their amplitudes in the FT spectra are too low. Nevertheless, the peak at 50 cm^{-1} even remains for the multipulse with an interpulse distance of 84 fs, where the peak at 590 cm^{-1} vanished. This observation indicates that there has to be an additional contribution at 50 cm^{-1}. Possible candidates are torsional vibrational modes. These modes can be at such low wavenumbers, especially for coupled ring systems like Nile Blue [108].

Effect of Different Excitation Spectra

The overall shape mainly depends on the spectral shape of the excitation and less on its temporal shape as shown in Section 3.6.2.
The local minimum in the vibrational coherence is observed close to the absorption maximum for the resonant excitation and red-shifted by 10 nm for the red-detuned excitation (Figure 3.21). Assuming that the relevant potential energy surface has the shape of an anharmonic oscillator [82], this can be interpreted as probing there the minimum of a potential energy surface, where the wave packet is less localized than on the outer sides of the potential well. The observations

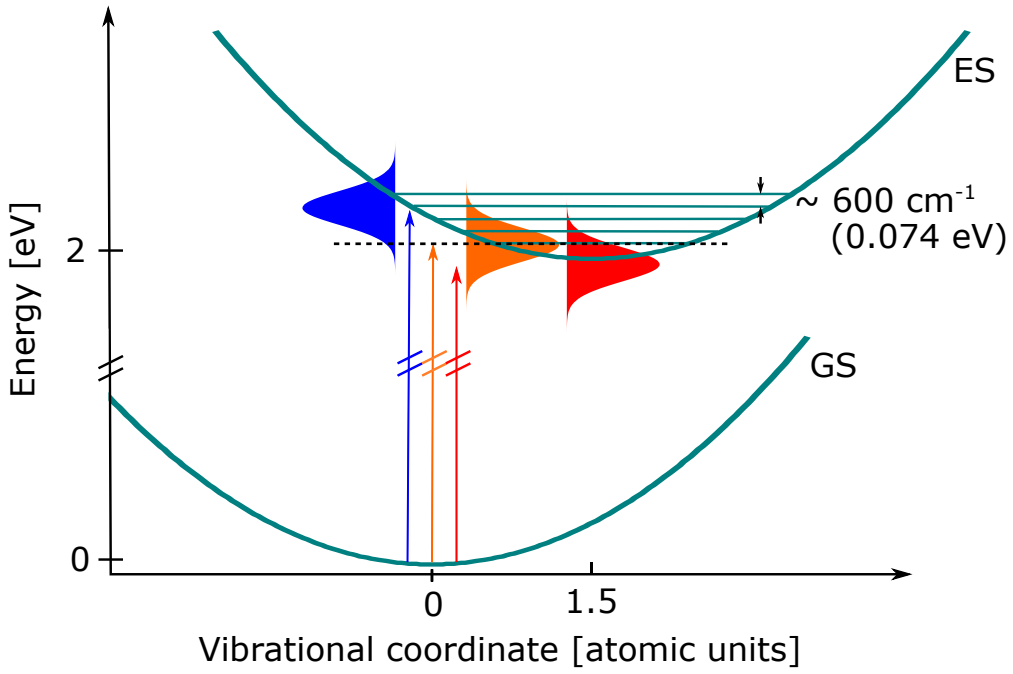

Figure 3.30: The ground and excited states are approximated by a one-dimensional system of displaced harmonic potential surfaces as proposed in Ref. [86]. The red-detuned excitation spectrum (indicated by the red Gaussian) only reaches the lowest vibrational states of the excited state with a part of its spectral bandwidth. In contrast, the whole spectral bandwidth of blue-detuned excitation spectrum (blue Gaussian) covers vibrational states. The resonant case (orange) is in between. The excitation spectrum crucially influences the vibrational coherence in the excited as well as in the ground state.

for resonant and red-detuned are in good agreement with [82, 84] although there the excitation spectra had a noticeable different shape. It allows the assumption that the wave packet is probed on a potential energy surface of similar shape in all cases. To visualize the effect of the different excitation spectra, the ground and excited states are approximated by a one-dimensional system of displaced harmonic potential surfaces as proposed in Ref. [86]. The displacement is 1.5 atomic units and the vibrational modes are separated by about 600 cm^{-1} (Figure 3.30).

Nevertheless, the overall shape of the vibration coherence completely changes for the near blue-detuned and far blue-detuned excitation spectra, where only a single peak appears in the region of maximum absorption. This is in qualitative

agreement with Ref. [85], where the vibrational coherence of LD690 is examined in dependence on the excitation spectrum as well as linear chirp. The spectral range of the excitation directly determines which modes of the molecule are addressed at all. Depending on that also the coupling between different modes can be affected. The results here indicate the complex dependence of the vibrational coherence on the excitation spectrum.

Besides the overall shape, also the absolute height of the vibrational coherence should be discussed. Remarkable is the red-detuned excitation, which shows maximum amplitudes above probe wavelengths of 600 nm and minimum amplitudes below 550 nm. This can be interpreted that the red-detuned excitation pulse mainly addresses the ground state while the excited state is nearly reached. In comparison, the amplitudes for resonant and blue-detuned excitations are comparable above 600 nm. It implies that after reaching a resonant threshold, the vibrational coherence cannot be further enhanced by tuning the excitation further to the blue. For the excited state in contrast, the detuning has a more profound impact and the vibrational coherence increases for more blue-detuned excitations meaning that more higher lying vibrational levels are reached by the excitation (c.f. Figure 3.30).

Phase of the Vibrational Coherence

The broadband probe spectrum allows to sample the wave packet over time at different positions of the potential energy surface. The temporal information can be expressed by the phase of the oscillatory signals. In early days of femtosecond spectroscopy, the phase of oscillatory signals was analyzed to differ coherences in ground and excited state [86, 109–111]. However, it showed that this method is limited by the extraction of the phase and it is very challenging to interpret the results.
The π jump in the phase of the dominating mode around the absorption maximum (c.f. Figure 3.23) is seen as proof that the two edges of the potential energy surface are probed and the wave packet moves within half a period from one edge to the other. Such π jump have been reported in earlier papers on various

oxazine such as LD690[3] [82, 85] and Oxazine 1 [84]. The underlying process for the ground state wave packet is visualized with a schematic picture in Figure 3.23. The wave packet evolves from one side of the potential energy surface to the other one within half a period. These two turning points are probed with two different wavelengths on both sides of the absorption maximum due to the displacement between the potential energy surfaces of ground and excited state. As the wave packet is less localized at the center of the oscillator potential than on the outermost points, this phase jump typically coincides with a local minimum of the FT amplitude. In Ref. [84], the probe wavelength of the phase jump and of the local minimum, in terms of strength of the FT amplitude, coincided for an excitation covering the blue wing of the absorption spectrum. In our measurements, this holds for the resonant and red-detuned, but it is not the case for the blue-detuned excitation spectra. This indicates that predominantly the ground state is probed for the resonant and red-detuned. In contrast there seems to be overlapping contributions from the ground and excited state at the same probe wavelengths above 620 nm for the blue-detuned spectra. These observations indicate the strong sensitivity of the phase on the interplay between absorption and excitation spectra, which makes a comparison between measurements very challenging.

The phase shift at 516 nm is consistent for the resonant and both blue-detuned excitation spectra. Such a phenomenon in the ESA signal was already reported for a broadband excitation of LD690 [85]. In contrast to the data shown in Ref. [85], we also analyzed the oscillations in the ESA signal in more detail and are able to combine these results. Figure 3.21 shows a local minimum in the vibrational coherence around 516 nm for all excitation spectra showing a link between the FT amplitude and the FT phase in this case. Although the probe wavelength is red-detuned with respect to the maximum of the ESA signal, one can conclude that at these probe wavelengths only the motion of the wave packet on the potential energy surface in the excited state is probed.

Furthermore, the overall shape of the FT phase is independent of the tailoring of the excitation in the regions below 540 nm and above 590 nm (Figure 3.24). The FT phase in dependence on linear chirp was in accordance with an earlier ex-

[3] LD690 with its chemical formula $C_{18}H_{22}N_3O_5Cl$ has a similar structure as Nile Blue but one carbon ring less.

perimental studied at the fluorescent dye Sulforhodamine-B in the ground-state bleach signal by Wand *et al.* [63]. Our measurements show that this is also the case for multipulse and chirped multipulse excitation. The independence of the FT phase in the ground-state bleach signal can be interpreted as an indicator for dominant contributions from the ground state vibrational coherence. In contrast, the features around 560 nm allows the assumption that the mixture of ground and excited state is probed in this range.

As this overview shows, there are already many details of Nile Blue, which can be studied based on the data sets. However, at this point the discussion will be continued with a focus on the enhancements due to shaped excitation pulses.

3.7.2 Enhancement of the Population and Vibrational Coherence due to Shaped Excitation

Based on the previous discussion, the two probe wavelengths 610 and 530 nm are assigned to probe the electronic ground and excited state, respectively. In the following, the enhancement of these states by shaped pulses im comparison to TL pulses with different spectra are discussed, which represents the central part of the systematic study.

Enhancement of the Population

In general, the symmetry in the enhancement of the population for 610 nm (ground state) and 530 nm (excited state) allows the interpretation that a positive enhancement in the excited state directly leads to a suppression of the ground state .

The results that the ground state population (Figure 3.26(b)) is enhanced by negative chirp and suppressed by positive chirp, especially for resonant excita-

tion is in qualitative agreement with a recent theoretical study, which is based on a non-perturbative, time-dependent density matrix approach, on the effect of linear chirp in dependence on the excitation spectrum [112], although the enhancement factors there are smaller.
The displacement of the harmonic potential energy surfaces of ground and excited state along a nuclear coordinate (c.f. Figure 3.30) could be the reason for the insensitivity to the temporal shape of blue-detuned excitation pulses. This nearly independence of ground state population on the chirp for the far blue-detuned excitation spectrum is in accordance with the study at oxazine 1, where a blue-detuned excitation has been chosen to study the population in the ground state [83].
The multipulse demonstrates a similar influence as negatively chirped pulses. The highest enhancement is achieved for the resonant excitation. The overall shape of the enhancement for multipulse excitation has already been predicted theoretically, where also the non-perturbative, time-dependent density matrix approach is utilized [14].

The results indicate that the excited state population (Figure 3.26(c)) is enhanced by positively chirped pulses. This can be explained by the fact that stimulated emission is suppressed [113]. Apparently, the effect is especially strong for resonant excitation and decreases for increasing detuning of the excitation spectrum. Furthermore, our chirp dependence reproduces earlier fluorescence measurements on LD690 [114]. An increased population transfer to the excited state due positively chirped pulses is also proven for red-detuned excitation of the laser dye IR 125 in a feedback control experiment [115]. With the new systematic study, this phenomenon can be extended to multipulse excitation as well, where the tendency of the multipulse is comparable to negative chirp.
Last but not least, the results for the multipulse excitation show qualitative agreement with earlier measurements and theory for the excited state [14]. In the case of chirped multipulses, an ordering occurs. Negative chirp amplifies the effect of the multipulse while positive chirp reduces it. The combination of chirp and multipulse shows an interplay of both quantities for the resonant and red-detuned excitation spectra, where the multipulse is dominating the effect on the population. Negative chirp shows the same trend as a multipulse

excitation, so negative chirp added to the multipulse leads to a more pronounced effect. In contrast, positive chirp causes an opposite effect, therefore, the effect of negatively chirped multipulses is weakened in comparison to a multipulse excitation.

Enhancement of the Vibrational Coherence

While the population enhancement factors of both states are related to each other, this is not the case for vibrational coherence. This indicates that the latter can be created and destroyed by many more impact factors as shown in Figure 3.20. The vibrational coherence enhancement factors range from 0.6 to 1.4 for ground and excited state.

For the resonant and blue-detuned excitation spectra, negative and positive chirp leads to and enhancement and suppression of the ground state, respectively (Figure 3.28(b)). This is in qualitative agreement with earlier measurements, where the effect of positive and negative chirp on the vibrational coherence in LD690 was examined [82]. However, a detailed comparison shows that the enhancement factors in Ref. [82] range from 0 to 2. Comparing the experimental details allows two possible explanations, why the absolute values differ. First, the absolute value for linear chirp is less in our case, as the combination of chirp with multipulse limits the maximum chirp. Second, for the reported experiments the excitation pulse covers the whole absorption spectrum. Our excitation spectra, in contrast, cover only different parts around the maximum of the absorption spectrum.
An extreme influence of the excitation pulse in combination with linear chirp can be observed in Figure 3.26(b). For the resonant excitation spectrum negative chirp enhances the vibrational coherence in the ground state while positive chirp causes a suppression. In contrast, positive chirp enhances the vibrational coherence and negative chirp suppresses it, when the excitation spectrum is tuned to the blue wing of the absorption spectrum. The suppression of the vibrational coherence in the ground state for blue-detuned negatively chirped excitation is in agreement with Ref. [85]. These measurements show that the

pump-dump scenario proposed in Ref. [12] is not universal. This statement is also confirmed in Ref. [112] although there positive chirp led to enhancement of the vibrational coherence in the ground state in a very narrow spectral range, while negative chirp leads to a suppression. A possible explanation for the flip in our measurements can be the following. Comparing the resonant and far blue-detuned excitation spectra shows that there is only a small spectral overlap. However, just this part of the spectrum hits first the sample molecules not only in case of a positively chirped far blue-detuned excitation but also in case of a negatively chirped resonant pulse. Inverting the sign of the chirp of the two pulses has as a consequence that this spectral component hits the sample as the very last. Therefore, it could be assumed that not the ordering of all spectral components matters but the timing of a specific component is also crucial. Such an interpretation is only possible as the excitation spectrum is carefully tuned across the absorption spectrum. Furthermore, tuning the excitation spectrum from resonant to red-detuned shows a decrease of the enhancement for all temporal shapes probably due to the shrinking spectral overlap between excitation and absorption spectrum. The decrease is stronger for the multipulse and the chirped multipulses than for the chirped pulses.

The multipulse excitation seems to be independent of this phenomenon. The enhancement of the vibrational coherence in the ground state observed here for the resonant and near blue-detuned is in contradiction to the calculations in Ref. [14], where a strong suppression, i.e. an enhancement factor down to 0.6, around the absorption maximum is predicted. However, this is currently the only available comparison.

The combination of chirp and multipulse has an impact for the resonant and red-detuned. An enhancement (suppression) due to the multipulse leads to an increase (decrease) of the enhancement factor for the chirped multipulse in comparison to the chirped pulse. For the near blue-detuned excitation, this is only valid for positive chirp while there is no impact on the negatively chirped pulse by adding a multipulse. The latter observation is also made for the far blue-detuned excitation. In contrast, the effect of a positively chirped far blue-detuned multipulse is stronger than that of a chirped pulse, while the multipulse has no effect at all. This can be interpreted, as in this special case, the enhancement of temporal ordering of the spectral components within a positively chirped pulse

can be amplified by adding a multipulse, while a multipulse cannot trigger this enhancement.

The same phenomenon can also be observed in the excited state for the far blue-detuned excitation (Figure 3.28(c)). However, this is the only correspondence between ground and excited state. Positive chirp leads to an enhancement, while negative chirps causes a suppression, especially for near blue-detuned and far blue-detuned excitation spectra. According to the theoretical study done in Ref. [63], the effect of chirp is stated to be limited to suppression of vibrational coherence in the excited state for a resonant Gaussian pulse. Our measurements show that this is not the case for blue-detuned excitation pulses. Enhancement of the excited state is also proposed in Ref. [112] in two very narrow windows for the excitation spectrum. As there is a discrepancy in the excitation spectrum as well as in the states representing the molecule in the study, an enhancement due to positive chirp and a suppression due to negative chirp independent of the excitation spectrum are not surprising.
Last but not least, the vibrational coherence shows a qualitative agreement for the multipulse excitation with the experimental data and calculations reported in Ref. [14]. However, the experimental enhancement factors given in Ref. [14] range from 0.85 to 1.85. This large range is in better quantitative agreement with the measurements here with a positively chirped multipulse while the overall shape is similar for the multipulse excitation. This comparison hints on the possibility that the multipulse utilized in Ref. [14] had some additional positive chirp.

However, the interpretation of the data for vibrational coherence in the excited state is challenging as higher lying states and also competing processes to the ground state are involved. Especially, the results for the red-detuned excitation should be seen critical as the vibrational coherence in the excited state is very weak.
Thus, the effect on the coherence seems to be dominated by the chirp and less by the multipulse. Furthermore, the trend of multipulse and positive chirp shows some similarity. Both observations are in contrast to the population, where the multipulse is dominating and negative chirp and multipulse give the same trend.

In conclusion, this allows one to conclude that the effect on the coherence is chirp while the effect on the population is dominated by the multipulse.

The combination of enhancement in population and coherence can be used to give a final guideline: For the best enhancement of the excited state a blue-detuned positively chirped multipulse is ideal. A resonant negatively chirped multipulse is the best choice for an enhancement of the ground state. These two recommendations show indeed that the combination of chirp and multipulse, especially with a tunable excitation spectrum, build a successful tandem for the selective enhancement of molecular states.

Based on this guideline, a possible explanation can be given, why various control experiments failed in the past. One of the few unsuccessful trials, which was published, concerns the excitation of single molecules [15]. The publication states that the population in the excited state cannot be controlled by tailoring the pulse shape alone in the weak-field limit. This is shown for one excitation spectrum, which covers the whole molecular absorption spectrum. However, the results of the systematic study performed in the scope of this thesis imply that the excitation spectrum has a significant impact on the controllability of the population as well as the vibrational coherence. Subsequently, it seems to be reasonable to recommend a repetition of the experiments presented in Ref. [15] for different excitation spectra to examine the generality of the statement concerning the controllability.

3.8 Conclusion

In conclusion, the study shows how sensitive population and vibrational coherence in ground and excited state are in the low-intensity regime to the temporal and spectral shape of the excitation pulse. For the first time, a systematic study including the spectral shape as well as linearly chirped pulses, multipulses and chirped multipulses excitation has been realized. It shows that it is difficult to enhance population and coherence of the excited state simultaneously; however,

a blue-detuned positively chirped multipulse is favorable. The best choice for the ground state is a resonant negatively chirped multipulse. These results can be seen as a guideline for parameter sets to perform successful control experiments in the future.
In the near future, the topic will be investigated from the theoretical side with nonperturbative, quantum dynamic calculations. For such a simulation, input parameters like the light field should be chosen according to the experimental parameters. The comparison of experiment and theory allows to get a deeper insight into the control mechanisms.

Development of an AOM-Based Shaping System in the Ultraviolet

4

Inspired by the success of control experiments in the visible like the one in the previous section, the spectral range of shaped pulses is expanded to the ultraviolet (UV). In this spectral regmine, Small molecules and organic compounds, which are of special interest for several reasons, predominantly absorb. However, the experimental realization of shaped laser pulses in the UV is challenging. In the scope of this thesis, a shaping system in the UV was developed, which is presented in the upcoming chapter. The first section, the motivation for tailored femtosecond pulses in the UV as well as for control experiments in this spectral range is given. Next, the status quo of UV shaping is briefly described and the choice of the system, which is based on an acousto-optical modulators (AOM) is justified. Subsequently, the working principle of the AOM is explained. The section about the implementation of the device in the UV includes the optical and electronical configuration as well as the description of the spectral calibration. For the characterization of the AOM, its shaping performance is investigated and the shaping limitations are depicted. These specifications are compared to the ones of other shaping devices. The final section summarizes the performance of the AOM-based shaping system and an outlook for the application of shaped UV pulses is given.

4.1 Motivation

There is an extensive interest in shaping femtosecond pulses in the UV as many organic molecules absorb in this spectral range. A classic example is the DNA nucleobases, where they display the process of UV-induced ring dimerization, and which also have strong links to UV-induced cancer and mutagenic ailments [116, 117]. Indeed, many of the simple, small molecular systems (with typically less than 30 atoms) have valence, electronic transitions in the UV regime. Furthermore, a lot of these molecules occur in various biomedical and pharmacological avenues of research; and subsequently due to their intrinsically small atom composition, they are better candidates for highly sophisticated computational and theoretical studies. This is very appealing to experimentalists that wish to couple sophisticated experimental methodologies to robust theoretical background. However, in order to do this, the generation [24–26] and shaping [27–30] of UV laser pulses must progress further. For this reason, a shaping system in the UV was developed in the scope of this thesis.

4.2 Current Status of UV Shaping

The development and application of shaping devices are especially challenging in the UV due to restrictions such as transmissivity, damage threshold and the limitations on the desired spectral bandwidth. For the UV shaping, several techniques were realized, which are based on various concepts. An overview over these techniques is given in the following. Some of them were originally applied in the visible or near-infrared range and adapted for the UV.

Micro-Electro Mechanical System

A micro-electro mechanical system (MEMS) consists of an array of reflective micro mirrors. Such an array is placed at the Fourier plane of a 4f set-up (cf.

Section 2.2.1. The spatially dispersed spectral components of the femtosecond pulse are reflected from different micro mirrors. The position of each mirror can be controlled independently along the propagation direction of the light to introduce a phase shift of the individual spectral components. As the incidence of the light is perpendicular to the surface, the phase modulation is independent of the light polarization. Tilting the micro mirrors allows amplitude shaping in addition. Like the LCM, which was used in the previous chapters, the performance of the MEMS suffers from the pixelated modulation and the gaps between the micro mirrors. For the shaping set-up with a reflective MEMS only one grating and one focusing mirror are required and the shaped pulse is coupled out after passing the grating for the second time. Choosing appropriate coating of the micro mirrors, shaping of UV femtoseconds was demonstrated [27, 118]. Beside their use phase and amplitude modulator, MEMS were implemented for reducing spatial chirp of the pulse [119] and also as shaper-assisted UV cross correlator [45].

Acousto-Optic Modulator

In case of an AOM, a diffraction grating is generated by an acoustic wave inside a material. The diffracted light can be modulated by adjusting the shape of the acoustic wave. The working principle of AOMs will be discussed in detail in section 4.3. The performance of the AOM does not suffer from pixel gaps as the mask is generated by a continuous waveform. However, the application is limited to pulsed systems with a repetition rate smaller than 100 to 300 kHz, because this waveform is not static. The AOM allows for changing the pulse shape from shot to shot.
Pioneering work on shaping by AOM was demonstrated by W. Warren and co-workers in the 1990s using the titanium-sapphire oscillator at 780 nm [18, 120]. Its first application for Uv pulses is reported in Ref. [121].

Acousto-Optic Programmable Dispersive Filter

A very different type of shaper is the acousto-optic programmable dispersive filter (AOPDF), which is also known with its commercial name "Dazzler". It does not need a 4f set-up as the light passes collinearly with an acoustic wave in an anisotropic birefringent medium (e.g.a potassium dihydrogen phosphate crystal). An diffraction grating is generated by the acoustic wave. The phase matching condition between the ordinary and extraordinary axis is fulfilled for each diffracted spectral component by a specific acoustic radio frequency. During the diffraction process, the polarization of the light is rotated from the fast extraordinary to the slow ordinary axis. The shape of the acoustic wave determines, where in the crystal the single spectral components are diffracted and therefore, the group delay of the components is shaped. The amplitude of the diffracted spectral components is controlled via the magnitude of the acoustic wave. The diffracted beam leaves the crystal parallel to the undiffracted beam but with a certain spatial offset.
Its first successful operation for adaptive compensation of group delay time dispersion was published in 1997 [19]. More advanced pulse shapes of 30-fs pulses were reported a few years later in the near-infrared [122] and visible regime [123]. The first shaping of UV pulses with an AOPDF was reported in 2006 [29]. Four years later, the shaping of sub-20 fs pulses was achieved [124].

Indirect Shaping and Ultraviolet Liquid-Crystal Modulator

Commercial LCMs as used in the previous chapters are limited to the visible and near-infrared spectral region. Subsequently, the basic idea of indirect shaping is to shape the phase and amplitude of a pulse in the visible or near-infrared regime, e.g. by an LCM. This pulse is then transferred to the UV by frequency upconversion like sum frequency mixing. In this case the repetition rate as well as possible problems with pixel gaps are determined by the shaper chosen to shape this fundamental wavelength.
This method was first applied to the fourth harmonic at 204 nm of a Ti:sapphire laser system [28]. Sub-20 fs pulses in the range from 295 nm to 450 nm were

generated via sum frequency mixing between a broadband NOPA output in the visible and a pulse at 775 nm [125]. More recently, the technique of four-wave mixing was applied for the generation of sub-30 fs pulses at 237 nm [126].

To directly shape UV pulses with an LCM, the development of a new type of liquid crystals in material science was needed and finally succeeded. It allows for transferring the concept of LCMs into the UV with sufficient damage threshold and transmissivity in the UV. The realization of a prototype device and its application for UV shaping were reported ten years ago [53, 127]. In the following, it will named UV-LCM to distinguish it from the succeeded LCMs as utilized in the previous chapters.

Choice of the New Shaping System

Beyond these various shaping systems, the AOM was chosen for the newly developed set-up for several reasons. A MEMS was utilized earlier in our research group [43, 118]. Its update rate is smaller than the 1 kHz rate of the laser system. Furthermore, it suffers from shaping artifacts due to the pixelation and the spatial gaps between the micro mirrors, which can disturb the application of the shaped pulses [124]. This is also a disadvantage of the UV-LCM, which is furthermore a prototype shaping system and which so far does not allow for simultaneously phase and amplitude shaping. The indirect shaping technique offers a high flexibility regarding the shaping of amplitude or polarization beside phase. However, the implementation is challenging and especially, it is not required for the application of unshaped pulses. In addition, the effect of the phase instabilities as observed in Chapter 2 could add further complications in the UV. In contrast, the AOPDF is easy to implement as it does not need the 4f set-up at all. Nevertheless, its diffraction efficiency is lower than the one of the other shaping set-ups and it adds much group velocity dispersion due to the length of the material. Another aspect is the price for the AOPDF, which is at least twice as high as the one for the whole new AOM set-up.
The work of T. Weinacht and co-workers [30] on an AOM-based set-up served as a template for the development. The set-up in Ref. [30] was optimized for shaping

the third harmonic (262 nm) of a Ti:sapphire laser with a spectral bandwidth of about 3 nm. Fundamental modifications of this set-up were required to realize the shaping of pulses with a central wavelength between 250 nm and 350 nm and a spectral bandwidth of up to 7.7 nm, which allows for a further degree of freedom in the form of tunability in the UV shaping.
A more detailed comparison of the specifications and performance of the various UV shaping systems will be given in Section 4.6, which also includes the newly developed system.

4.3 Working Principle of the Acousto-Optic Modulator

The working principle of the AOM is based on light-matter interaction. A radio frequency voltage is converted by a piezo-electric transducer to a photoelastic medium. Therefore, an acoustic wave travels through the material. On the atomic level this means that in the solid state the atoms vibrate around their position of equilibrium. This changes the density of the material locally and consequently, the refractive index is modified as depicted in Figure 4.1. The resultant time- and position-dependent refractive grating can be described by a sinusoidal change of the refractive index, n, according to

$$\delta n(t, x) = \delta n_0 \sin(\omega_{RF} t - kx). \tag{4.1}$$

The frequency, ω_{RF}, is defined by the carrier radio frequency F as

$$\omega_{RF} = 2\pi F. \tag{4.2}$$

The wave number, k, is gives as

$$k = \frac{2\pi}{\Lambda}, \tag{4.3}$$

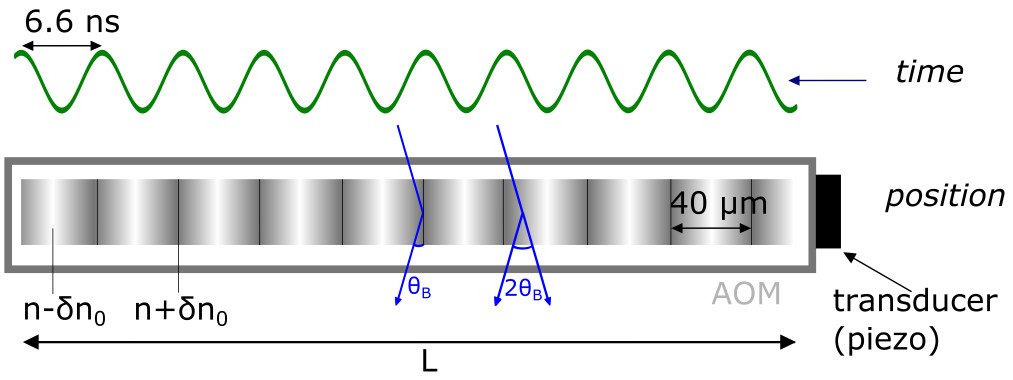

Figure 4.1: Schematic of the diffraction of light inside the AOM. A piezo transducer initiates an acoustic wave with a radio frequency F passing the optical medium of length L. The acoustic wave causes a traveling refractive grating with the acoustic wavelength Λ. Light passing the medium sees the grating as quasi-static. Constructive interference of the reflected light occurs for maximum reflectance whenever the Bragg condition, (4.7), between light wave and acoustic wave is fulfilled.

where the acoustic wavelength Λ,

$$\Lambda = \frac{v_a}{F}, \tag{4.4}$$

depends on the speed of the acoustic wave, v_a, inside the medium.
The magnitude of the grating, δn_0, is proportional to the square root of the intensity of the acoustic wave, I_a:

$$\delta n_0 \propto \sqrt{I_a}. \tag{4.5}$$

As Eqn. (4.1) indicates, the grating is not static but moving with v_a. However, as

$$v_a \ll c, \tag{4.6}$$

where c is the speed of light, it can be assumed that the reflective grating is quasi-static for the reflection of light. For constructive interference within the refracted light field, the Bragg condition,

$$\begin{aligned} \sin(\theta_B) &= \frac{\lambda_m}{2\Lambda} \\ &= \frac{\lambda_m}{2n\Lambda} \end{aligned} \tag{4.7}$$

has to be fulfilled[1], where $\lambda_m = \lambda/n$ is the light wavelength inside the medium. As long as the acoustic wave is not too strong, the reflectance R is proportional to I_a:

$$\begin{aligned} R &\propto I_a \\ &\propto \delta n_0. \end{aligned} \tag{4.8}$$

To realize the shaping of femtosecond pulses, the AOM is placed at the Fourier plane of a 4f set-up. The device is not placed perpendicular to the propagation direction of the light as in the case of an LCM or MEMS, but the Bragg condition (Eqn. (4.7)) between light and acoustic wave has to be fulfilled. A portion of the intensity across the whole spatially dispersed spectrum is reflected by the refractive grating as shown in Figure 4.1. Temporally modulating amplitude and phase of the acoustic wave allows for directly shaping of spectral components in amplitude and phase. However, as the acoustic wave is not static, the application is limited to pulsed systems with a repetition rate smaller than a few hundreds of kHz. The exact value depends on the dimensions of the AOM and the speed of sound inside the material. An advantage of this fact is that for every light pulse a new acoustic wave is sent through the AOM meaning that the shaping can be modified from shot to shot.

[1] Here the condition for the Bragg (thick grating) regime is shown as it is valid for the application. For thin gratings, i.e. short interaction region between medium and light, the AOM works in the Raman-Nath regime. For more details see [54, 128].

Property	Symbol	Value
Substrate material		UV grade fused silica
Maximum optical power density		100 W/mm^2
Carrier radio frequency	F	150 MHz
Bandwidth of the radio frequency	ΔF	50 MHz
Active aperture	H x L	1 mm x 20 mm
Optical transmission (from 260 to 488 nm)		98 %
Deflection (Bragg) angle	θ_B	0.12 °
Speed of sound	v_a	5960 m/s
Maximum RF power		2 W

Table 4.1: General specifications of AOM device provided by the manufacturer. Based on these values, further specifications and shaping limitations for the application of the AOM in the UV are derived later.

4.4 Implementation of the AOM in the UV

Based on the description of the working principle of an AOM, the AOM is implemented for shaping femtosecond pulses in the UV. The experimental realization of the set-up includes the optical and electronical configuration as well as the spectral calibration of the device.

4.4.1 Optical Configuration

At present time, there are two UV laser sources available within our research group, which should be combinable with the AOM. They are a second-harmonic and a sum-frequency mixing, two-stage NOPA, tunable between 250 nm to 300 nm and 300 nm to 350 nm, respectively. Both can generate sub 30-fs pulses with a spectral width of up to 7.5 nm (detailed information in [44]). Based on these perspectives, an AOM made from UV grade fused silica (FSD3-150-50-260 from Brimrose) and the other optical components for the set-up were chosen. The specifications of the AOM are listed in Table 4.1. The device is placed at the Fourier plane of a 4f set-up. Figure 4.2 shows a picture taken in the lab to give an impression of the AOM and the whole set-up. The 4f set-up consists of two

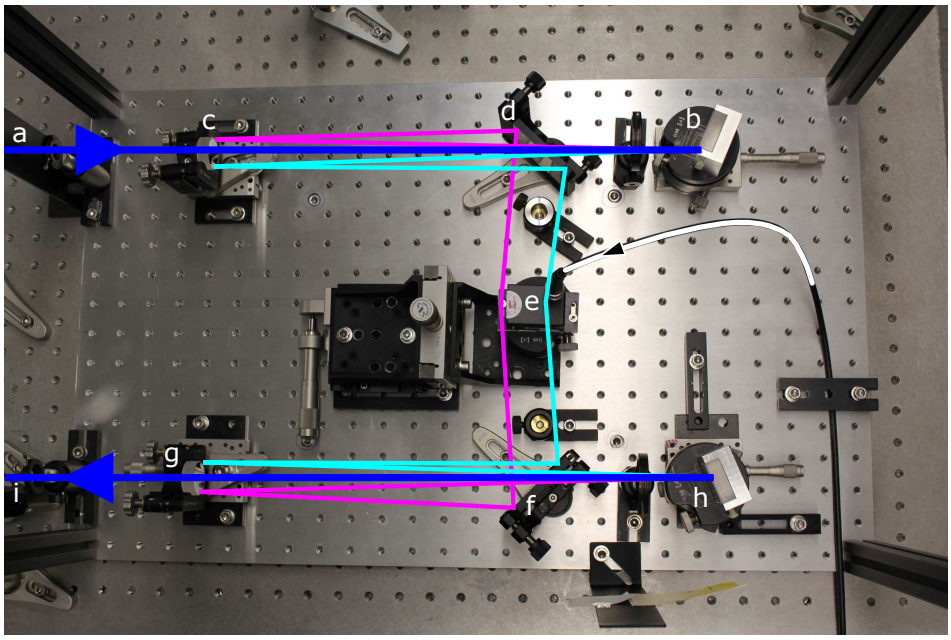

Figure 4.2: Picture of the AOM surrounded by the 4f set-up. The laser beam is coming from the left (a) and diffracted from the first grating (b). The spectrum is collimated in the horizontal axis and focused in the vertical direction by the first focusing mirror (c), after being reflected by the folding mirror (d), into the AOM (e). In the second half of the 4f set-up the ordering of the optical elements is reversed (folding mirror (f), focusing mirror (g), grating (h)). The beam leaves the 4f set-up on the left (i). The AOM is mounted with two translation stages and two rotational axis stages to allow for optimization the spatial overlap between the acoustic wave and the spatially dispersed laser beam. The RF waveform is transmitted to the piezo inside the AOM device via a coaxial cable. For clarity, the beam path between the two grating is indicated by only two spectral components and the undiffracted part of the beam is not shown.

gratings with 2400 grooves per mm and two spherical mirrors with a focal length of 375 mm. The number of grooves of the gratings as well as the focal length of the spherical mirror were chosen carefully to find a compromise in such a way that the same geometry can be used for the whole spectral range from 250 nm to 350 nm. For the choosen grating and mirror parameters, a spectral bandwidth of about $\Delta\lambda_{\mathrm{AOM}} = 21\,\mathrm{nm}$ illuminates the aperture of the AOM in this wavelength range. Two sets of mirrors and grating cover the spectral range with optimal diffraction and reflection efficiency. The gratings for less than 300 nm (150R from

RichardsonGratings) reflect more than 60 % from 200 to 285 nm. The gratings for wavelengths larger than 300 nm (430H from RichardsonGratings) have a reflectivity between 80 % and 90 % from 300 nm to 350 nm. The highly reflective focusing and folding mirrors guarantee a reflectivity of more than 97 % at their central wavelengths of 266 nm and 330 nm. All these values are given for light polarized parallel to the grooves of gratings, i.e. perpendicular to the direction of travel of the acoustic wave inside the AOM and to the optical table. Whenever the wavelength of the incoming laser pulses is changed from below to above 300 nm or vice versa, it is sufficient to exchange the optics, namely gratings and mirrors, in the 4f set-up.
As the light wave should be diffracted from the quasi-static grating inside the AOM, the incident angle of the light matches the Bragg angle, $\theta_B = 0.12°$ (cf. Bragg condition, (4.7)). As this angle is that small, it is sufficient to adjust the folding mirrors directly before and after the AOM to fulfill the Bragg condition and maintain the beam path after the 4f set-up.
The diffraction efficiency of the AOM itself depends critically on the polarization. It is optimal for light, which is polarized perpendicular to the propagation direction of the acoustic wave. The diffraction efficiency is typicall 70 % and 50 % at 260 nm and 330 nm, respectively. Experimental tests show that the diffraction efficiency of the AOM is reduced by a factor of six when the polarization is rotated by 90°. Summing up the efficiencies of all components in the 4f set-up, a total efficiency of 25 % and 30 % at 260 nm and 330 nm, respectively, can be achieved. However, these values are reduced further by aluminum mirrors, which are used to couple the 4f set-up into the beam path on the optical table. As the output of both available laser sources is about 1 µJ per pulse, the energy after the AOM is 250 nJ and 300 nJ at 260 and nm 330 nm, respectively. Further optical elements, which guide the beam from the 4f set-up to the sample, cause a further decrease of the energy available for experiments with shaped pulses.

4.4.2 Electronical Configuration

A schematic view of the electronical set-up is shown in Figure 4.3. The radio frequency (RF) signal for the acoustic wave is generated by an arbitrary waveform

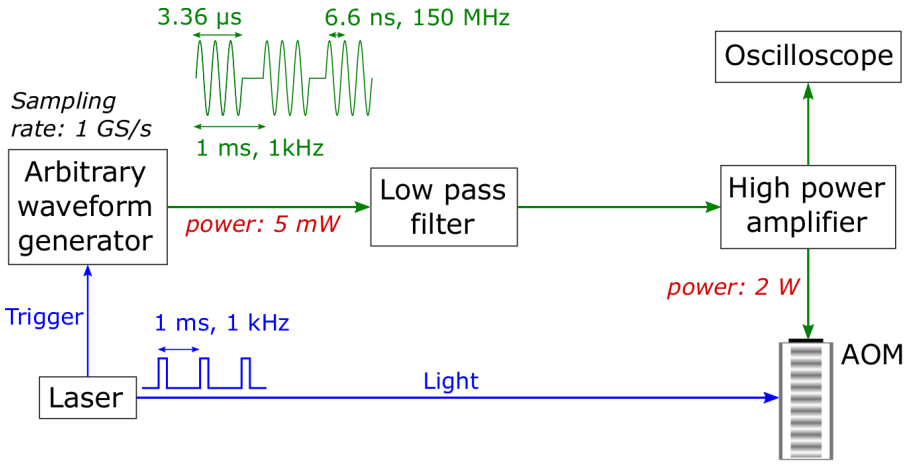

Figure 4.3: Schematic of the electronics to control the AOM, including the synchronization with the laser. The AWG generates a RF waveform with a carrier radio frequency of 150 MHz over 3.36 µs. This signal passes a low pass filter to clean up high-frequency artifacts. In the high power amplifier, the signal of 5 mW is amplified to 2 W to drive the AOM. Finally, the RF waveform is transduced as an acoustic wave inside the AOM by a piezo element attached to the AOM crystal. As the laser triggers the AWG, the waveform is generated with a 1 kHz repetition rate. Subsequently, the acoustic wave and the laser light arrive synchronously inside the AOM.

generator (arbitrary waveform generator card, DA11000, from Acquitec)). This electric signal passes through a low pass filter (SLP-250 from Mini-Circuits) to clean up high-frequency artifacts from the waveform generation process. Radio frequencies higher than 250 MHz are attenuated by more than 3 dB. Next, the RF signal is amplified in a high power amplifier (ZHL-03-5WF+ from Mini-Circuits) to an output power of 2 W. This is the maximum power the AOM can be driven with. The amplified RF signal is then directly transferred by a piezo transducer to the AOM to create the quasistatic grating inside the AOM. An oscilloscope allows monitoring the RF waveform simultaneously. The length of cables between the devices is kept as short as possible to minimize attenuation and reflections of the RF signal. The output of the AWG is triggered by the laser to ensure that the RF waveform and the light pulse are synchronized and arrive at the same time inside the AOM.

Generation of the Waveform

The RF signal is generated with 1 GS/s and a vertical resolution of 12 bit. It can be described by a time-dependent waveform, $w(t)$,

$$w(t) = A \sin(2\pi F t), \tag{4.9}$$

where the central radio frequency $F = 150\,\text{MHz}$ (see Table 4.1) is chosen according to the AOM material. The variable A is the magnitude of the waveform, which has to be chosen carefully to not exceed the maximum RF power of 2 W after the amplification. This RF waveform is generated about a certain time range, ΔT, to create a quasistatic grating across the whole aperture of length, L. The corresponding time range of this RF waveform, also called time window[2], is given by

$$\begin{aligned} \Delta T &= \frac{L}{v_a} \\ &= 3.36\,\mu\text{s}, \end{aligned} \tag{4.10}$$

with $L = 20\,\text{mm}$ and $v_a = 5960\,\text{m/s}$, see Table 4.1. The RF waveform is generated by the AWG discretely with a sampling rate $f_s = 1\,\text{GHz}$. Therefore, the continuous variable t in Eqn. (4.10) is replaced by $f_s \cdot j$, where the sample index, j, is introduced as a discrete temporal parameter, running from 1 to 3360 to cover the whole time window of 3.36 µs. $w(j)$ consists of 3360 points like j. So far, the RF waveform was described in the temporal domain, i.e. j corresponds to the temporal position within the RF waveform. Simultaneously, j defines a spatial position of the quasistatic grating within the AOM. As the spectrally dispersed light pulse is diffracted from this grating, a synchronization between RF waveform and light pulse as well as a spectral calibration (see Section 4.4.3) are required to assign a specific wavelength component to every j.
For phase shaping of a laser pulse by use of an AOM, the desired spectral phase, $\phi(j)$, is introduced as an additional argument in the sinusoidal function. It is a vector, which has a length of 3360. This can be interpreted as a locally introduced phase shift of the radio frequency or as a modulation of the radio frequency.

[2] In principle, ΔT limits the maximum repetition rate of pulses, which can be individually shaped, to $1/\Delta T \approx 300$ kHz. This rate is more than two orders of magnitude larger than the 1 kHz rate of the utilized laser system and, therefore, it is no limiting factor at all.

Additionally, amplitude shaping is realized by replacing the constant magnitude A by a vector $A(j)$ of length 3360. The resulting RF waveform $w(j)$ has the form

$$w(j) = A(j)\sin\left(2\pi F f_s j + \phi(j)\right). \tag{4.11}$$

Although $A(j)$ and $\phi(j)$ both have 3360 entries, their values cannot be chosen arbitrarily. A qualitative explanation is that one period within the RF waveform lasts about 6.6 ns ($\approx 1/F = 150$ MHz) and, therefore, it is generated by 6 to 7 discrete adjacent points of the RF waveform, $w(j)$. This central radio frequency could be completely changed by arbitrarily choosing $A(j)$ and $\phi(j)$. For this reason, there have to be limitation for these two variables. The limitations are given by L and the bandwidth of the radio frequency, ΔF. The minimum and maximum radio frequency, which is supported by the AOM material, is given by the RF bandwidth $\Delta F = 50$ MHz (see Table 4.1), corresponding to a range from 125 MHz to 175 MHz. The bandwidth is an intrinsic property of the AOM material and it is limited by the attenuation of the acoustic wave inside the material. The limitations on $A(j)$ and $\phi(j)$ can be expressed by the product of ΔF and ΔT. This value is called number of features, N_{fea} with

$$\begin{aligned} N_{fea} &= \Delta T \Delta F \\ &= 168. \end{aligned} \tag{4.12}$$

$N_{fea} = 168$ can be interpreted that 168 different values within $A(j)$ and $\phi(j)$ can be chosen to shape a femtosecond pulse, whose spectral width covers the whole aperture of the AOM. All other entries of $A(j)$ and $\phi(j)$ are interpolated and a single feature consists of $3360/168 = 20$ adjacent points within the waveform. The term number of features is an analogue to pixel for shaping devices as the LCM, where discrete values for A and ϕ are applied to the single spectral components covering the pixels.

4.4.3 Spectral Calibration

For the spectral calibration, an amplitude vector is generated, where only a few tens of adjacent entries of $A(j)$ are not zero (Figure 4.4). The corresponding wave-

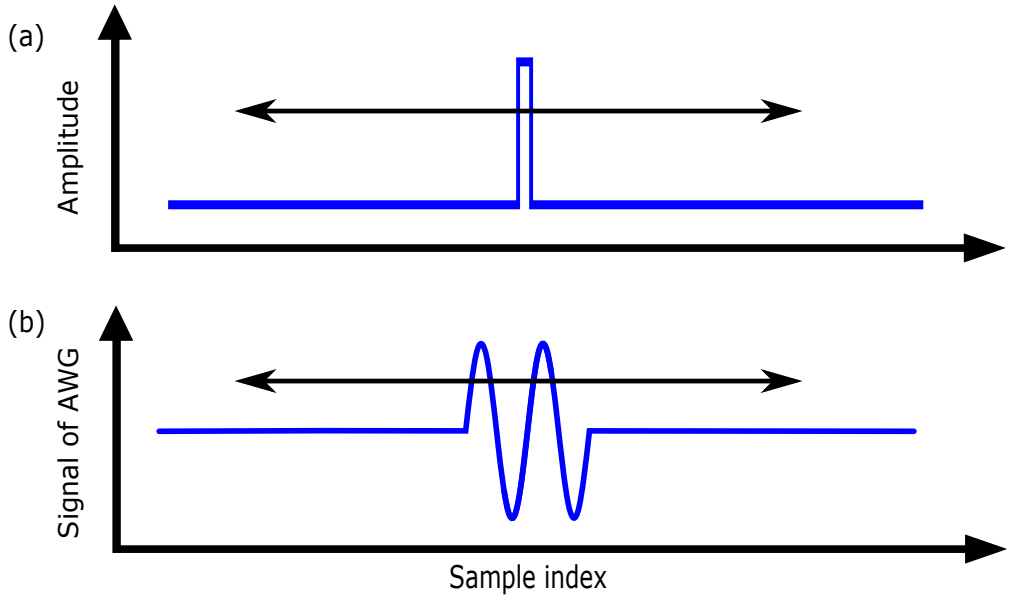

Figure 4.4: (a) The amplitude of only a few tens of sample indices is set to a value larger than zero. (b) Therefore, the AWG generates a waveform, which consists of only a few periods corresponding to a spatially narrow diffraction grating. Moving the position across the sample index allow calibrating the AOM (see Figure 4.5).

form consists of only a few periods. Therefore, only a spatially narrow diffraction grating is generated inside the AOM. Consequently, only a small spectral part is diffracted, which is recorded by the spectrometer (AvaSpec-ULS3648-USB2 from Avantes) for the calibration. The position of the peak, i.e. its sample index, is varied across the RF waveform. The spectra of the diffracted light for various positions are plotted in Figure 4.5(a). The wavelengths of the maximum in each spectrum is plotted versus the corresponding sample index (Figure 4.5(b)). A linear fit with a slope of $(6.28 \pm 0.05)\,\mathrm{pm/ns}$[3] gives the relation between the position in the RF waveform and wavelength over the whole shaping window.

The spectral bandwidth covering one feature, $\Delta\lambda_{\mathrm{fea}}$ can be calculated by use of the slope as one feature consists of 20 points within the RF waveform. Alternatively, it can be approximated from spectral bandwidth of $\Delta\lambda_{\mathrm{AOM}} = 21\,\mathrm{nm}$,

[3]The unit of ns on the x-axis is chosen in accordance to the sampling rate of 1 GHz of the AWG.

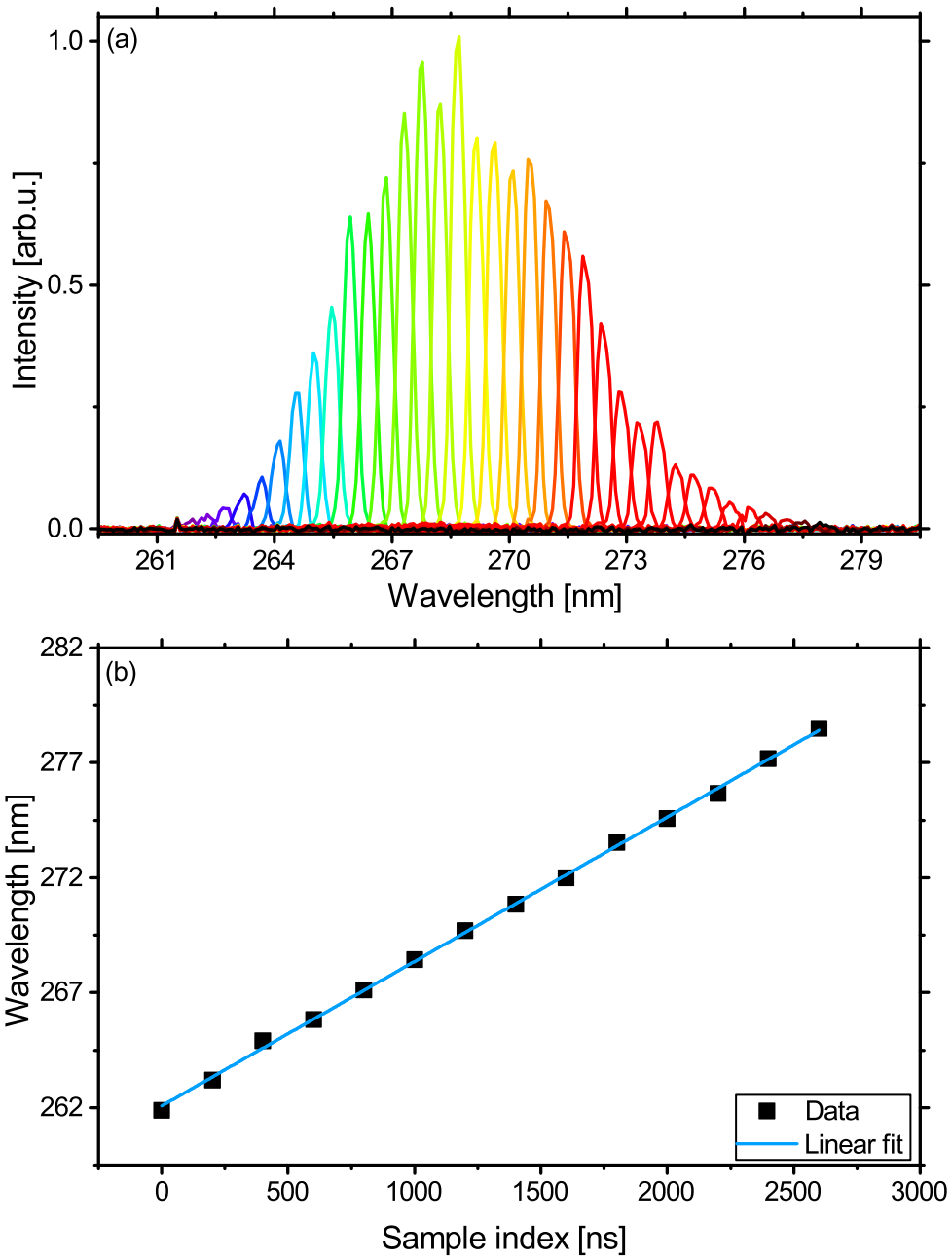

Figure 4.5: (a) Diffracted spectrum for δ peak-like waveforms at different positions in the waveform. (b) Peak wavelength versus position in the waveform for spectral calibration. The slope is (6.28 ± 0.05) pm/ns, indicating the spectral separation corresponding to adjacent points within the waveform.

which illuminates the aperture of the AOM, and the number of features across the AOM, $N_{fea} = 168$. Therefore, the bandwidth of one feature, $\Delta\lambda_{fea}$, is typically

$$\begin{aligned} \Delta\lambda_{fea} &= \frac{\Delta\lambda_{AOM}}{N_{fea}} \\ &= 0.125\,\text{nm}. \end{aligned} \tag{4.13}$$

4.5 Characterization of the AOM

After the general implementation of the AOM, its shaping performance is discussed in the following, starting with the attenuation of the acoustic wave.

4.5.1 Attenuation of the Acoustic Wave

The carrier radio frequency of the acoustic wave is a property of the material due to its intrinsic structure. Inside the material, the acoustic wave is attenuated due absorption and scattering phenomena [129]. The attenuation increases for acoustic waves, whose carrier radio frequency deviates of the characteristic carrier radio frequency. This attenuation is the limiting factor for the range of radio frequencies, which are transmitted through the AOM, and it defines the RF bandwidth of the device.
As the diffraction efficiency R is proportional to the intensity of the acoustic wave, I_a, the attenuation behavior can be characterized via the intensity of the diffracted light. The intensity of the diffracted light is measured while the radio frequency is varied to characterize the attenuation of the acoustic wave in dependence on the radio frequency. In addition, the RF signal is monitored simultaneously, as its peak-to-peak value varies with the radio frequency. In Figure 4.6, the light intensity and voltage of the AWG are plotted versus radio frequency. On top of that, the data are corrected for the changes in voltage, i.e. light intensity divided by peak-to-peak voltage squared. The attenuation curve is not perfectly symmetric around 150 MHz. However, the efficiency decreases by a factor of three at 125 MHz and 175 MHz with respect to 150 MHz, which is

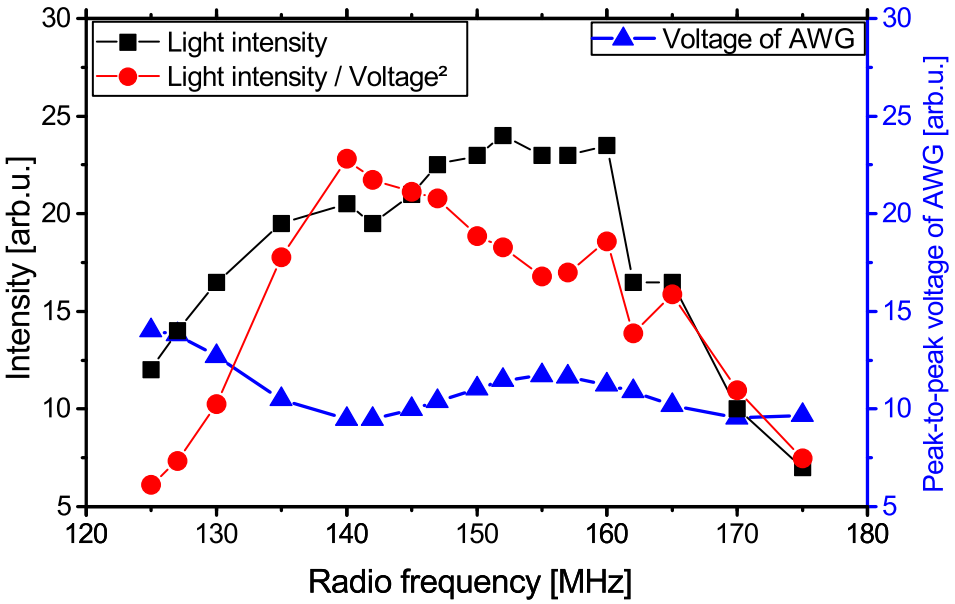

Figure 4.6: Attenuation of the acoustic wave inside the AOM. The attenuation is determined by measuring the diffractive light (black). As the efficiency depends quadratically on the power of the RF waveform, it is corrected by the actual power output (blue) of the AWG (result shown in red). The efficiency decreases by a factor of three, which is in accordance to the data sheet of the manufacturer.

in accordance to the data sheet of the manufacturer.
This method actually determines the attenuation of the diffraction efficiency. It is mainly determined by the attenuation of the acoustic wave inside the material. On top of this, changing F also modifies the Bragg condition as θ_B depends on F. However, the measurement was performed under realistic conditions as θ_B is a constant for the shaping.
With further measurements at $F = 150\,\mathrm{MHz}$, a significant attenuation of the acoustic wave across the aperture of the AOM could be excluded.

4.5.2 Amplitude Shaping

Amplitude shaping corresponds to a variation of the intensity of the RF waveform. To verify the correct amplitude shaping, the amplitude of the RF waveform

is tuned between 0.1 and 0.7 and the spectrum of the diffracted light is measured[4] (Figure 4.7(a)). The RF amplitude as well as the spectral intensity at 263.5 nm are logarithmized and plotted verses each other (Figure 4.7(b)). A linear fit for amplitudes from 0.25 to 0.7 has a slope of 2.19±0.08 verifies the quadratic dependence of the diffraction efficiency on the amplitude of the acoustic wave (cf. Eqn. (4.8)).

4.5.3 Phase Shaping

To realize phase shaping with the AOM, a phase term is added to the carrier radio frequency of the waveform (cf. Eqn. (4.11)). To characterize the phase shaping, linearly chirped pulses and multipulse are generated and their autocorrelation traces are measured. For a deeper understanding of the shaping effects on the RF waveform, the Fourier transform (FT) of the RF waveform is determined. The reference is an unshaped pulse with a constant phase and amplitude along the whole RF waveform. Its FT shows a sharp peak at 150 MHz, where the width is limited by the length and the sampling rate of the RF waveform.

Linear Chirp

The phase $\phi(\omega)$ for linear chirp has the form

$$\phi(\omega) = \frac{1}{2}\phi''(\omega - \omega_{cen})^2 \tag{4.14}$$

(cf. Eqn. (2.2)). A pulse of 40 fs is elongated to 60 fs and 70 fs due to linear chirp of -700 fs^2 and 800 fs^2, respectively. The corresponding autocorrelation traces are plotted in Figure 4.8. Additionally, The FT of the RF waveform for a linearly chirped pulse ($\phi'' = 800\,fs^2$) is determined (Figure 4.9). It shows a clear broadening of the peak, which can be interpreted as a change of the radio frequency along the waveform.

[4] The maximum amplitude, which is applied to the AWG, is 0.7 to limit the output power of the amplifier driving the AOM to 2 W.

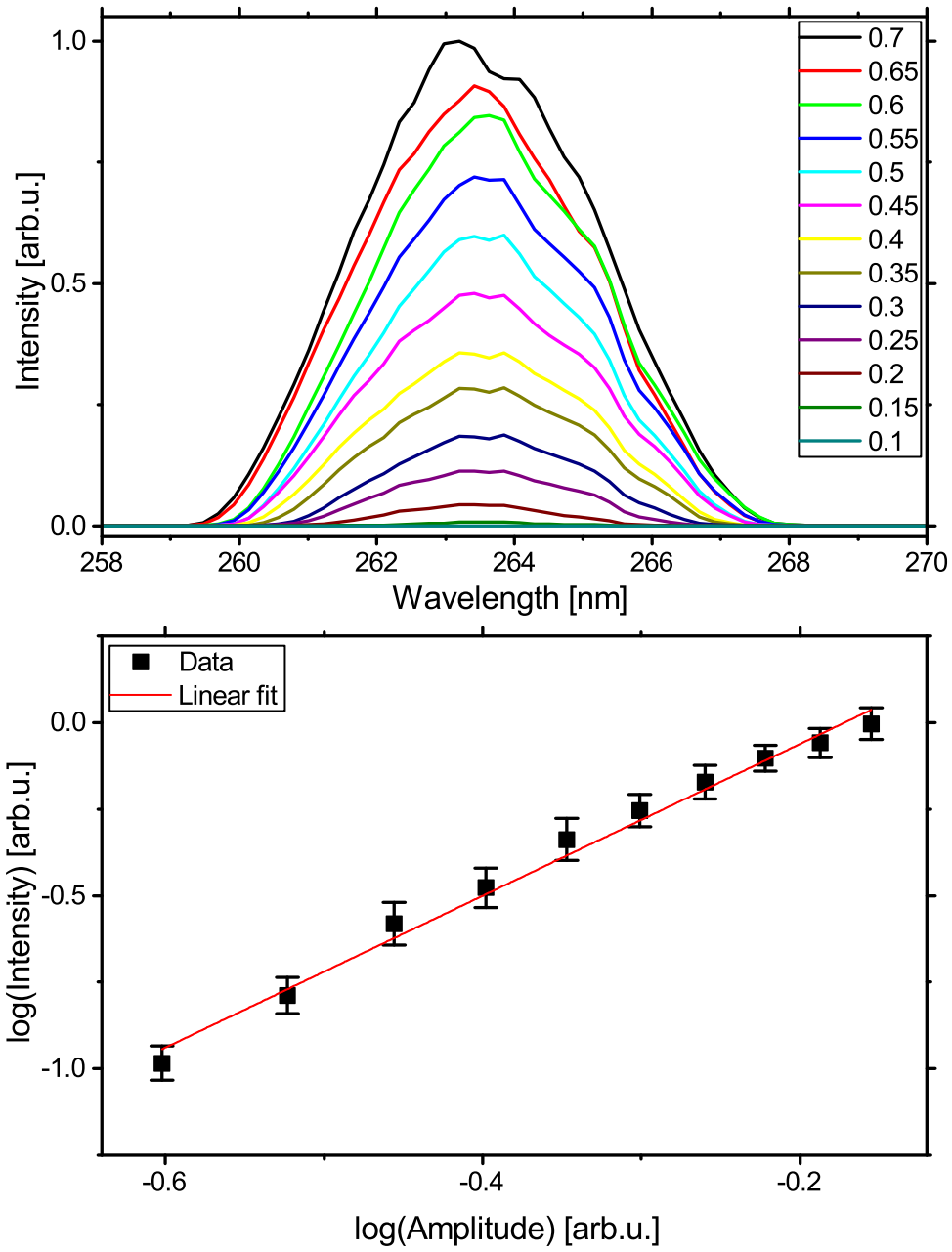

Figure 4.7: (a)Spectra of diffracted light for amplitude values between 0.1 and 0.7. The latter is the maximum amplitude that can be applied without damaging the AOM. (b) The spectral intensity versus the set value for the amplitude on a log-log scale. A linear fit for amplitudes from 0.25 to 0.7 verifies the quadratic dependence as the slope is 2.19±0.08.

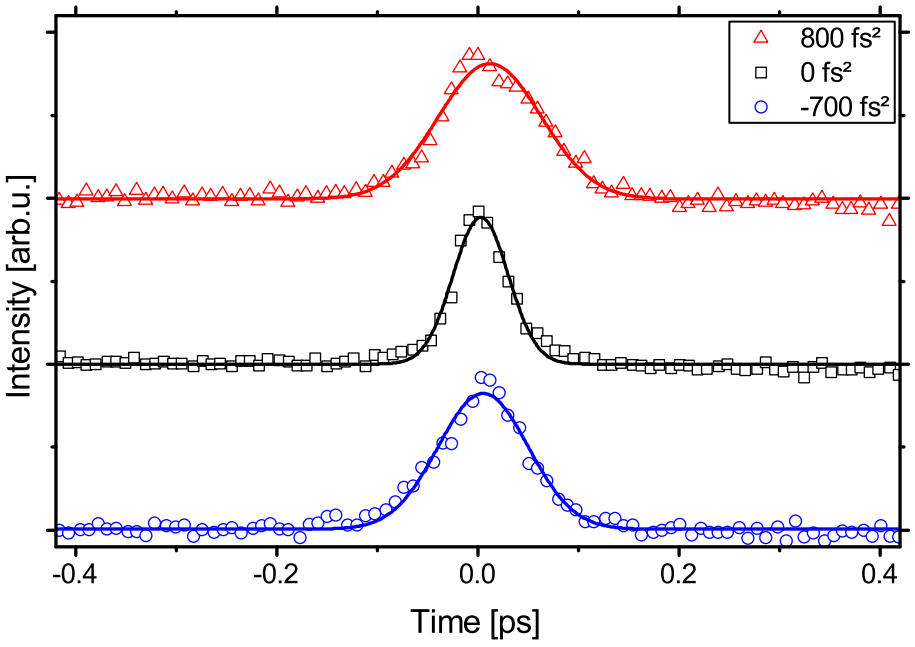

Figure 4.8: Autocorrelation traces of chirped pulses with several interpulse distances as indicated by the legend. The single traces are individually fitted with a Gaussian. The resulting pulse durations are 40 fs (for 0 fs^2), 60 fs (for -700 fs^2) and 70 fs (for 800 fs^2).

Multipulse

Multipulses are generated with the AOM by adding a phase term of the form

$$\phi(\omega) = a \sin(b(\omega - \omega_{cen}) + c) \tag{4.15}$$

(cf. Eqn. (2.4)). The autocorrelation traces for different values of b and constant $a = 1.23$ and $c = 0$ are plotted in Figure 4.10. The correct interpulse spacing indicates the sufficient performance of the AOM. The asymmetry for positive and negative chirp seen in Figure 4.8 as well as for the multipulse in Figure 4.10 is due to space-time coupling on split mirror autocorrelation measurements, which was studied in detail for this autocorrelator set-up previously [118].

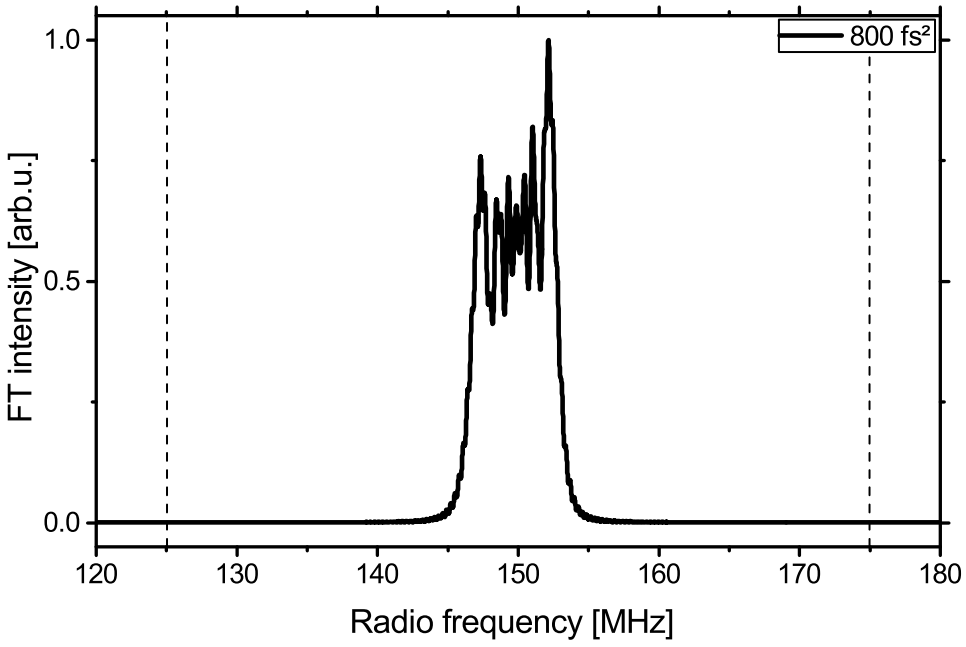

Figure 4.9: FT of the RF waveform for a linearly chirped pulse ($\phi'' = 800 fs^2$).

4.5.4 Double Pulses

While chirped pulses and multipulses can be realized by phase shaping, the generation of identical double pulses requires additional amplitude shaping. A double pulse consisting of two identical replicas at time $t = 0$ and $t = \tau$ can be mathematically expressed by

$$M(\omega) = \frac{1}{2}\{1 + \exp[i(\omega - \omega_{cen})\tau]\}. \tag{4.16}$$

This expression can be rearranged to a mask function

$$M(\omega) = \cos\left(\frac{\omega - \omega_{cen}}{2}\tau\right) \exp\left(i\frac{\omega - \omega_{cen}}{2}\tau\right), \tag{4.17}$$

where spectral phase and amplitude can be directly identified as

$$\phi(\omega) = \frac{\omega - \omega_{cen}}{2}\tau \tag{4.18}$$

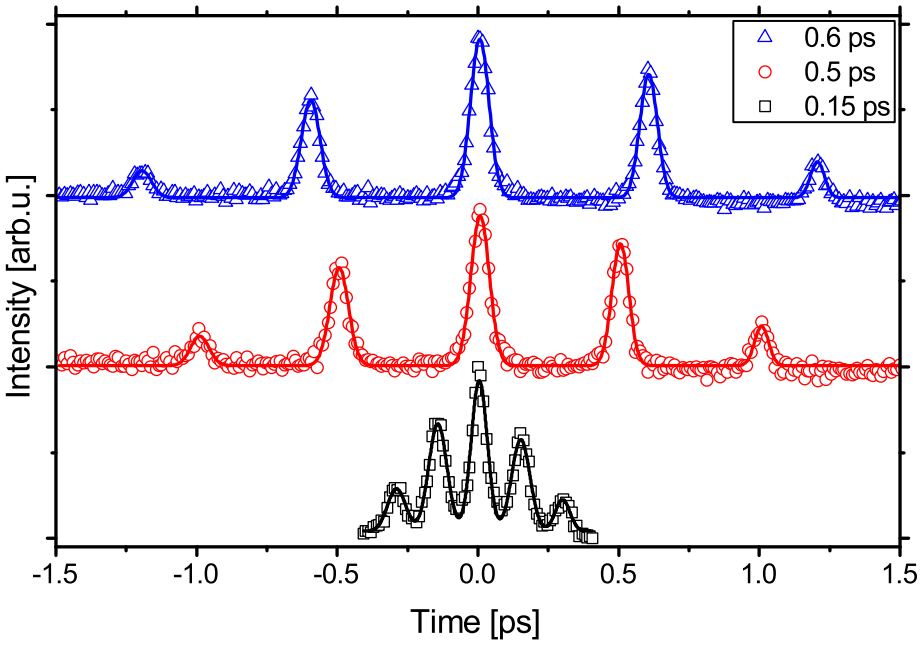

Figure 4.10: Autocorrelation traces of multipulses with several interpulse distances as indicated by the legend. In all cases, the parameters a and c are set to $a = 1.23$ and $c = 0$. For $b = 0.15$ ps the spatial range of the delay stage of the autocorrelator is reduced to improve the temporal resolution. For this reason the temporal window is limited.

and

$$A(\omega) = \cos\left(\frac{\omega - \omega_{cen}}{2}\tau\right). \tag{4.19}$$

The phase term given in Eqn. (4.18) corresponds to a first order Taylor term (cf. Eqn. (2.2)), which causes a temporal delay of the shaped pulse. Eqn. (4.19) implies that the amplitude shaping of a double pulse reduces the total energy of the shaped output by a factor of two as the diffraction efficiency scales with the squared amplitude (c.f. Eqn. (4.8) and Figure 4.7(b)).

An alternative mask function to generate a double pulse (also including amplitude shaping) with two replicas at $t = \pm\tau/2$ can be found in Ref. [130].
In contrast, a two-color double pulse only demands phase shaping. For example, when Eqn. (4.18) is applied for $\omega < \omega_{cen}$ and $\phi(\omega) = 0$ for $\omega > \omega_{cen}$ (or vice versa), one half of the spectrum is delayed.

Various double pulses were generated with the AOM. The shaped spectra were measured with the spectrometer (Figure 4.11(a)). The autocorrelation traces in Figure 4.11(b) show the temporal distribution of the pulses. Eqn. (4.19) implies that for increasing τ, i.e. the temporal spacing between the subpulses, the period of the function $A(\omega)$ decreases. This can be directly seen in Figure 4.11. For $\tau = 1\,\mathrm{ps}$, the fringes in the spectrum are closely spaced. For $\tau = 0.25\,\mathrm{ps}$, the fringes are more far apart from each other. The maximum delay of 3 ps of the autocorrelator and the resolution of the spectrometer (0.1 nm) limit the interpulse distance of a multipulse, which can be acquired. The limitation of the AOM on the double pulse is presented in the next section.

4.5.5 Shaping Limitations

The properties of the AOM and its application in the UV limit the parameter space for shaping. In the following, restrictions for linearly chirped, multi- and double pulse are discussed. As these limitations depend on the central wavelength of the shaped pulse, two characteristic values at the wavelengths of 260 nm and 330 nm for the two UV laser sources are given.
For pixelated devices as the LCM, Nyquist-Shannon sampling theorem limits the maximum change in phase for adjacent pixels. The theorem dictates that the relative phase shift between two adjacent features has to be smaller than π to prevent aliasing (e.g. [94]). The AOM is not pixelated, but as shown previously, the bandwidth of the RF waveform restricts the maximum number of independently shaped features. Therefore, it seems to be reasonable to apply the Nyquist-Shannon sampling theorem also to these features to estimate the shaping limitations. The theorem is written as

$$\phi(\omega_{\mathrm{fea(n)}}) - \phi(\omega_{\mathrm{fea(n\text{-}1)}}) \leqslant \pi, \tag{4.20}$$

where n is the index of the feature. At this point, it is crucial to remember adjacent features are not adjacent points of the RF waveform.

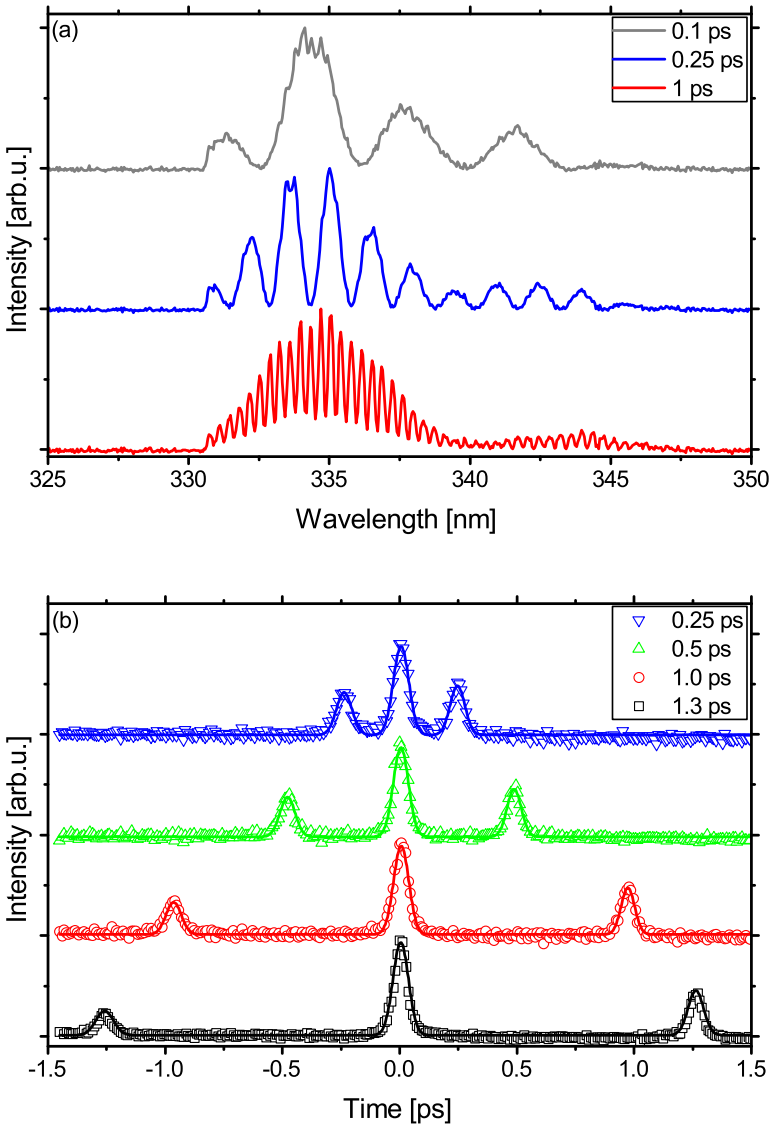

Figure 4.11: (a) Spectra of double pulses with several interpulse distances τ as indicated by the legend. The resolution of the spectrometer (0.1 nm) restricts contrast for large values of τ, i.e. small period. (b) Autocorrelation traces of double pulses with varying interpulse distances as indicated by the legend. The maximum delay, which can be measured is limited by the range of the piezo inside the autocorrelator set-up. An increase of the temporal interpulse separation leads to a decreased separation of the peaks in the spectrum (cf. Eqn. 4.19).

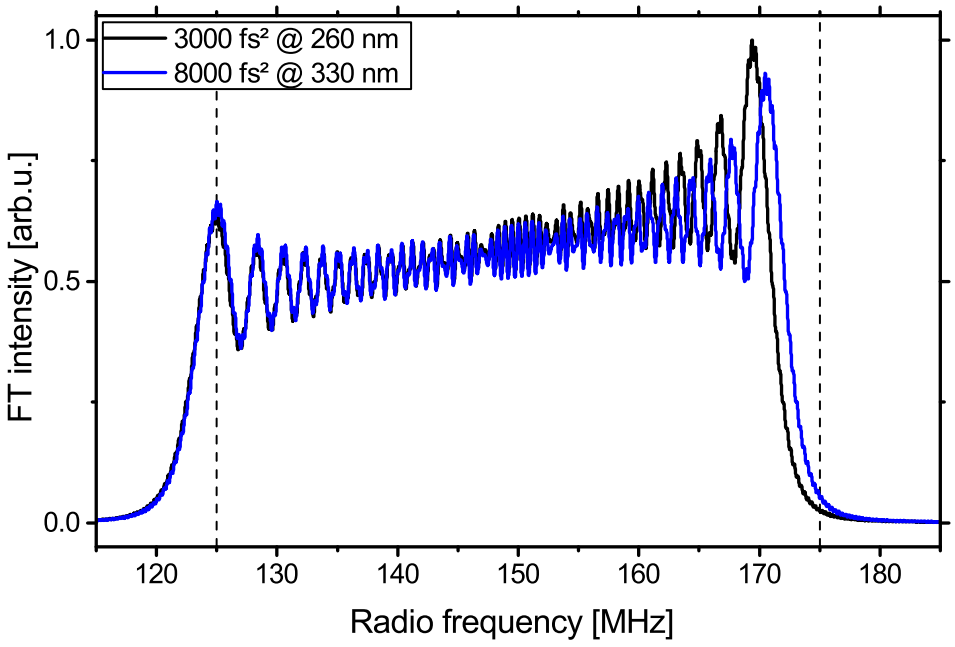

Figure 4.12: FT of the RF waveform for shaping masks with linear chirp of $\phi'' = 3000\,\mathrm{fs}^2$ at 260 nm and $\phi'' = 8000\,\mathrm{fs}^2$ at 330 nm. As the outermost peaks of both curves are at the bandwidth edge of 125 MHz, these values are the maximum chirps, which can be generated with the AOM

Maximum Chirp

In the case of linear chirp, Eqn. (4.14) is inserted into Eqn. (4.20).

$$\frac{1}{2}\phi''\left[(\omega_{\mathrm{fea(n)}}-\omega_{\mathrm{cen}})^2-(\omega_{\mathrm{fea(n\text{-}1)}}-\omega_{\mathrm{cen}})^2\right]\leqslant\pi. \tag{4.21}$$

Resolving this equation for ϕ'' gives the upper limit for the linear chirp, ϕ''_{max}.

$$\phi''_{\mathrm{max}}=\frac{2\pi}{|(\omega_{\mathrm{fea(n)}}-\omega_{\mathrm{cen}})^2-(\omega_{\mathrm{fea(n\text{-}1)}}-\omega_{\mathrm{cen}})^2|}. \tag{4.22}$$

ϕ''_{max} depends on the two frequencies $\omega_{\mathrm{fea(n)}}$ and $\omega_{\mathrm{fea(n\text{-}1)}}$ as well as on the central frequency ω_{cen}. For a conservative estimation, the frequencies are chosen from the edge of the AOM. The resultant maximum values are calculated to be $2600\,\mathrm{fs}^2$ and $6900\,\mathrm{fs}^2$ for 260 nm and 330 nm, respectively. To check if the

whole RF bandwidth of the AOM is exhausted for this estimation, the FT of the RF waveforms, when such a linear chirp is applied, is determined. The FT shows a peak at the low end of the FT spectrum is at 128 MHz for both central wavelengths. It means that this simple approach underestimates the maximum chirp and that Eqn. (4.20) only provides an approximation for the shaping limit, especially for the AOM, which is not pixelated. Furthermore, the tool of the FT allows for determining the actual maximum chirp. To shift the peak to the bandwidth edge, 125 MHz, chirp values of even 3000 fs^2 and 8000 fs^2 for 260 nm and 330 nm, respectively, can be applied as shown in Figure 4.12. The plot shows that only the lower RF bandwidth limit at 125 MHz is hit but not the one at 175 MHz. This in principle allows for pushing these values even further by shifting the carrier radio frequency to higher values than 150 MHz.

Maximum Delay for Double and Multipulses

As shown previously, the double pulse is generated by a combination of sinusoidal amplitude shaping and phase shaping, which causes a temporal delay. The general expression for the phase $\phi(\omega)$ of a pulse with delay, b_1, is given by

$$\phi(\omega) = b_1(\omega - \omega_{cen}). \tag{4.23}$$

Inserting this expression into Eqn. (4.20), results in

$$\begin{aligned} b_1\left(\omega_{fea(n)} - \omega_{fea(n\text{-}1)}\right) &= b_1 \Delta\omega_{fea} \\ &\leqslant \pi, \end{aligned} \tag{4.24}$$

where $\Delta\omega_{fea} = \omega_{fea(n)} - \omega_{fea(n\text{-}1)}$. This allows to calculate the maximum delay to be

$$b_{1,max} = \frac{\pi}{\Delta\omega_{fea}}. \tag{4.25}$$

However, as the double pulse requires an additional amplitude shaping with the period of $\frac{\tau}{2}$, the maximum delay of the double pulse, τ_{max}, is only half the value given in Eqn. (4.25):

$$\begin{aligned}\tau_{max} &= \frac{b_{1,max}}{2} \\ &= \frac{\pi}{\Delta\omega_{fea}}.\end{aligned} \tag{4.26}$$

In the UV, the spectral width of one feature, $\Delta\omega_{fea}$, can be approximated by

$$\Delta\omega_{fea} \approx \frac{\Delta\omega_{AOM}}{N_{fea}}. \tag{4.27}$$

Thus, Eqn. (4.26) can be rewritten to

$$\begin{aligned}\tau_{max} &= \frac{\pi N_{fea}}{\Delta\omega_{AOM}} \\ &= \frac{N_{fea}\lambda_{cen}^2}{2c\Delta\lambda_{AOM}}.\end{aligned} \tag{4.28}$$

In the second step, the relation ship

$$\Delta\omega = 2\pi c\frac{\Delta\lambda}{\lambda_{cen}^2} \tag{4.29}$$

is used, where λ_{cen} is the central wavelength and c is the speed of light. The maximum delay of a double pulse is calculated to be 0.9 ps and 1.5 ps for central wavelengths of 260 nm and 330 nm, respectively. To verify τ_{max}, the RF waveform is generated for a double pulse with $\tau = \tau_{max}$ and its FT is determined (Figure 4.13). The latter shows a second peak, which is centered around the bandwidth edge, 125 MHz.

The approximation of the shaping limit fits for the double pulse. Therefore, it seems to be justifiable to expand the range of linear chirp to higher and lower values until the outermost peak in the FT spectrum also reaches the bandwidth edge, even if they exceed the calculated values.

Furthermore, Eqn. (4.28) can be applied to any other multiple pulse sequence. or a triple pulse the maximum delay is half, i.e. 0.45 ps and 0.75 ps for a central wavelength of 260 nm and 330 nm, respectively. .

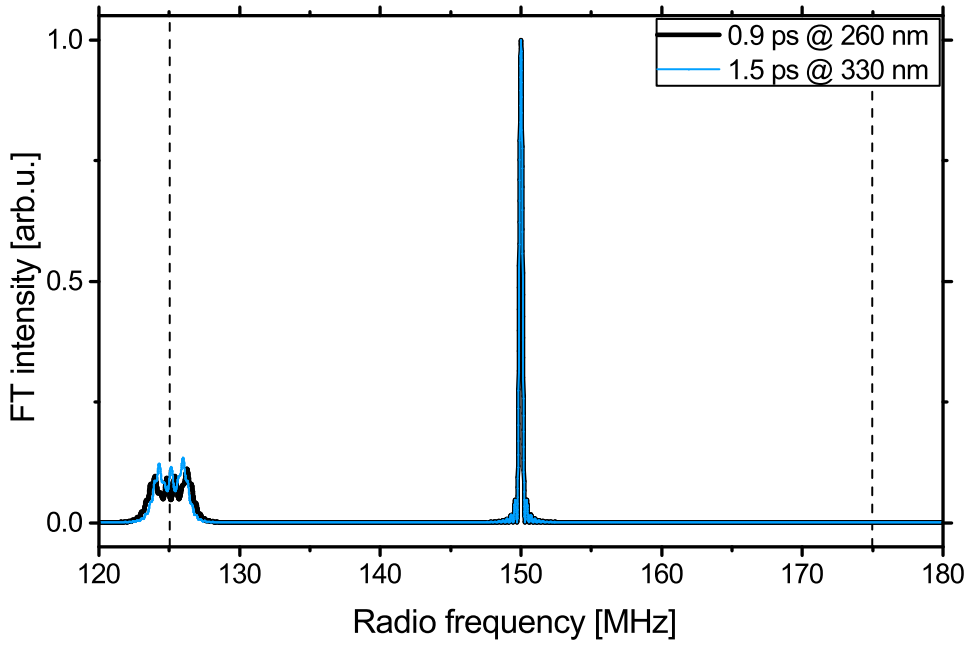

Figure 4.13: FT of the RF waveform for the shaping mask for double pulses with maximum interpulse delay of $\tau = 0.9$ fs (at 260 nm) and $\tau = 1.5$ fs (at 330 nm).

The maximum values given here refer to situations where only one type of shaping is applied. The values reduce in presence of chirp to compress the pulse initially or when a combination of phases is applied.

4.6 Comparison of the AOM-Based UV Shaper with Other Devices

In the following, various properties are compared for several shaping devices in the UV, which were described in Section 4.2. The values are summarized for all devices in Table 4.2. The AOM-based set-up, which was developed in the scope of this work, is called AOM 1 to distinguish it from T. Weinacht's set-up, which is called AOM 2. Furthermore, the comparison includes the AOPDF, the MEMS, which was used earlier in our research group, the UV-LCM and two schemes

of indirect shaping. Two examples are chosen for the indirect shaping to show the effort, which was made during the last years in this field. Both of them were developed within five years. However, there were essential improvements from Ref. [28] to Ref. [125]: after the concept was proven for 150 fs pulses, it was applied to sub-20 fs pulses.
The UV laser source determines the central wavelength of the shaped pulse and it also is taken into consideration for the design of the shaping set-up, which determines its shaping window. The UV-LCM, AOM 2 and one of the indirect shaping set-ups are used to shape the second, third and forth harmonic of a Ti:sapphire amplifier system, respectively. Therefore, their central wavelength is fixed. In contrast, the devices AOM 1, AOPDF, MEMS and the second indirect shaping set-up are used to shape the sum frequency or second harmonic signal of visible NOPAs. As a consequence, they cover a whole wavelength range over several tens of nm and the spectral width of the UV pulses is broader than for the harmonics mentioned earlier. The shaping window of the AOPDF is extremely large. It can be a clear advantage for the shaping of laser pulses with such a broad bandwidth.
The diffraction efficiency of AOM 1 is with 70 % lower than the corresponding values for AOM 2, MEMS and UV-LCM. Nevertheless, the choice of gratings and mirrors compensates this and the best output efficiency, 30 %, out of all devices is achieved. It should be noted that the output efficiency of the AOPDF is comparable to the values given here for the other devices. This is surprising as the AOPDF is the only device, which does not require a 4f set-up with further losses due to gratings and mirrors. The energy of the shaped pulses depends on two parameters. First, the shaping efficiency of the fundamental light field in the visible or near-infrared and second, the conversion efficiency in the nonlinear crystal into the UV are crucial. However, the latter is an essential parameter for the generation of UV pulses in general.
In principle, all presented devices can modulate the phase and amplitude of the pulses. In Ref. [127], only phase modulation is mentioned for the UV-LCM. However, it is a technical aspect if one or two LC displays are installed and it can be expected that the next generation of UV-LCMs will provide the possibility of combined phase and amplitude shaping. The underlying concepts of the UV-LCM and of indirect shaping allow one to choose between amplitude

shaping and polarization shaping, which was already realized in the past by indirect shaping [131, 132]. The reflective device MEMS is not sensitive to the polarization of the light, which directly excludes polarization shaping. In contrast, the diffraction efficiency of the two acousto-optic devices, AOM and AOPDF, is polarization dependent. However, they intrinsically do not offer the option of polarization shaping.

The number of pixels or features varies between the devices by more than a factor of four. The UV-LCM provides the highest number, 648. Furthermore, it and the MEMS, they are both two dimensional. Therefore, it is possible to shape a single spectral components in two or even more different ways simultaneously. This option has been used for example for a shaper-assisted cross correlator [45]. The number of features of the AOM in contrast is limited to less than 200. It is mainly restricted by the length of the device and the attenuation of the acoustic wave as discussed in Section 4.5.1. Nevertheless, the advantage of AOM and AOPDF is that the shaping mask is generated by a continuous RF waveform and it is not pixelated. Such a pixelation causes artifact in the pulse shape (e.g. Ref. [28] in the UV), which can disturb the application of shaped pulses.

To compare the shaping performance based on a concrete pulse shape, the maximum delay of a double pulse, τ_{max}, is calculated for all devices. Despite the central wavelength, the shaping window and the number of pixels or features determine τ_{max} (Eqn. (4.28)). Compared to the other devices, τ_{max} for AOM 1 is the smallest value. Nevertheless, in none of the references for the other shaping devices, the temporal shaping exceeds a time window of $\pm 1.5\,\mathrm{ps}$. Therefore, it can be assumed that for most applications, τ_{max} is not a limiting factor.

As a last point, the update rate of the shaping devices is compared. All these devices in the UV are used to shape pulses of a laser system with a repetition rate of 1 kHz. Therefore, the static shaping mask of the UV-LCM and for indirect shaping does not bring any advantage, but it rather decreases the update rate between different shaping masks. The micro mirrors of a MEMS cannot be deflected statically but their duty cycle is typically 5 %. Nevertheless, the update rate for the application of a MEMS with a 1 kHz laser system was optimized to 0.3 kHz [43], corresponding to a 33 % duty cycle in combination with a 1 kHz laser system. In contrast, AOM and AOPDF can be used with update rates up to a few hundreds of kHz. Therefore, they allow a change of the shaping mask on

a pulse-to-pulse basis. This is especially favorable for applications, where the pulse shape is a scanning parameter (e.g. in two-dimensional spectroscopy).
In conclusion, the performance of AOM 1 is comparable to other shaping devices in the UV. The maximum delay of a double pulse can be seen as a weak spot, but it should not be limiting for the aplication of the shaped pulses. The output efficiency of AOM 1 is the best in comparison to the one of the other devices due to an ideal choice of gratings and mirrors. Another advantage is the flexibility of the set-up as it can be used in the large spectral range from 250 nm to 350 nm.

Literature	AOM 1	AOM 2 [30]	AOPDF [124]	MEMS [27, 118]	UV-LCM [127]	IND 1; 2 [28]; [125]
Central wavelength / utilized wavelength range [nm]	250-350	262	250-400	300-340	390	200; 295-370
Shaping window [nm]	21	9	30-60	16	25	0.43; 49
Transmission^{t} / reflection^{r} / diffraction^{d} efficiency [%]	70^{d}	78^{d}	20^{d}	85^{r}	> 85^{t}	-
Output efficiency of set-up [%]	30	21	20	25	21^{e}	-
Shaping of phase (ϕ) / amplitude (A)	ϕ and A	ϕ and A	ϕ and A	ϕ and A	ϕ or A	ϕ; ϕ and A^{p}
Number of pixels^{p} / features^{f}	168^{f}	150^{f}	^{r}	240 x 200^{p}	648 x 2^{p}	160; 256^{g,p}
τ_{max} [ps] (c.f. Eqn. (4.28))	1.5	1.9	3 - 4	2.7	3.6	25.8; 1.2
Maximum update rate [kHz]	300	300	300^{s}	0.33^{u}	cw to 0.1	cw to 0.1

Table 4.2: Properties of the various shaping techniques in the UV for comparison.
^{e} The value is not provided in Ref. [127]. It is estimated for a prism-based 4f set-up with a prism efficiency of 50 %. The losses of the utilized mirrors are neglected.
^{g} These values are given for the shaping of the fundamental. Assuming that the whole spectrum is transferred to the UV, the number of pixels is maintained in the UV.
^{p} Polarization shaping is possible as shown in Ref. [131, 132] for the second-harmonic signal of a 800 nm laser.
^{r} The number of features is not provided in Ref. [124].
^{s} 300 kHz is limited by the acoustic waveform refreshing time; due to the technical implementation the update rate was smaller in Ref. [124].
^{u} Optimized update rate for the application with a 1 kHz system (c.f. Ref. [43]).

4.7 Summary and Outlook for UV Shaping

	260 nm	330 nm
Diffraction efficiency (AOM)	70 %	50 %
Diffraction efficiency (2 gratings)	42 %	68 %
Output efficiency (4f + AOM)	26 %	30 %
Maximum linear chirp ϕ''	3000 fs^2	8000 fs^2
Maximum double pulse distance	0.9 ps	1.5 ps

Table 4.3: Efficiencies and shaping limitations of the AOM. The total efficiency is further reduced due to the four mirrors (currently with aluminum coating), which are necessary to integrate the 4f set-up into the whole laser set-up.

Overall, the shaping performance of the AOM is promising. The set-up allows for shaping of femtosecond pulses with a total spectral width of up to 21 nm between 250 nm to 350 nm. The overall efficiency of the set-up is between 26 % and 30 % and double pulses with a maximum separation of 0.9 ps and 1.5 ps for 260 nm and 330 nm is possible (see Table 4.3). A comparison of several current UV shaping devices shows that the developed set-up has a higher efficiency than the other devices. Although it provides less flexibility for the pulse shaping, it will be sufficient for various applications of the shaped pulses.

There are numerous avenues to apply UV shaping. In general, the concept of a systematic study as demonstrated in Chapter 3 can be transferred into the UV for studying e.g. organic compounds. The advantage of such studies in the UV is that the complexity of simple systems, which typically absorb in the UV, is significantly reduced. Subsequently, the analysis and interpretation of the observed processes can be more straightforward.
A class of molecules with high prospects are coumarin derivatives. They find applications in biomedicine e.g. as HIV-inhibitors [133]. Ultrafast processes in coumarin monomers and coumarin dimers were investigated with unshaped pulses earlier in our research group [134, 135]. From the work performed, the question arises how branching points in the excited state manifold, quantum yields and cleavage dynamics can be manipulated by shaped pulses.

For sufficiently high light intensities, photodissociation of even smaller systems consisting of a few atoms can be studied. Such experiments are of special interest as quantum mechanical calculations are available with high precision to model the observed processes (e.g. [136]).
Another type of molecule with immense impact in biology is DNA. It has been addressed with a variety of ultrafast techniques such as pump-probe mass spectrometry [137], time-resolved photoelectron spectroscopy [138] and UV transient absorption spectroscopy [139, 140] to investigate the dynamics of the excited state. With shaped pulses it could be possible to control the timescale of these dynamics. In addition, it was used as a prototype to demonstrate two-dimensional (2D) spectroscopy in the UV.
2D spectroscopy in general is used to study molecular structures and energy transfer. Prominent examples are electronic coupling in photosynthesis and semiconductor carrier dynamics [141]. The measured quantity is the third order polarization, which is induced by a pair of excitation pulses. A high phase stability between these two pulses is essential. In the infrared spectral range, set-ups with diffractive optics [142, 143] or active interferometric stabilization [144] or a birefringent delay line [145] are sufficient for this purpose. In the UV regime, it is more challenging, as when changing the spectral range to the UV, the phase stability has to improve by one order of magnitude due to the smaller wavelength. Nevertheless, femtosecond pulses shaped into double pulses provide such a stability as recently shown for a AOPDF [146]. An advantage of the AOPDF, and the AOM-shaper developed in this thesis, is that they allow one to change the pulse shape as a continuous varying parameter from shot to shot.
Related to these perspectives is also the option to perform resonant Raman spectroscopy. The set-up allows for directly implementing single-beam CARS (coherent anti-Stokes Raman scattering) to temporally resolve and manipulate molecular vibrations. It was typically performed in the near-infrared [147–149]. Its transfer into the UV to resonant electronic transitions will dramatically improve its sensitivity. Therefore in the future, compounds will be studied at low concentrations, which is crucial for its applications e.g. in remote sensing.
In conclusion, there is a vast range of molecules and concepts, which can be addressed with this shaping set-up in the UV. For all these techniques, transient absorption, 2D or resonant Raman spectroscopy, the presented set-up allows

temporal shaping similar to other shaping set-ups. Its advantage is the tunability to modify the spectral overlap between excitation and absorption spectra.

5 Summary and Outlook

One of the long-term goals in femtochemistry is the ability to control chemical reactions with a quantum mechanical approach. Remarkable benchmarks could be set in this field over the last decades. However, despite the vast number of examples for successful control experiments, the parameter space is huge and an efficient parameter set has often been found by chance or after many unsuccessful trials. The control in the low-intensity regime is thereby of special interest as light-driven reactions in nature occur in this regime. Therefore, the main goal of this thesis was to perform a systematic study on a prototype molecule with the aim of providing a guideline for future coherent control experiments at low pulse intensity. As the coherently controlled dynamics can strongly depend on the pulse shape, reliable pulse shapes on a pulse-to-pulse basis are crucial for this purpose.

A widespread device for pulse shaping is the LCM. Nevertheless, a low-frequency phase noise generated by LCMs was reported for the first time in the scope of this thesis. This phase noise led to very strong pulse deformations, independent of the applied phase parameterization, as visualized by shot-to-shot autocorrelation traces. The power spectrum obtained in experiments and the observed strong temperature dependence of the phase noise indicate that the noise originates from molecular properties of the nematic liquid crystal molecules, such as their temperature dependent mobility. The effect of phase noise was further investigated by a numerical simulation of the autocorrelation. The noise was a direct input parameter for the phase of the simulated pulse. A time dependence as observed in the experimental data and a coupling across the phase of the spectral components were introduced to reproduce the experimental autocorre-

lation traces. The phase noise of the LCM was strongly minimized by a careful choice of experimental parameters. Firstly, the shot-to-shot stability of the output tailored pulse was improved by a factor of two due to external cooling of the LCM. Secondly, rapid-scan averaging of the data led to a suppression of the low-frequency phase noise by one order of magnitude. Combining these two strategies allows to apply LCMs to sub-15 fs laser pulses with high precision. The reason, why such phase noise has never been reported earlier in the shaping community, is that two prerequisites have to be fulfilled for its observation. Firstly, a sufficient spectral width of the tailored pulse is required as the impact of the phase noise increases with the tailored spectral width as the simulations show. Secondly, the instabilities mainly appear in a shot-to-shot acquisition and especially in combination with low laser repetition rates (kHz) due to the low-frequency dependence of the instabilities. However, LCMs are mainly utilized to shape pulses from lasers with high repetition rates (tens of MHz) or less broad laser spectra. After a satisfying minimization for spectrally broad laser pulses with a low repetition rate was realized, coherent control experiments, where only small differences in the shaped pulses were important, could be performed.

These experiments comprised a systematic study on the prototype molecule Nile Blue, an oxazine dye. The excitation spectrum was tuned across the absorption spectrum of Nile Blue and the temporal shape of the excitation pulse was tailored to linearly chirped pulses and to multipulses, whose interpulse distance matches the period of the dominant ring breathing mode of Nile Blue, and additionally to the combination of both to generate a complete data set. The effect of the shaped pulses on population and vibrational coherence in the ground and excited state was evaluated. The results for population and vibrational coherence were combined for a general statement about the spectral and temporal parameters, which lead to the best enhancement. While the ideal choice for the ground state is a resonant negatively chirped multipulse, the excited state is enhanced best with a blue-detuned positively chirped multipulse. The systematic study indicates that a careful choice of the excitation pulse with respect to its temporal shape as well as its spectrum is crucial for a successful control experiment. Furthermore, it shows that the sum of linear chirp and multipulse parametrization even improves the enhancement compared to the use of only one of these two

types of parametrization. More general, the study can be utilized as a guideline for future control experiments to choose favorable parameter sets.
In the near future, a theoretical study will be performed to gain a deeper understanding and to be able to give even more general statements. It will be based on similar parameters as the experiment and in particular it will include chirped multipulses. Furthermore, the parameter set for temporal shaping can be expanded. One possibility is to add linear chirp of different sign and strength to the subpulses within the multipulse. Next, the molecular system can be varied, starting with other types of oxazines.

Inspired by the improved pulse shaping technique in the visible and the successful systematic study on control experiments, a further project has been started, which should enable the performance of control experiments in the UV in the future. To follow this avenue, an AOM-based shaping set-up in the UV was developed. This set-up allows for the shaping of sub-30 fs pulses with a central wavelength between 250 nm to 350 nm. The overall efficiency of the set-up is up to 30 %. Double pulses with a maximum separation of 0.9 ps and 1.5 ps are possible for 260 nm and 330 nm, respectively.
This setup offers the opportunity to transfer the concept of a systematic study into the ultraviolet wavelength regime to study organic compounds with absorption bands in the UV. Furthermore, 2D spectroscopy becomes possible with this setup as sufficient phase stability is provided, which is typically the limiting factor for set-ups without pulse shaper. In addition, resonant Raman spectroscopy with clearly enhanced sensitivity compared to near-infrared Raman spectroscopy seems feasible. Molecular candidates of great interest are the DNA and RNA bases. Their examination in the one-photon regime is of special importance as DNA damage occurs in nature due to sun light, i.e. at low intensity.

Bibliography

[1] H. Rabitz et al. “Whither the Future of Controlling Quantum Phenomena?” In: *Science* 288.5467 (2000), pp. 824–828. DOI: 10.1126/science.288.5467.824.

[2] T. Brixner et al. “Photoselective adaptive femtosecond quantum control in the liquid phase”. In: *Nature* 414.6859 (2001), pp. 57–60. DOI: 10.1038/35102037.

[3] M. Dantus. “COHERENT NONLINEAR SPECTROSCOPY: From Femtosecond Dynamics to Control”. In: *Annual Review of Physical Chemistry* 52.1 (2001), pp. 639–679. DOI: 10.1146/annurev.physchem.52.1.639.

[4] D. Brinks et al. “Coherent control of single molecules at room temperature”. In: *Faraday Discussions* 153.0 (2011), pp. 51–60. DOI: 10.1039/C1FD00087J.

[5] A. Assion et al. “Control of Chemical Reactions by Feedback-Optimized Phase-Shaped Femtosecond Laser Pulses”. In: *Science* 282.5390 (1998), pp. 919–922. DOI: 10.1126/science.282.5390.919.

[6] J. L. Herek et al. “Quantum control of energy flow in light harvesting”. In: *Nature* 417.6888 (2002), pp. 533–535. DOI: 10.1038/417533a.

[7] J. Savolainen et al. “Controlling the efficiency of an artificial light-harvesting complex”. In: *Proceedings of the National Academy of Sciences* 105.22 (2008), pp. 7641–7646. DOI: 10.1073/pnas.0711927105.

[8] V. I. Prokhorenko et al. “Coherent Control of Retinal Isomerization in Bacteriorhodopsin”. In: *Science* 313.5791 (2006), pp. 1257–1261. DOI: 10.1126/science.1130747.

[9] M. Shapiro and P. Brumer. "Coherent control of molecular dynamics". In: *Reports on Progress in Physics* 66.6 (2003), p. 859. DOI: 10.1088/0034-4885/66/6/201.

[10] G. Vogt et al. "Femtosecond pump–shaped-dump quantum control of retinal isomerization in bacteriorhodopsin". In: *Chemical Physics Letters* 433.1–3 (2006), pp. 211–215. DOI: 10.1016/j.cplett.2006.11.028.

[11] V. I. Prokhorenko et al. "On the mechanism of weak-field coherent control of retinal isomerization in bacteriorhodopsin". In: *Chemical Physics* 341.1–3 (2007), pp. 296–309. DOI: https://doi.org/10.1016/j.chemphys.2007.07.031.

[12] C. J. Bardeen, Q. Wang, and C. V. Shank. "Selective Excitation of Vibrational Wave Packet Motion Using Chirped Pulses". In: *Physical Review Letters* 75.19 (1995), pp. 3410–3413. DOI: 10.1103/PhysRevLett.75.3410.

[13] J. Hauer, T. Buckup, and M. Motzkus. "Enhancement of molecular modes by electronically resonant multipulse excitation: Further progress towards mode selective chemistry". In: *The Journal of Chemical Physics* 125.6 (2006), p. 061101. DOI: 10.1063/1.2243273.

[14] T. Buckup et al. "Control of excited-state population and vibrational coherence with shaped-resonant and near-resonant excitation". In: *Journal of Physics B: Atomic, Molecular and Optical Physics* 41.7 (2008), p. 074024. DOI: 10.1088/0953-4075/41/7/074024.

[15] A. Weigel, A. Sebesta, and P. Kukura. "Shaped and Feedback-Controlled Excitation of Single Molecules in the Weak-Field Limit". In: *The Journal of Physical Chemistry Letters* 6.20 (2015). PMID: 26706166, pp. 4032–4037. DOI: 10.1021/acs.jpclett.5b01748.

[16] A. M. Weiner, J. P. Heritage, and E. M. Kirschner. "High-resolution femtosecond pulse shaping". In: *Journal of the Optical Society of America B* 5.8 (1988), p. 1563. DOI: 10.1364/JOSAB.5.001563.

[17] A. M. Weiner et al. "Programmable femtosecond pulse shaping by use of a multielement liquid-crystal phase modulator". In: *Optics Letters* 15.6 (1990), pp. 326–328. DOI: 10.1364/OL.15.000326.

[18] C. W. Hillegas et al. “Femtosecond laser pulse shaping by use of microsecond radio-frequency pulses”. In: *Optics Letters* 19.10 (1994), pp. 737–739. DOI: 10.1364/OL.19.000737.

[19] P. Tournois. “Acousto-optic programmable dispersive filter for adaptive compensation of group delay time dispersion in laser systems”. In: *Optics Communications* 140.4–6 (1997), pp. 245–249. DOI: 10.1016/S0030-4018(97)00153-3.

[20] D. Kaplan and P. Tournois. “Theory and performance of the acousto optic programmable dispersive filter used for femtosecond laser pulse shaping”. In: *Journal de Physique IV (Proceedings)* 12.5 (2002), pp. 69–75. DOI: 10.1051/jp4:20020098.

[21] G. Stobrawa et al. “A new high-resolution femtosecond pulse shaper”. In: *Applied Physics B* 72.5 (2001), pp. 627–630. DOI: 10.1007/s003400100576.

[22] J. M. Maxson, A. C. Bartnik, and I. V. Bazarov. “Efficient and accurate laser shaping with liquid crystal spatial light modulators”. In: *Applied Physics Letters* 105.17 (2014), p. 171109. DOI: 10.1063/1.4900835.

[23] J. Köhler et al. “Zeptosecond precision pulse shaping”. In: *Optics Express* 19.12 (2011), p. 11638. DOI: 10.1364/OE.19.011638.

[24] I. Kozma et al. “Widely tunable sub-30 fs ultraviolet pulses by chirped sum frequency mixing”. In: *Optics Express* 11.23 (2003), pp. 3110–3115. DOI: 10.1364/OE.11.003110.

[25] P. Baum, S. Lochbrunner, and E. Riedle. “Tunable sub-10-fs ultraviolet pulses generated by achromatic frequencydoubling”. In: *Optics Letters* 29.14 (2004), pp. 1686–1688. DOI: 10.1364/OL.29.001686.

[26] C. Homann, P. Lang, and E. Riedle. “Generation of 30 fs pulses tunable from 189 to 240 nm with an all-solid-state setup”. In: *J. Opt. Soc. Am. B* 29.10 (2012), pp. 2765–2769. DOI: 10.1364/JOSAB.29.002765.

[27] M. Hacker et al. “Micromirror SLM for femtosecond pulse shaping in the ultraviolet”. In: *Applied Physics B* 76.6 (2003), pp. 711–714. DOI: 10.1007/s00340-003-1180-0.

[28] M. Hacker et al. “Programmable femtosecond laser pulses in the ultraviolet”. In: *Journal of the Optical Society of America B* 18.6 (2001), pp. 866–871. DOI: 10.1364/JOSAB.18.000866.

[29] S. Coudreau, D. Kaplan, and P. Tournois. “Ultraviolet acousto-optic programmable dispersive filter laser pulse shaping in KDP”. In: *Optics Letters* 31.12 (2006), pp. 1899–1901. DOI: 10.1364/OL.31.001899.

[30] B. J. Pearson and T. C. Weinacht. “Shaped ultrafast laser pulses in the deep ultraviolet”. In: *Optics Express* 15.7 (2007), pp. 4385–4388. DOI: 10.1364/OE.15.004385.

[31] G. Thalhammer et al. “Speeding up liquid crystal SLMs using overdrive with phase change reduction”. In: *Optics Express* 21.2 (2013), p. 1779. DOI: 10.1364/OE.21.001779.

[32] *Springer handbook of lasers and optics*. 2. ed. Berlin ; Heidelberg [u.a.]: Springer, 2012. DOI: 10.1007/978-3-642-19409-2.

[33] J. Voll and R. d. Vivie-Riedle. “Pulse trains in molecular dynamics and coherent spectroscopy: a theoretical study”. In: *New Journal of Physics* 11.10 (2009), p. 105036. DOI: 10.1088/1367-2630/11/10/105036.

[34] w. c. 10. print. *Handbook of mathematical functions. with formulas, graphs, and mathematical tables*. Ed. by M. Abramowitz. National Bureau of Standards applied mathematics series. Washington, DC: U. S. Government Printing Office, 1972.

[35] E. W. Weisstein. *Jacobi-Anger Expansion*. Accessed 2017-04-13. www.mathworld.wolfram.com/Jacobi-AngerExpansion.html.

[36] I. Z. Kozma et al. “Compact autocorrelator for the online measurement of tunable 10 femtosecond pulses”. In: *Review of Scientific Instruments* 75.7 (2004), pp. 2323–2327. DOI: 10.1063/1.1764615.

[37] R. Trebino et al. “Measuring ultrashort laser pulses in the time-frequency domain using frequency-resolved optical gating”. In: *Review of Scientific Instruments* 68.9 (1997), pp. 3277–3295. DOI: 10.1063/1.1148286.

[38] C. Iaconis and I. A. Walmsley. “Spectral phase interferometry for direct electric-field reconstruction of ultrashort optical pulses”. In: *Optics Letters* 23.10 (1998), pp. 792–794. DOI: 10.1364/OL.23.000792.

[39] V. V. Lozovoy, I. Pastirk, and M. Dantus. "Multiphoton intrapulse interference. IV. Ultrashort laser pulse spectral phase characterization and compensation". In: *Optics Letters* 29.7 (2004), pp. 775–777. DOI: 10.1364/OL.29.000775.

[40] M. Miranda et al. "Characterization of broadband few-cycle laser pulses with the d-scan technique". In: *Optics Express* 20.17 (2012), pp. 18732–18743. DOI: 10.1364/OE.20.018732.

[41] L. I. Isaenko et al. "Anisotropy of two-photon absorption in BBO at 264 nm". In: *Optics Communications* 198.4 (2001), pp. 433–438.

[42] D. C. Edelstein et al. "Femtosecond ultraviolet pulse generation in β-BaB_2O_4". In: *Applied Physics Letters* 52.26 (1988), pp. 2211–2213. DOI: 10.1063/1.99767.

[43] J. M. Möhring. *Methoden zur Erzeugung und Charakterisierung von geformten Femtosekunden-UV-Impulsen und deren Anwendung*. Dissertation. Universität Marburg, 2011. DOI: http://dx.doi.org/10.17192/z2011.0491.

[44] M. Jiang. *Femtosecond UV transient absorption study of coumarin dimers*. Dissertation, Ruperto-Carola University, 2017. Heidelberg. DOI: 10.11588/heidok.00022677.

[45] J. Möhring, T. Buckup, and M. Motzkus. "Shaper-assisted full-phase characterization of UV pulses without a spectrometer". In: *Optics Letters* 35.23 (2010), pp. 3916–3918. DOI: 10.1364/OL.35.003916.

[46] R. Borrego-Varillas et al. "Optimized ancillae generation for ultra-broadband two-dimensional spectral-shearing interferometry". In: *Journal of the Optical Society of America B* 32.9 (2015), p. 1851. DOI: 10.1364/JOSAB.32.001851.

[47] JENOPTIK Laser Optik Systeme GmbH. *SLM-S 640/d Technical Documentation*. 2004.

[48] A. M. Weiner. "Femtosecond pulse shaping using spatial light modulators". In: *Review of Scientific Instruments* 71.5 (2000), pp. 1929–1960. DOI: 10.1063/1.1150614.

[49] P.-G. de Gennes and J. Prost. *The physics of liquid crystals*. 2. ed., repr. International series of monographs on physics ARRAY(0x31ec078). Oxford: Clarendon Press, 2008.

[50] M. Karim. *Electro-Optical Displays*. Optical Science and Engineering. Taylor & Francis, 1992.

[51] R. W. Boyd. *Nonlinear optics*. 3rd ed. Burlington, MA: Academic Press, 2008.

[52] G. New. *Introduction to Nonlinear Optics*. Cambridge: Cambridge University Press, 2011.

[53] K. Hazu, T. Sekikawa, and M. Yamashita. "Spatial light modulator with an over-two-octave bandwidth from ultraviolet to near infrared". In: *Optics Letters* 32.22 (2007), pp. 3318–3320. DOI: 10.1364/OL.32.003318.

[54] B. E. A. Saleh and M. C. Teich. *Fundamentals of photonics*. 2. ed. Wiley series in pure and applied optics. Hoboken, N.J.: Wiley, 2007.

[55] M. Plewicki et al. "Phase, amplitude, and polarization shaping with a pulse shaper in a Mach-Zehnder interferometer". In: *Applied Optics* 45.32 (2006), pp. 8354–8359. DOI: 10.1364/AO.45.008354.

[56] F. Weise and A. Lindinger. "Full control over the electric field using four liquid crystal arrays". In: *Optics Letters* 34.8 (2009), p. 1258. DOI: 10.1364/OL.34.001258.

[57] C. Schwarz, O. Hüter, and T. Brixner. "Full vector-field control of ultrashort laser pulses utilizing a single dual-layer spatial light modulator in a common-path setup". In: *J. Opt. Soc. Am. B* 32.5 (2015), pp. 933–945. DOI: 10.1364/JOSAB.32.000933.

[58] G. Cerullo et al. "Sub-8-fs pulses from an ultrabroadband optical parametric amplifier in the visible". In: *Optics Letters* 23.16 (1998), pp. 1283–1285. DOI: 10.1364/OL.23.001283.

[59] G. M. Gale, M. Cavallari, and F. Hache. "Femtosecond visible optical parametric oscillator". In: *JOSA B* 15.2 (1998), pp. 702–714. DOI: 10.1364/JOSAB.15.000702.

[60] A. Shirakawa, I. Sakane, and T. Kobayashi. "Pulse-front-matched optical parametric amplification for sub-10-fs pulse generation tunable in the visible and near infrared". In: *Optics Letters* 23.16 (1998), pp. 1292–1294. DOI: 10.1364/OL.23.001292.

[61] E. Riedle et al. "Generation of 10 to 50 fs pulses tunable through all of the visible and the NIR". In: *Applied Physics B* 71.3 (2000), pp. 457–465. DOI: 10.1007/s003400000351.

[62] B. Schmidt et al. *LAB2 - A virtual femtosecond laser lab*. http://www.lab2.de.

[63] A. Wand et al. "Chirp effects on impulsive vibrational spectroscopy: a multimode perspective". In: *Physical Chemistry Chemical Physics* 12.9 (2010), pp. 2149–2163. DOI: 10.1039/B920356G.

[64] J. A. Moon. "Optimization of signal-to-noise ratios in pump-probe spectroscopy". In: *Review of Scientific Instruments* 64.7 (1993), pp. 1775–1778. DOI: 10.1063/1.1144009.

[65] D. von der Linde. "Characterization of the noise in continuously operating mode-locked lasers". In: *Applied Physics B* 39.4 (1986), pp. 201–217. DOI: 10.1007/BF00697487.

[66] E. N. Ivanov, S. A. Diddams, and L. Hollberg. "Experimental study of noise properties of a Ti:sapphire femtosecond laser". In: *IEEE Transactions on Ultrasonics, Ferroelectrics, and Frequency Control* 50.4 (2003), pp. 355–360. DOI: 10.1109/TUFFC.2003.1197957.

[67] T. Buckup and M. Motzkus. "Multidimensional Time-Resolved Spectroscopy of Vibrational Coherence in Biopolyenes". In: *Annual Review of Physical Chemistry* 65.1 (2014), pp. 39–57. DOI: 10.1146/annurev-physchem-040513-103619.

[68] A. Yabushita, Y.-H. Lee, and T. Kobayashi. "Development of a multiplex fast-scan system for ultrafast time-resolved spectroscopy". In: *The Review of Scientific Instruments* 81.6 (2010), p. 063110. DOI: 10.1063/1.3455809.

[69] M. Gueye et al. "Broadband UV-Vis vibrational coherence spectrometer based on a hollow fiber compressor". In: *Review of Scientific Instruments* 87.9 (2016), p. 093109. DOI: 10.1063/1.4962699.

[70] H. Stegemeyer et al. *Liquid Crystals*. Topics in Physical Chemistry. Steinkopff, 2013.

[71] C. Cramer et al. "Measurement of orientational order and mobility of a nematic liquid crystal in random nanometer confinement". In: *The Journal of Chemical Physics* 106.9 (1997), pp. 3730–3742. DOI: 10.1063/1.473425.

[72] Personal communication with P. Gussek from JENOPTIK Optical Systems GmbH. 2017-05-08.

[73] A. M. Weiner et al. "Femtosecond Pulse Sequences Used for Optical Manipulation of Molecular Motion". In: *Science* 247.4948 (1990), pp. 1317–1319. DOI: 10.1126/science.247.4948.1317.

[74] T. Hornung, R. Meier, and M. Motzkus. "Optimal control of molecular states in a learning loop with a parameterization in frequency and time domain". In: *Chemical Physics Letters* 326.5–6 (2000), pp. 445–453. DOI: 10.1016/S0009-2614(00)00810-1.

[75] V. V. Lozovoy et al. "The role of pulse sequences in controlling ultrafast intramolecular dynamics with four-wave mixing". In: *International Reviews in Physical Chemistry* 19.4 (2000), pp. 531–552. DOI: 10.1080/014423500750040609.

[76] N. Dudovich, D. Oron, and Y. Silberberg. "Single-pulse coherent anti-Stokes Raman spectroscopy in the fingerprint spectral region". In: *The Journal of Chemical Physics* 118.20 (2003), pp. 9208–9215. DOI: 10.1063/1.1568072.

[77] T. Hornung, H. Skenderović, and M. Motzkus. "Observation of all-trans-β-carotene wavepacket motion on the electronic ground and excited dark state using degenerate four-wave mixing (DFWM) and pump–DFWM". In: *Chemical Physics Letters* 402.4–6 (2005), pp. 283–288. DOI: 10.1016/j.cplett.2004.11.135.

[78] J. R. Durrant et al. "Subpicosecond equilibration of excitation energy in isolated photosystem II reaction centers". In: *Proceedings of the National Academy of Sciences* 89.23 (1992), pp. 11632–11636.

[79] M. H. Vos, J. Breton, and J.-L. Martin. "Electronic Energy Transfer within the Hexamer Cofactor System of Bacterial Reaction Centers". In: *The Journal of Physical Chemistry B* 101.47 (1997), pp. 9820–9832. DOI: 10.1021/jp971486h.

[80] A. M. Streltsov et al. "BA and BB Absorbance Perturbations Induced by Coherent Nuclear Motions in Reaction Centers from Rhodobacter sphaeroides upon 30-fs Excitation of the Primary Donor". In: *The Journal of Physical Chemistry B* 102.37 (1998), pp. 7293–7298. DOI: 10.1021/jp981514b.

[81] J. Hauer et al. "Enhancement of Raman modes by coherent control in β-carotene". In: *Chemical Physics Letters* 421.4–6 (2006), pp. 523–528. DOI: 10.1016/j.cplett.2006.01.115.

[82] C. J. Bardeen, Q. Wang, and C. V. Shank. "Femtosecond Chirped Pulse Excitation of Vibrational Wave Packets in LD690 and Bacteriorhodopsin". In: *The Journal of Physical Chemistry A* 102.17 (1998), pp. 2759–2766. DOI: 10.1021/jp980346k.

[83] S. Malkmus et al. "Chirp Dependence of Wave Packet Motion in Oxazine 1". In: *The Journal of Physical Chemistry A* 109.46 (2005), pp. 10488–10492. DOI: 10.1021/jp054462g.

[84] M. Braun et al. "Analysis of Wave Packet Motion in Frequency and Time Domain: Oxazine 1". In: *The Journal of Physical Chemistry A* 110.32 (2006), pp. 9793–9800. DOI: 10.1021/jp0575431.

[85] A. C. Florean et al. "Optical Control of Excited-State Vibrational Coherences of a Molecule in Solution: The Influence of the Excitation Pulse Spectrum and Phase in LD690†". In: *The Journal of Physical Chemistry B* 110.40 (2006), pp. 20023–20031. DOI: 10.1021/jp0627628.

[86] W. T. Pollard et al. "Quantum-mechanical theory for 6 fs dynamic absorption spectroscopy and its application to nile blue". In: *Chemical Physics Letters* 168.3–4 (1990), pp. 239–245. DOI: 10.1016/0009-2614(90)85603-A.

[87] T. Arlt et al. "The accessory bacteriochlorophyll: a real electron carrier in primary photosynthesis". In: *Proceedings of the National Academy of Sciences* 90.24 (1993), pp. 11757–11761.

[88] S. Prahl. *Nile Blue*. http://omlc.org/spectra/PhotochemCAD/html/005.html. 2012.

[89] S. A. Kovalenko et al. "Femtosecond spectroscopy of condensed phases with chirped supercontinuum probing". In: *Physical Review A* 59.3 (1999), pp. 2369–2384. DOI: 10.1103/PhysRevA.59.2369.

[90] O. G. Kosareva et al. "From Filamentation in Condensed Media to Filamentation in Gases". In: *Journal of Nonlinear Optical Physics and Materials* 06.04 (1997), pp. 485–494. DOI: 10.1142/S0218863597000368.

[91] A. Couairon and A. Mysyrowicz. "Femtosecond filamentation in transparent media". In: *Physics Reports* 441.2–4 (2007), pp. 47–189. DOI: https://doi.org/10.1016/j.physrep.2006.12.005.

[92] T. Buckup, J. Hauer, and M. Motzkus. "On the paradigm of coherent control: the phase-dependent light–matter interaction in the shaping window". In: *New Journal of Physics* 11.10 (2009), p. 105049. DOI: 10.1088/1367-2630/11/10/105049.

[93] M. Lorenc et al. "Artifacts in femtosecond transient absorption spectroscopy". In: *Applied Physics B* 74.1 (2002), pp. 19–27. DOI: 10.1007/s003400100750.

[94] T. Butz. *Fourier Transformation for Pedestrians*. Ed. by H. Klose et al. 2nd ed. 2015. Undergraduate Lecture Notes in Physics. Cham: Springer International Publishing, 2015.

[95] F. Frei, A. Galler, and T. Feurer. "Space-time coupling in femtosecond pulse shaping and its effects on coherent control". In: *The Journal of Chemical Physics* 130.3 (2009), p. 034302. DOI: 10.1063/1.3058478.

[96] A. Cusano et al. *Optochemical Nanosensors*. Series in Sensors. CRC Press, 2016.

[97] P. Myslinski, D. Wieczorek, and K. Kownacki. "Picosecond fluorescence anisotropy measured by frequency conversion". In: *Chemical Physics Letters* 155.3 (1989), pp. 256–261. DOI: 10.1016/0009-2614(89)85320-5.

[98] F. W. Wise, M. J. Rosker, and C. L. Tang. "Oscillatory femtosecond relaxation of photoexcited organic molecules". In: *The Journal of Chemical Physics* 86.5 (1987), pp. 2827–2832. DOI: 10.1063/1.452032.

[99] M. K. Lawless and R. A. Mathies. "Excited-state structure and electronic dephasing time of Nile blue from absolute resonance Raman intensities". In: *The Journal of Chemical Physics* 96.11 (1992), pp. 8037–8045. DOI: 10.1063/1.462355.

[100] M. K. Lawless. "Excited State Structure and Dynamics from Absolute Resonance Raman Intensities: the Photochemistry and Photophysics of 1,3,5-Cyclooctatriene, Cyclobutene and Nile Blue." In: *Ph.D. Thesis* (1993).

[101] A. Grofcsik, M. Kubinyi, and W. Jeremy Jones. "Intermolecular photoinduced proton transfer in nile blue and oxazine 720". In: *Chemical Physics Letters* 250.3 (1996), pp. 261–265. DOI: 10.1016/0009-2614(96)00003-6.

[102] A. Ghanadzadeh Gilani et al. "Excited state electric dipole moment of nile blue and brilliant cresyl blue: A comparative study". In: *Spectrochimica Acta Part A: Molecular and Biomolecular Spectroscopy* 89 (2012), pp. 231–237. DOI: 10.1016/j.saa.2011.12.063.

[103] Y. Zhang, S. R. Hartmann, and F. Moshary. "Incoherent four-wave-mixing on nile blue and cresyl violet in glass and polymer at 5 K: Single-site line shape analysis". In: *The Journal of Chemical Physics* 104.12 (1996), pp. 4380–4389. DOI: 10.1063/1.471189.

[104] Y. Nagasawa et al. "Two-Dimensional Analysis of Integrated Three-Pulse Photon Echo Signals of Nile Blue Doped in PMMA". In: *The Journal of Physical Chemistry A* 107.14 (2003), pp. 2431–2441. DOI: 10.1021/jp027012m.

[105] C. W. Lin et al. "Lysosomal localization and mechanism of uptake of Nile blue photosensitizers in tumor cells". In: *Cancer Research* 51.10 (1991), pp. 2710–2719.

[106] J. A. Cina et al. "Ultrafast transient absorption revisited: Phase-flips, spectral fingers, and other dynamical features". In: *The Journal of Chemical Physics* 144.17 (2016), p. 175102. DOI: 10.1063/1.4947568.

[107] J. P. Kraack et al. "Ground- and excited-state vibrational coherence dynamics in Bacteriorhodopsin probed with degenerate four-wave-mixing experiments". In: *Chemphyschem: A European Journal of Chemical Physics and Physical Chemistry* 12.10 (2011), pp. 1851–1859. DOI: 10.1002/cphc.201100032.

[108] G. Socrates. *Infrared and Raman Characteristic Group Frequencies: Tables and Charts*. Wiley, 2004.

[109] W. T. Pollard et al. "Theory of dynamic absorption spectroscopy of nonstationary states. 4. Application to 12-fs resonant impulsive Raman spectroscopy of bacteriorhodopsin". In: *The Journal of Physical Chemistry* 96.15 (1992), pp. 6147–6158. DOI: 10.1021/j100194a013.

[110] A. T. N. Kumar et al. "Investigations of amplitude and phase excitation profiles in femtosecond coherence spectroscopy". In: *The Journal of Chemical Physics* 114.2 (2001), pp. 701–724.

[111] A. L. Dobryakov and N. P. Ernsting. "Lineshapes for resonant impulsive stimulated Raman scattering with chirped pump and supercontinuum probe pulses". In: *The Journal of Chemical Physics* 129.18 (2008), p. 184504. DOI: 10.1063/1.3009221.

[112] I. J. Afa and C. Serrat. "Quantum Control of Population Transfer and Vibrational States via Chirped Pulses in Four Level Density Matrix Equations". In: *Applied Sciences* 6.11 (2016), p. 351. DOI: 10.3390/app6110351.

[113] G. Cerullo et al. "High-power femtosecond chirped pulse excitation of molecules in solution". In: *Chemical Physics Letters* 262.3–4 (1996), pp. 362–368. DOI: 10.1016/0009-2614(96)01092-5.

[114] E. C. Carroll et al. "Phase control of the competition between electronic transitions in a solvated laser dye". In: *Chemical Physics*. Femtochemistry and FemtobiologyPapers associated with the 8th International Conference on Femtochemistry and Femtobiology 350.1–3 (2008), pp. 75–86. DOI: 10.1016/j.chemphys.2008.01.023.

[115] C. J. Bardeen et al. "Feedback quantum control of molecular electronic population transfer". In: *Chemical Physics Letters* 280.1–2 (1997), pp. 151–158. DOI: 10.1016/S0009-2614(97)01081-6.

[116] R. P. Sinha and D.-P. Hader. "UV-induced DNA damage and repair: a review". In: *Photochem. Photobiol. Sci.* 1 (4 2002), pp. 225–236. DOI: 10.1039/B201230H.

[117] J. T. Reardon and A. Sancar. "Recognition and repair of the cyclobutane thymine dimer, a major cause of skin cancers, by the human excision nuclease". In: *Genes & Development* 17.20 (2003), pp. 2539–2551. DOI: 10.1101/gad.1131003.

[118] J. Möhring et al. "Generation of phase-controlled ultraviolet pulses and characterization by a simple autocorrelator setup". In: *Journal of the Optical Society of America B* 26.8 (2009), pp. 1538–1544. DOI: 10.1364/JOSAB.26.001538.

[119] A. Rondi et al. "Characterization of a MEMS-based pulse-shaping device in the deep ultraviolet". In: *Applied Physics B* 96.4 (2009), pp. 757–761. DOI: 10.1007/s00340-009-3548-2.

[120] M. A. Dugan, J. X. Tull, and W. S. Warren. "High-resolution acousto-optic shaping of unamplified and amplified femtosecond laser pulses". In: *Journal of the Optical Society of America B* 14.9 (1997), pp. 2348–2358. DOI: 10.1364/JOSAB.14.002348.

[121] M. Roth et al. "Acousto-optical shaping of ultraviolet femtosecond pulses". In: *Applied Physics B* 80.4 (2005), pp. 441–444. DOI: 10.1007/s00340-005-1767-8.

[122] F. Verluise et al. "Amplitude and phase control of ultrashort pulses by use of an acousto-optic programmable dispersive filter: pulse compression and shaping". In: *Optics Letters* 25.8 (2000), pp. 575–577. DOI: 10.1364/OL.25.000575.

[123] A. Monmayrant, S. Weber, and B. Chatel. "A newcomer's guide to ultrashort pulse shaping and characterization". In: *Journal of Physics B: Atomic, Molecular and Optical Physics* 43.10 (2010), p. 103001. DOI: 10.1088/0953-4075/43/10/103001.

[124] N. Krebs, R. A. Probst, and E. Riedle. "Sub-20 fs pulses shaped directly in the UV by an acousto-optic programmable dispersive filter". In: *Optics Express* 18.6 (2010), pp. 6164–6171. DOI: 10.1364/OE.18.006164.

[125] C. Schriever et al. "19 fs shaped ultraviolet pulses". In: *Optics Letters* 31.4 (2006), pp. 543–545. DOI: 10.1364/OL.31.000543.

[126] P. Zuo, T. Fuji, and T. Suzuki. "Spectral phase transfer to ultrashort UV pulses through four-wave mixing". In: *Optics Express* 18.15 (2010), pp. 16183–16192. DOI: 10.1364/OE.18.016183.

[127] T. Tanigawa et al. "Spatial light modulator of 648 pixels with liquid crystal transparent from ultraviolet to near-infrared and its chirp compensation application". In: *Optics Letters* 34.11 (2009), pp. 1696–1698. DOI: 10.1364/OL.34.001696.

[128] M. Born and E. Wolf. *Principles of optics. electromagnetic theory of propagation, interference and diffraction of light*. 7. (expanded) ed. Cambridge [u.a.]: Cambridge University Press, 1999.

[129] P. Laugier and G. Haïat. "Introduction to the Physics of Ultrasound". In: *Bone Quantitative Ultrasound*. Ed. by P. Laugier and G. Haïat. DOI: 10.1007/978-94-007-0017-8_2. Springer Netherlands, 2011, pp. 29–45.

[130] B. von Vacano, T. Buckup, and M. Motzkus. "In situ broadband pulse compression for multiphoton microscopy using a shaper-assisted collinear SPIDER". In: *Optics Letters* 31.8 (2006), p. 1154. DOI: 10.1364/OL.31.001154.

[131] R. Selle et al. "Generation of polarization-shaped ultraviolet femtosecond pulses". In: *Optics Letters* 33.8 (2008), pp. 803–805. DOI: 10.1364/OL.33.000803.

[132] P. Nuernberger et al. "Polarization-shaped femtosecond laser pulses in the ultraviolet". In: *Journal of Optics A: Pure and Applied Optics* 11.8 (2009), p. 085202. DOI: 10.1088/1464-4258/11/8/085202.

[133] I. Kostova et al. "Structure-Activity Relationships of Synthetic Coumarins as HIV-1 Inhibitors". In: *Bioinorganic Chemistry and Applications* (2006), p. 68274. DOI: 10.1155/BCA/2006/68274.

[134] C. M. Krauter et al. "Ultrafast branching in the excited state of coumarin and umbelliferone". In: *Physical Chemistry Chemical Physics* 15.41 (2013), pp. 17846–17861. DOI: 10.1039/C3CP52719K.

[135] M. Jiang et al. "Photocleavage of coumarin dimers studied by femtosecond UV transient absorption spectroscopy". In: *Physical Chemistry Chemical Physics* 19.6 (2017), pp. 4597–4606. DOI: 10.1039/C6CP08076F.

[136] C.-C. Shu and N. E. Henriksen. "Phase-only shaped laser pulses in optimal control theory: Application to indirect photofragmentation dynamics in the weak-field limit". In: *The Journal of Chemical Physics* 136.4 (2012), p. 044303. DOI: 10.1063/1.3678013.

[137] C. Canuel et al. "Excited states dynamics of DNA and RNA bases: Characterization of a stepwise deactivation pathway in the gas phase". In: *The Journal of Chemical Physics* 122.7 (2005), p. 074316. DOI: 10.1063/1.1850469.

[138] C. Z. Bisgaard et al. "Excited-State Dynamics of Isolated DNA Bases: A Case Study of Adenine". In: *ChemPhysChem* 10.1 (2009), pp. 101–110. DOI: 10.1002/cphc.200800516.

[139] J.-M. L. Pecourt, J. Peon, and B. Kohler. "Ultrafast Internal Conversion of Electronically Excited RNA and DNA Nucleosides in Water". In: *Journal of the American Chemical Society* 122.38 (2000), pp. 9348–9349. DOI: 10.1021/ja0021520.

[140] A. Reuther et al. "Femtosecond photo-ionization of nucleic acid bases: electronic lifetimes and electron yields". In: *Chemical Physics Letters* 325.4 (2000), pp. 360–368. DOI: https://doi.org/10.1016/S0009-2614(00)00699-0.

[141] T. Brixner et al. "Two-dimensional spectroscopy of electronic couplings in photosynthesis". In: *Nature* 434.7033 (2005), pp. 625–628. DOI: 10.1038/nature03429.

[142] T. Brixner et al. "Phase-stabilized two-dimensional electronic spectroscopy". In: *The Journal of Chemical Physics* 121.9 (2004), pp. 4221–4236. DOI: 10.1063/1.1776112.

[143] M. Cowan, J. Ogilvie, and R. Miller. "Two-dimensional spectroscopy using diffractive optics based phased-locked photon echoes". In: *Chemical Physics Letters* 386.1–3 (2004), pp. 184–189. DOI: https://doi.org/10.1016/j.cplett.2004.01.027.

[144] T. Zhang et al. "Optical two-dimensional Fourier transform spectroscopy with active interferometric stabilization". In: *Opt. Express* 13.19 (2005), pp. 7432–7441. DOI: 10.1364/OPEX.13.007432.

[145] D. Brida, C. Manzoni, and G. Cerullo. “Phase-locked pulses for two-dimensional spectroscopy by a birefringent delay line”. In: *Opt. Lett.* 37.15 (2012), pp. 3027–3029. DOI: 10.1364/OL.37.003027.

[146] N. Krebs et al. “Two-dimensional Fourier transform spectroscopy in the ultraviolet with sub-20 fs pump pulses and 250–720 nm supercontinuum probe”. In: *New Journal of Physics* 15.8 (2013), p. 085016. DOI: 10.1088/1367-2630/15/8/085016.

[147] S.-H. Lim, A. G. Caster, and S. R. Leone. “Single-pulse phase-control interferometric coherent anti-Stokes Raman scattering spectroscopy”. In: *Physical Review A* 72.4 (2005), p. 041803. DOI: 10.1103/PhysRevA.72.041803.

[148] B. von Vacano, T. Buckup, and M. Motzkus. “Highly sensitive single-beam heterodyne coherent anti-Stokes Raman scattering”. In: *Opt. Lett.* 31.16 (2006), pp. 2495–2497. DOI: 10.1364/OL.31.002495.

[149] B. von Vacano and M. Motzkus. “Time-resolving molecular vibration for microanalytics: single laser beam nonlinear Raman spectroscopy in simulation and experiment”. In: *Physical Chemistry Chemical Physics* 10.5 (2008), pp. 681–691. DOI: 10.1039/B715391K.

Danksagung

An erster Stelle möchte ich Prof. Dr. Marcus Motzkus danken. Sie ermöglichten mir meine Promotion in Ihrer Arbeitsgruppe. Durch das Arbeiten an zwei Projekten in verschiedenen Laboren konnte ich viele Dinge ausprobieren und die an einer Stelle erlangten Erkenntnisse oft an anderer Stelle wieder einbringen.
Prof. Dr. Wolfgang Petrich danke ich für die Übernahme der Zweitkorrektur meiner Arbeit.
Bei Prof. Dr. Rüdiger Klingeler und Prof. Dr. Björn-Malte Schäfer bedanke ich mich für die Bereitschaft, Teil meines Prüfungskomitees zu sein.
Bei der International Max Planck Research School for Quantum Dynamics in Physics, Chemistry and Biology (IMPRS-QD) möchte ich mich für die finanzielle Unterstützung meiner Promotion bedanken.
Ganz besonders bedanke ich mich bei Dr. Tiago Buckup für die fachlichen Diskussionen und offenen Gespräche. Du warst ein wichtiger Begleiter meiner Promotion. Mit deiner Erfahrung hast du mir sehr geholfen.
Die meiste Zeit meiner Promotion habe ich wohl mit meinen beiden Bürokollegen Dr. Lukas Brückner und Takeshi Miki verbracht. Danken möchte ich euch für mehr als drei Jahre in einer angenehmen Atmosphäre mit Diskussionen über ganz “einfache” Fragen, deren Antworten meist etwas schwieriger waren, und über “big problems”. Danke, Lukas, für die vielen Erklärungen bzgl. des Shapers. Danke, Takeshi, für deinen stets kritischen Blick auf meine NOPA-Justage.
Als nächstes möchte ich mich bei Dr. Jiang Man bedanken. Du hast die Grundlage für das UV-Labor gelegt. Danke, JJ, für unsere Zusammenarbeit dort. Du warst stets meine Expertin für Optik mit einer unglaublichen Leidenschaft.
Danke, Dr. Nick Paul, für den neuen Schwung während der zweiten Hälfte

meiner Promotion. Du brachtest viele neue Ideen und hattest stets Zeit für Diskussionen, die gerne über die Wissenschaft hinausgingen.
Ich möchte mich bei Dr. Julia Herz für die gemeinsame Zeit bedanken. Im Labor haben wir so manche Überraschung zusammen erlebt. Ansonsten hattest du immer ein aufbauendes Wort für mich.
Auch an apl. Prof. Dr. Hans-Robert Volpp im Erdgeschoss schicke ich ein Dankeschön. Die von dir gestellten Fragen haben mich stets weitergebracht und dein Optimismus ist ansteckend.
Allen anderen Gruppenmitgliedern während der vergangenen Jahre danke ich für die gemeinsame Zeit, die Fragen, die wir gemeinsam erörtert haben, und den frischen Wind, den Ihr in die Gruppe gebracht habt.
Ein herzlicher Dank geht an Sylvia Boganski und Angelika Neuner für alles neben der Wissenschaft, wie der Kontakt zur Univerwaltung und sonstiges Organisatorische. Dir, Angelika, danke ich besonders für die Gespräche, die eine schöne Abwechslung waren. Darüber hinaus danke ich unseren Elektronikern Uwe Branczyk und Gerhard Schodt so wie der Feinmechanikwerkstatt um Klaus Schmitt. Dank Ihrer Hilfe wurden Geräte, die scheinbar grundlos den Geist aufgaben, wiederbelebt und für jede Optik der passende Halter entworfen.
Ein weiteres Dankeschön schicke ich nach New York zu Prof. Dr. Thomas Weinacht, der mich mit seiner gesamten Expertise zum Thema AOM-Shaping unterstützte.
Außerdem möchte ich mich an dieser Stelle bei meinen Freundinnen und Freunden bedanken. Ihr wart immer für mich da. Während dem Studium haben einige von uns gemeinsam die meisten Übungszettel gemeistert, viel gelernt und zusammen so manches erlebt. Ganz besonders möchte ich Dr. Simona Scheidt danken für die freundschaftliche Unterstützung und die Mittagessen mit den so wohltuenden Gesprächen.
Mein größter Dank gilt meiner Familie und meinem Freund, Dr. Jakob Kunz! Danke für den Rückhalt, die Unterstützung und das Vertrauen in mich. Ihr gebt mir so viel Kraft und zeigt mir, was wirklich im Leben zählt. Ganz besonders danke ich dir, Jakob, dass du während der letzten Jahre mich und mit mir meine Promotion ausgehalten hast. Unsere gemeinsame Zeit und der Austausch mit dir über den (Uni-) Alltag waren und sind mir weiterhin sehr wichtig. Du hattest endlose Geduld und Verständnis.